

Plasmonic Hot Electron Photovoltaics by Internal Photoemission

by
Finlay MacNab

MSc., McGill University, 2007

BSc., McGill University, 1996

Thesis Submitted in Partial Fulfillment of the
Requirements for the Degree of
Doctor of Philosophy

in the
Department of Chemistry
Faculty of Science

© Finlay MacNab 2021
SIMON FRASER UNIVERSITY
Fall 2021

Copyright in this work is held by the author. Please ensure that any reproduction or re-use is done in accordance with the relevant national copyright legislation.

Declaration of Committee

Name: Finlay MacNab

Degree: Doctor of Philosophy

Title: Plasmonic Hot Electron Photovoltaics by Internal Photoemission

Committee:

Chair: Corina Andreoiu
Professor, Chemistry

Gary W Leach
Supervisor
Associate Professor, Chemistry

Vance Williams
Committee Member
Professor, Chemistry

Loren Kaake
Committee Member
Associate Professor, Chemistry

Simon Watkins
Examiner
Professor, Physics

Karthik Shankar
External Examiner
Professor, Electrical & Computer Engineering
University of Alberta

Abstract

The challenge of plasmonic hot electron science is in understanding and integrating the three pillars of device efficiency: (i) plasmonic excitation, (ii) plasmon decay and hot carrier transport, and (iii) rectification of the carrier's energy across an interface. These three concepts were introduced and synthesized into a systematic experimental approach to the design and fabrication of silver-zinc oxide Schottky junction, plasmonic photovoltaic devices. Devices were built and tested to establish structure-function relationships that underpinned device performance. The high-throughput device optimization strategies employed allowed the fabrication of hundreds of test samples, iteratively achieving: (i) a novel deposition technique for the PVD evaporation of ultra-smooth, single-crystal silver thin films; (ii) a low-cost, single step, high fidelity nanopatterning technique; (iii) prism-coupled plasmonic photovoltaic devices that exhibited world best performance by the internal photoemission mechanism (11.2% IQE @ 543 nm); and (iv) a low-cost, free-space coupled, nanostructured design, that exhibited strong second order nonlinear second harmonic generation and two photon photoluminescence, as well as, optical absorbance that agreed well with models, informing the interpretation of the nanostructure's photovoltaic response.

Keywords: plasmonics; second harmonic generation; Schottky junctions; internal photoemission, photovoltaics, epitaxial single-crystal silver

Dedication

I dedicate this work to my parents, my mother-in-law, my partner Clare and my two children, Julia and Fiona, for their love, compassion, encouragement, and sense of humour.

Acknowledgements

Parts of the data that is presented in this thesis was collected as part of a commercial research project over the course of 3.5 years. I acknowledge the efforts of my colleagues and co-workers. Particularly, I acknowledge: Dr. Xin Zhang and Dr. Enrico Bovero, for their contributions to material characterization. Dr. Tom Johansson and Dr. Haijun Qiao, for their contributions to optical characterization, Dr. Claire McCague, Dr. Kourosh Khosraviani, Dr. Jayna Chan, Steven Gou, and Greg Wong, for their work on the fabrication team, Dr. Murat Cetinbas for his work on FDTD simulations, and Dr. Andras Pattantyus-Abraham in his capacity as project manager and friend.

At SFU, I would like to acknowledge the invaluable contributions to this work from my Senior Supervisor, Prof. Gary Leach, as well as his mentorship and guidance over the years. Further, I acknowledge Dr. Saeid Kamal for his help with optical characterization and Kyle Vine for his assistance with FDTD studies. I would also like to acknowledge my groupmates, and my friends Dr. Ben Britton, Dr. Heather Baroody Adams, and Dr. Reagan Belan, for all of their help. Finally, I would like to acknowledge Prof. Elicia Maine for her mentorship and instruction in the art and practice of translational scholarship.

Table of Contents

Declaration of Committee	ii
Abstract	iii
Dedication	iv
Acknowledgements	v
Table of Contents	vi
List of Figures	viii
List of Acronyms	xiv
Chapter 1. Introduction	1
1.1. Plasmonics and Surface Plasmons	1
1.1.1. Surface Plasmon Polaritons	2
Prism coupling of SPPs	6
1.1.2. Locally Resonant Surface Plasmons	10
1.2. Surface Plasmon Decay	15
1.3. Schottky Junctions	20
1.4. Internal Photoemission	25
References	31
Chapter 2. Experimental Methods	34
2.1. Physical Vapour Deposition	34
2.1.1. Thermal Evaporation of Silver	35
2.1.2. Magnetron Sputtering of Zinc Oxide	40
2.1.3. Magnetron Sputtering of Doped Zinc Oxide	44
2.2. Nanostructuring techniques	45
2.3. Material Characterization Techniques	48
2.3.1. Scanning Electron Microscopy	48
2.3.2. Focused Ion Beam Milling and Transmission Electron Microscopy	51
2.3.3. Two-Dimensional X-Ray Diffraction	53
2.4. Electrical Characterization Techniques	56
2.4.1. Diode characterization	57
2.5. Optical and Optoelectronic Characterization Techniques	58
2.5.1. Otto Coupled Devices	59
2.5.2. Free-Space Coupled Nanostructured Devices	67
2.6. Confocal Microscopy and Plasmonically Enhanced Nonlinear Optical Techniques	68
References	74
Chapter 3. High Efficiency Plasmonic Hot Electron Rectification at Planar Ag/ZnO Schottky Junctions	77
3.1. Introduction	77
3.2. Results and Discussion	79
3.3. Summary	91
References	93

Chapter 4. Epitaxial Silver Plasmonic Arrays on Silicon by Nanostencil Lithography.....	95
4.1. Introduction.....	95
4.2. Results and Discussion	97
4.3. Summary	106
4.4. Supplemental Figures.....	107
References.....	111
Chapter 5. Nanostructured Silver/Zinc Oxide Schottky Junctions for Plasmonic Photovoltaics	115
5.1. Introduction.....	115
5.2. Results and Discussion	116
5.3. Summary	133
References.....	135
Chapter 6. Conclusions and Future Work	138
Appendix A.	142
Supplementary Data File	142
Appendix B.	143
Supplementary Data File	143
Diode Parameter Fitting	143
Details of Prism Device Diode Testing	144
Details of Nanostructured Device Diode Testing	147
FDTD Simulation Details	149

List of Figures

Figure 1.1.	The permittivity of silver (reprinted with permission from reference 1). The measured values agree with the Lorentz Drude model.....	5
Figure 1.2.	Surface Plasmon Polariton Dispersion Curve. For light in a vacuum $\omega=ck_x$. The dispersion curve relates oscillation frequency, ω , to the x component of the wave vector, k_x . The dispersion curve describes how momentum changes with frequency. The relative permativity of the dielectric, ϵ_d , is equal to 1 (vacuum) in the above plot.....	6
Figure 1.3.	Left: Otto configuration and Right: Kretschmann configuration (reprinted with permission from reference 1)	7
Figure 1.4.	Dispersion curve depicting energy and momentum matching conditions for prism coupling of SPPs. (reprinted with permission from reference 1) .	8
Figure 1.5.	Otto coupling to photovoltaic prism devices. a) a device cartoon, b) simulated SPP coupling maxima for different ZnO film thickenss c) peak shape at 633 nm for different ZnO thicknesses	9
Figure 1.6.	SPP electric field decay lengths propagating in the x direction.	10
Figure 1.7.	The harmonic oscillation of a plasmonic nanoparticle under the influence of an external field.....	11
Figure 1.8.	Green absorption and green scattering from the plasmonic gold nanoparticle decoration of the Lycurgus cup (reprinted with permission from reference 1).....	13
Figure 1.9.	a,b,c) A single LSP excited nanoparticle. b) the splitting of excitation energies when a strongly coupled dimer is excited across the long axis of the dimer. c) along the the long axis d) A simulated triangular arrangement of LSP active centers from different directions(arrows). e) Simulated scattering from the structure in (d). (reprinted with permission from reference 1).....	15
Figure 1.10.	a) Cartoon of grating-coupled SPP decay generating hot carriers. Intra-band transitions can be surface- and phonon-assisted. Interband direct transisitons are the most probable when photon energies are above the transition threshold, 3.4eV for silver. (adapted with permission from reference 13).....	16
Figure 1.11.	a) Simplified band diagram of silver, p is the equilibrium electron distribution. b) High energy hot electrons resulting from intra sp-band transitions. c) Low energy electrons and high energy holes resulting from interband transition from the d- to sp-band. (from ref 14).....	17
Figure 1.12.	The kinetic energy of 2PPE generated electrons with increasing silver nanoparticle size under 3.16ev illumination (reprinted with permission from reference 15).....	19
Figure 1.13.	Band bending of an n-type semiconductor metal junction. E_v is the energy of HOMO, E_c is the energy of the LUMO (adapted from ref 14).....	21
Figure 1.14.	Schottky barrier under forward (left) and reverse (right) bias (V)	22
Figure 1.15.	The crystal structure of wurtzite ZnO (adapted from ref 23).....	23

Figure 1.16.	Schottky contact a) under ideal conditions, and b) pinned by interface dipoles (reproduced from ref 26).	24
Figure 1.17.	(left) Band diagram of a theoretical nanoparticle undergoing intraband plasmonic excitation of hot electrons, showing the distribution of energies as a function of EDJDOS (right) The interaction of hot electrons with the barrier. Electrons with energy $< \Phi_B$ are reflected. (adapted with permission from reference 27).....	26
Figure 1.18	The escape cap model momentum diagram. (reprinted with permission from reference 32).....	28
Figure 2.1.	The PVD 75 modular deposition instrument.	35
Figure 2.2.	Equilibrium vapour pressure for a selection of metals (reprinted with permission from reference 1).....	36
Figure 2.3.	Angle dependent thickness of Thermal evaporation. (adapted with permission from reference 7).....	38
Figure 2.4.	a) Schematic of a simplified DC sputtering system (adapted with permission from reference 7) b) The ionization cascade for argon gas...	40
Figure 2.5.	Cross section of a circular sputtering target in a magnetron configuration. (reprinted with permission from reference x)	42
Figure 2.6.	Nanostencil images. a) cross-section of the membrane and scaffold. b) Transparent, iridescence of the thin stress-free SiN. c) Trench geometry. d) SEM image of the nano-hole array.....	46
Figure 2.7.	Basic elements of a scanning electron microscope.	49
Figure 2.8.	Examples of SEM images. a)Top surface of samples presented in Chapter 5, b) cross section of the ZnO, dZnO interface, c) discontinuous growth of silver on a mica substrate, d) cross section of experimental three layer deposition of dZnO/ZnO/ZnO on Si(100).	51
Figure 2.9.	Simplified schematic of a transmission electron microscopy instrument.	52
Figure 2.10.	High resolution TEM cross section of the Ag-Si interface (inset the focused ion beam prepared sample being lifted out).	53
Figure 2.11.	Graphical representation of diffraction according to Bragg's law.	54
Figure 2.12.	2D X-Ray diffraction spectra. a) Polycrystalline silver with ring angle X and 2θ angular distance from the point of origin. b) Single-crystal silver results in point diffraction spots. The dashed red line is the orientation normal to the surface.	55
Figure 2.13.	The M150 probe station. Samples were placed under the microscope on the circular vacuum sample stage and probed with tungsten needles attached to manually operated probe manipulators. Experiments were conducted under the control of the Agilent 1500A analyzer.	56
Figure 2.14.	Left: Diode curve (blue) of sample P018r13 and ohmic junction of a failed device. Right: Image of the silver top contacts of prism sample P018r18 and probe tip.	57
Figure 2.15.	Fill Factor of prism sample P011r21. The red area fraction of the blue area is the fill factor.	59
Figure 2.16.	Cartoon of the Otto configured prism devices. 2%AlZnO doped zinc oxide is the transparent contact.	59

Figure 2.17.	Otto configuration $\text{TiO}_2/\text{ZnO}/\text{Ag}$ The coupling (reflectivity, R) as a function of ZnO and Ag thickness, d, at 633 nm. The colour scale represents reflectivity (Coupling is insensitive to Ag thickness beyond ~ 80 nm) 60
Figure 2.18.	Otto configuration $\text{TiO}_2/\text{ZnO}/\text{Ag}$ Effect of ZnO stack thickness for 633 nm light. 61
Figure 2.19.	Calculated wavelength and ZnO stack thickness dependence for optimal coupling for devices with 150 nm thick Ag top contacts. 62
Figure 2.20.	FDTD simulation of field enhancement at the Ag/ZnO interface. The field at the surface is enhanced 77 times over the field of the incident photon and decays exponentially into the dielectric and metal layers (see Section 1.11). 63
Figure 2.21.	Otto configuration TiO_2/ZnO (200 nm)/Ag with surface roughness: the simulated reflectance vs angle for flat (top left) Ag, and rough ZnO-Ag interfaces with RMS roughness = 1 nm (top right), 3 nm (bottom left), and 5 nm (bottom right), 64
Figure 2.22	Reflectivity versus coupling angle for prism sample P015r7 with $\sim 99\%$ coupling efficiency at 633 nm 65
Figure 2.23	Coupling efficiency of prism samples over time showing reproducibility increasing over time. 65
Figure 2.24.	Photovoltaic response (upper) and open circuit voltage (lower) over time for the prism device sample set. 66
Figure 2.25.	The excitation mechanism of two photon photoluminescence (2PPL), Left) the instantaneous two photon excitation common for organic dyes. Right) two sequential excitations. Δt indicates a nanoparticle shape dependent relaxation time on the order of picoseconds. 70
Figure 2.26.	top) The SHG process mediated by a virtual transition state. bottom) The anharmonic potential environment that supports second order non linear optical processes in a non-centrosymmetric environment. 72
Figure 3.1.	Three step internal photoemission mechanism across a Schottky junction: i) coupling of free space electromagnetic waves (green wavy arrow) to surface plasmons, ii) the decay of the excited surface plasmons into hot electrons with energy $h\nu$ (red verticle arrow), and iii) the inelastic internal photoemission of a generated hot electron over the Schottky barrier (red horizontal arrow). 78
Figure 3.2.	a) Otto configuration prism-coupled device enabling evanescent wave coupling of light to SPPs supported at the Ag/ZnO interface. b) Device layer schematic depicting SPP excitation, and hot electron internal photomission across the Ag ZnO Schottky interface 80
Figure 3.3.	Heatmap of QE vs Coupling Angle for 539 Otto-coupled prism device samples at 633 nm excitation wavelength. 81
Figure 3.4.	Morphology of the Ag film surface. left) SEM image of the large-grained smooth silver film on a prism sample. (inset) polycrystalline silver deposited under the same conditions on glass. right) smooth oriented ZnO prior to Ag overcoating. (inset) Atomic force microscope scan $1 \mu\text{m} \times 1 \mu\text{m}$ area RMS roughness = 1.3 nm, Ra = 1.0 nm. And 2D-XRD of the prism sample showing the alignment of the Ag $\langle 111 \rangle$ and ZnO $\langle 002 \rangle$ diffraction spots 82

Figure 3.5.	IV curve of a Ag/ZnO diode from representative prism devices The blue curve is an example of a prism sample with a Schottky junction interface (Section 1.5). The green curve was from an ohmic junction (rejected sample). See Appendix B for.....	83
Figure 3.6.	A representative sample of prism devices reveals the correlation between QE and ideality factor.....	84
Figure 3.7.	a) 2D XRD of prism sample. b) The integrated intensity along the arc <i>X corresponding to the radial 2θ spacing (see Section 2.3.3)</i> . The aligned narrow spots indicate that the TiO ₂ /dZnO/ZnO/Ag films are aligned.	85
Figure 3.8.	The overall crystallinity score vs quantum efficiency for a selection of prism devices measured at 633 nm.....	86
Figure 3.9.	Series resistance vs quantum efficiency for a representative sample of prism device measurements.....	87
Figure 3.10.	Trends in barrier height vs quantum efficiency.	88
Figure 3.11.	V _{oc} dependence on barrier height.....	89
Figure 3.12.	Fill factor versus open circuit voltage.	90
Figure 3.13.	Fowler plot of device response vs incident photon energy.....	91
Figure 4.1	SEM investigation of the evolution of silver growth from isolated epitaxial islands to continuous films by high temp. thermal evaporation. a) - d) show H-Si terminated Si(100) surface mediated Ag film growth at thicknesses of a) 20 nm, b) 30 nm (cross section, tilt view), c) 75 nm, and d) 300 nm (inset: cross section, tilt view). Panels e) and f) are images of H-Si terminated Si(111) surface mediated Ag film growth at e) 30 nm and f) 500 nm.....	100
Figure 4.2.	2D XRD patterns of Ag films grown on Si substrates. The dashed red lines show the sample surface normal and the blue lines show directions of constant χ angle corresponding to a given lattice plane orientation (see section 2.4). All films tested were 300 nm thick a) Low temp. Ag (see 2.1.1) on native oxide coated Si (100) b) Low temp. Ag on H-Si terminated Si(100) c) High temp Ag. on a H-Si terminated Si(111) d) High temp Ag. on a H-Si terminated Si(100).....	101
Figure 4.3.	Low temperature nanostenciled pillars a) 100 nm on polycrystalline Ag. b) 20 nm of Ag on a native oxide terminated Si(100) c) 100 nm of Ag on a 300 nm high temperature deposited Ag(100)//Si(100) planar film (cross section, tilt view), d) top view image of c) showing faceted nanopillars, e) schematic of epitaxial faceted crystalline silver nanopillar arrays.	103
Figure 4.4.	High resolution transmission electron microscopy of nanostenciled Ag pillars. a) Cross section of a nanopillar with the Ag(100)/pillar interface indicated by the green double headed arrow. b) Expanded view of the Ag(100)/pillar interface near the nanopillar edge. c) High resolution image of the interface region indicated by the green box in b). The green arrows indicate the location of the interface and demonstrate epitaxial deposition of the Ag nanopillar with a low defect density interface. d) indexed fast Fourier transform of the image in c).....	104
Figure 4.5.	Confocal microscope image of plasmonically-enhanced second harmonic generation from ZnO-coated epitaxial silver nanopillar arrays. a) SHG image from ZnO-coated silver in patterned (bright) and unpatterned (dark)	

	silver regions. b) Magnified image highlighting the hexagonal, pillar-resolved SHG response at the edge of the patterned nanopillar array. The inset shows the cross-sectional SHG intensity along a row of pillars indicated by the blue hatched line.	106
Figure 4.6	SEM images of thermally evaporated Ag film morphologies. All films were deposited at a rate of 3 \AA s^{-1} on Si(100) substrates: a) 150 nm Ag film deposited at $55 \text{ }^\circ\text{C}$ on the native oxide surface, b) 150 nm Ag film deposited at $250 \text{ }^\circ\text{C}$ on the native oxide surface, c) 300 nm Ag film deposited at $55 \text{ }^\circ\text{C}$ on a BOE etched surface, and d) tilt view of 300 nm Ag film deposited at $350 \text{ }^\circ\text{C}$ on a BOE etched surface.	108
Figure 4.7	SEM cross section images of thermally evaporated Ag film morphologies on H-Si(100) deposited at $350 \text{ }^\circ\text{C}$ and a rate of 3 \AA s^{-1} . a) 50 nm Ag islands illustrating that the Ag island crystallite facets are aligned along the crystal planes of the underlying silicon. b) 50 nm Ag islands showing Ag island facet angle of 54.8° , consistent with the expected angle between (100) and (111) planes of the Ag fcc lattice.	108
Figure 4.8.	SEM cross section images of thermally evaporated Ag film morphologies on Ag(100)//H-Si(100) deposited at $55 \text{ }^\circ\text{C}$ and a rate of 3 \AA s^{-1} through a nanostencil mask. a) Large scale image illustrating the uniformity of the crystal nanopillar features and b) Ag island facet angle of 45° , consistent with the expected angle between (100) and (110) planes of the Ag fcc lattice.	109
Figure 4.9.	SEM top view images of a nanostencil mask illustrating a) the $3 \text{ mm} \times 3 \text{ mm}$ patterned area consisting of a nanopatterned Si_3N_4 membrane supported by a silicon scaffold fabricated on a 0.6 mm thick silicon chip. The patterned region consists of $150 \text{ }\mu\text{m} \times 3000 \text{ }\mu\text{m}$ windows containing b) hexagonal arrays of 450 nm diameter pores with 900 nm periodicity. c) A typical Ag nanopillar array fabricated by nanostencil lithography of Ag deposited at 55°C on Ag(100)//H-Si(100).	109
Figure 4.10.	SEM top view images of a) a contaminated nanostencil mask, b) the misshapen nanopillars resulting from deposition through the contaminated mask, and c) an expanded view of pillars deposited through the contaminated mask illustrating that pillar faceting remains prevalent even under these deposition conditions.	110
Figure 4.11.	SEM images of a ZnO coated Ag(100) substrate. a) SEM image (cross section, tilt view) of 140 nm thick sputter-deposited ZnO layer atop a planar Ag(100) region of the substrate. The SEM image shows a fragmented piece of the ZnO layer in the left foreground resulting from fracture of the substrate. b) SEM image (cross section, tilt view) of 140 nm thick sputter-deposited ZnO layer atop the epitaxial silver patterned nanopillar region, illustrating the conformal coating of the Ag nanopillars. The region labeled by 141.3 nm thickness lies between Ag nanopillars and corresponds to the ZnO overlayer thickness.	110
Figure 5.1.	Figure 5.2. Device cartoon. The device comprises: a single-crystal Si<100> substrate coated with single-crystal Ag<100> nanostructured plasmonic coupling layer, a ZnO semiconducting layer forms a rectifying junction at the Ag interface, and a highly doped Al:ZnO transparent 250	

	μm circular top contact is probed with a tungsten needle. (see Chapter 2)	116
Figure 5.3.	Reprinted Figure 4.3 for clarity. Low temperature nanostenciled pillars a) 100 nm on polycrystalline Ag. b) 20 nm of Ag on a native oxide terminated Si(100) c) 100 nm of Ag on a 300 nm high temperature-deposited Ag(100)/Si(100) planar film (cross section, tilt view), d) top view image of c) showing faceted nanopillars, e) schematic of epitaxial faceted crystalline silver nanopillar arrays.	118
Figure 5.4.	High-asymmetry planar Ag bottom contact PVD-sputtered ZnO diode curve (see Section 2.4.1).	119
Figure 5.5.	a) Cross section SEM images of the nanostructured Ag/ZnO interface. b) 2D XRD of the highly crystalline and oriented Ag and ZnO films (see section 2.3.3).	121
Figure 5.6.	FDTD Simulated absorption vs broadband experimentally measured spectrum of the test chip design.	122
Figure 5.7.	Measured absorption of a plasmonic photovoltaic test chip under s-polarized illumination. (see Section 2.5.2)	123
Figure 5.8.	a) SEM image of a nanostructured device showing the zinc oxide with tilted c-axis orientation (arrows). Confocal microscope image of plasmonically-enhanced second harmonic generation from ZnO-coated epitaxial silver nanopillar arrays shown in a). The image highlights the hexagonal, pillar-resolved SHG response at the edge of the patterned nanopillar array. The inset shows the cross-sectional SHG intensity along a row of pillars indicated by the blue hatched line.	125
Figure 5.9.	Intense 2D-SHG diffraction from a nanostructured sample under illumination with 800 nm light at 42° angle of incidence (viewed through a paper screen).	126
Figure 5.10.	Time-resolved microscopy of 2PPL from Ag/ZnO nanostructured devices. left) Long-lived fluorescence from a nanostructured Si/Ag/ZnO/dZnO device (see section 2.5.3). right) A histogram of the measured lifetimes and lifetime fit parameters.	128
Figure 5.11.	Wavelength dependent photovoltaic response. (circular callout: IQE at 930 nm is unexpectedly low in a region of high absorption).	130
Figure 5.12.	Surface lattice resonance with electric field intensity distribution between the pillars rather than near the ZnO-Ag Schottky interface can lower expected IQE.	132
Figure 6.1.	Gold plasmonically electrodeposited from a gold chloride solution on a polycrystalline gold film excited with 650 nm incident light in a Kretschmann coupled geometry. Inset) A region of the same film that was not illuminated, at identical magnification.	141

List of Acronyms

<i>2PPE</i>	Two photon photoemission
2PPL	Two photon photoluminescence
ACE	Acetone
ALD	Atomic layer deposition
BOE	Buffered oxide etch
BSE	Back scattered electron
<i>c</i>	Speed of light
CDA	Coupled dipole approximation
<i>DC</i>	Direct current
<i>DI</i>	Deionized
DOS	Density of states
dZnO	Doped zinc oxide
<i>e</i>	Fundamental charge of an electron
<i>e''</i>	Imaginary permittivity
ED	Electrodeposition
<i>EDJDOS</i>	Electron distribution joint density of states
<i>E_F</i>	Fermi energy
<i>E_{loc}</i>	Local electric field vector
EM	Electromagnetic
EQE	External quantum efficiency
eV	Electron volts
FCC	Face centred cubic
FDTD	Finite difference time domain
FF	Fill factor
FIB	Focused ion beam
FWHM	Full width half maximum
GASD	Gas assisted selective deposition
<i>h</i>	Planck's Constant
H	Magnetic field

I_0	Saturation current
I_{mp}	Current at maximum power
<i>IPA</i>	Isopropyl alcohol
IPE	Internal photoemission
IQE	Internal quantum efficiency
I_{sc}	Short circuit current
k	Wavevector
k	Boltzmann constant
LRSP	Lattice resonant surface plasmons
LSP	Localized surface plasmon
LSPR	Localised surface plasmon resonance
m^*	Effective mass
MBE	Molecular beam epitaxy
MIM	Metal-insulator-metal
n	Index of refraction
n	Ideality factor
NLO	Nonlinear optics
OCS	Overall crystallinity score
P	Polarization vector
P_{abs}	Absorbed power
PCE	Power conversion efficiency
PE	Primary electron
<i>PMMA</i>	Polymethylmethacrylate
PV	Photovoltaic
PVD	Physical vapour deposition
QCM	Quartz crystal thickness monitor
QE	Quantum efficiency
REAM	Rapid electron area masking
RF	Radio Frequency
R_s	Series resistance
R_{shunt}	Shunt resistance

<i>SE</i>	Secondary electron
SEM	Scanning electron microscopy
SERS	Surface enhanced Raman scattering
SFU	Simon Fraser University
SHG	Second harmonic generation
SiN	Silicon nitride
S-K	Stranski-Krastanov (growth mode)
SP	Surface plasmon
SPP	Surface plasmon polariton
SPR	Surface plasmon resonance
TCO	Transparent conducting oxide
TCSPC	Time correlated single photon counting
<i>TE</i>	Thermal evaporation
TEM	Transmission electron microscopy
TiO ₂	Titanium dioxide
TIR	Total internal reflection
UV	Ultraviolet
v_g	Group velocity
VLSI	Very large scale integration
V_{mp}	Voltage at maximum power
V_{oc}	Open circuit voltage
XRD	X-ray diffraction
ZnO	Zinc oxide
α	Polarizability
ϵ	Relative permittivity
ϵ'	Real permittivity
ϵ_0	Permittivity of vacuum
η_e	External quantum efficiency
η_i	Internal quantum efficiency
λ	Wavelength
ν	Photon frequency

σ	Cross-section
ϕ_B	Schottky barrier
Φ_M	Metal work function
$\chi^{(1)}$	Linear susceptibility
$\chi^{(2)}$	Second order susceptibility
X_{sc}	Semiconductor electron affinity
ω	Angular frequency

Chapter 1.

Introduction

The work described in this thesis includes data gathered through the intense efforts of a large team of dedicated researchers over several years. The details of the author's specific contributions can be found as a footnote at the beginning of Chapters 3, 4, and 5. Briefly, the author was intimately involved in fabrication and design of devices, and some aspects of device characterization, referred to as major contributions in the footnotes. In addition, the author was called upon, when required, to fulfil other characterization duties usually carried out by other team members, referred to as minor contributions. In the course of research activities, the author iteratively communicated with the optics and modelling team members to inform their activities, referred to as minimal in the footnotes.

The study of plasmonic hot electron photovoltaics is a complex inter-disciplinary research activity that draws heavily on insights from materials chemistry, optoelectronics, and microelectronic fabrication. In order to ground the reader's understanding across the broad landscape of the research to be presented, this introductory Chapter will present background information intended to promote inter-disciplinary bridges of understanding and insight.

1.1. Plasmonics and Surface Plasmons

Plasmonics is the study of the confinement of electromagnetic (EM) fields to nanometer-scale dimensions on the order of, or well below, the wavelength of light that oscillates at a similar frequency. This confinement is achieved through the interaction of EM fields, most often in the form of an incident photon, with quasi-free electrons at a designed interface.¹ These fascinating and complex interactions are called surface plasmons or surface plasmon polaritons. They have been observed across many types of material combinations but are most easily studied and understood at metal/dielectric interfaces that are excited with light at optical frequencies.²

Unlike the familiar case of simple reflection from a metal surface, where free electrons at the metal dielectric interface oscillate under the influence of an incoming

photon's EM field so that their polarization cancels the external field and generates a reflected photon 180° out of phase, surface plasmons are the result of coupling between quantized electron oscillations called surface plasmons and incident photons. An understanding of plasmonics hinges on descriptions of the complex electron dynamics that develop within metals. Plasmons arise from the interaction of negatively charged free electrons and positively charged lattice bound nuclei. As described in the rest of Section 1, plasmons, or bulk plasmons, are quantum quasiparticles that are most easily understood in chemical terms as analogous to extended phonon vibrations within crystal lattices, but instead of collective lattice motions bulk plasmons are collective free electron oscillations. The periodic distribution of positively charged metal atom nuclei within the metal lattice give rise to resonant bulk plasmon frequencies where free electrons within the metal oscillate collectively within the lattice. Bulk plasmons oscillate with a frequency equal to the plasma frequency, ω_p , discussed in the next section.

Surface plasmons, distinct from bulk plasmons, can only be excited in the near surface region of a metal dielectric interface where the translational symmetry of the metal lattice is broken. Surface plasmon excitations are characterized by an oscillating electromagnetic field that is confined to a metal dielectric interface and have a characteristic frequency related to the bulk plasma frequency of the metal and the dielectric properties of the overlayer. Surface geometry and nanoparticle size effects can also influence the characteristic surface plasmon frequency ω_{SP} .

The excitation of surface plasmons is a complex topic, but in general they are excited optically in one of three ways: grating coupling, prism coupling, and nanostructure mediated coupling. Grating coupling and prism coupling give rise to surface plasmon polaritons (SPPs) which propagate along planar metal-dielectric interfaces and localized surface plasmons (LSPs) can be excited at structured metal surfaces like periodic arrays of nanostructures or on individual nanoparticles and do not propagate along a surface. The prism-coupled and nanostructure-mediated coupling techniques are relevant to this work and are discussed in the next two sections

1.1.1. Surface Plasmon Polaritons

The central importance of SPPs to spectroscopic and optoelectronic research arises from the fact that plasmonic electric fields are confined to a metal/dielectric

interface and that the fields of coupled photons are concentrated from a 3-Dimensional (3D) delocalized volume down to a 2-dimensional (2D) area. This field confinement leads to a field enhancement that is typically an order of magnitude in close proximity to the metal surface and is used to advantage to enhance otherwise weak spectroscopic signals in some optical experiments, such as surface enhanced Raman scattering (SERS). The sensitivity of SPP coupling conditions to the index of refraction of the dielectric overlayer is also exploited in techniques such as surface plasmon resonance, (SPR), spectroscopy³, and forms the basis of many color-based biosensor applications, different lab-on-a-chip sensors, and to sense metal adsorbates in flow cells⁴.

Surface plasmon polaritons are composite surface bound electromagnetic excitations that are comprised of a surface plasmon and a photon, forming a polariton. Polaritons are quantum quasiparticles that result from strong coupling of light and matter and can only be excited under carefully designed conditions⁵. In the case of SPPs, the conditions under which light can be coupled to surface plasmons to generate an SPP propagating parallel to the metal surface depends on the matching of the momentum vectors of the incident photon in the x direction, k_x , and the momentum of the surface plasmon polariton, k_{SPP} , as well as the frequency of incident light and that of the surface plasmon frequency ω_{SP} (Figure 1.1)

The strong coupling of a surface plasmon and a photon gives rise to a SPP with a frequency vs momentum (dispersion) curve depicted in red. Briefly, and according to the Lorentz Drude model, in which the metal is approximated as a neutral plasma of free-electrons within an immobile lattice of positive nuclei, the momentum vector of the SPP parallel to the metal surface (the x-direction) is given by Equation 1.1.

$$k_{SPPx} = \frac{\omega}{c} \left(\frac{\epsilon_m \epsilon_d}{\epsilon_m + \epsilon_d} \right)^{1/2} \quad (1.1)$$

where ϵ_m is the complex permittivity of the metal layer, ϵ_d is the permittivity of the dielectric layer, ω is the angular frequency of the plasmon oscillation, and c is the speed of light.

In order for the SPP to be confined to the surface it must have no real momentum in the z-direction, normal to the surface. This value, denoted k_{SPPz} is given for an infinite metal-dielectric interface by Equation 1.2.

$$k_{SPPz} = \frac{\omega}{c} \left(\frac{\epsilon_d^2}{\epsilon_m + \epsilon_d} \right)^{1/2} \quad (1.2)$$

SPPs will be confined to the metal surface if the value of k_{SPPz} is imaginary. At first glance, the value of k_{SPPz} appears to be a real number. To understand why it is not, and the significance of an imaginary value of the SPP's k_z momentum, the concept of complex permittivity and negative permittivity must be introduced.

A material's permittivity, a measure of that material's ability to resist electric flux generated by an electric field, is a frequency-dependent property. The mathematics of the Drude model¹ allow the derivation of a material property called the plasma frequency:

$$\omega_p = \frac{ne^2}{\epsilon_0 m^*} \quad (1.3)$$

where n is the number density of electrons, e is the charge of an electron, ϵ_0 is the permittivity of vacuum, and m^* is the effective mass of the electron within the metal lattice. The motion of electrons within a material is governed by the distribution of charges that give rise to the lattice and band structure. The collective effect of this local environment on the motion of electrons results in electron motion that can be modeled in Equation 1.3 as a change in the mass of an electron travelling within the bulk of the metal. The effective mass is a key property that determines the plasma frequency inside a plasmonic metal.

In the absence of damping effects, the frequency-dependent value of a metal's permittivity can be approximated by:

$$\epsilon(\omega) = 1 - \frac{\omega_p^2}{\omega^2} \quad (1.4)$$

From Equation 1.4 it is evident that, when the frequency of the EM field interacting with the metal is less than the plasma frequency, the real permittivity has a negative value.

Another way of expressing the frequency-dependent permittivity of metals that incorporates damping effects involves a real and imaginary component of this dependence. In the optical regime, the permittivity of plasmonically active metals is

dominated by the frequency-dependent motion of conduction band electrons within the metal, and is given by the dielectric function:

$$\epsilon(\omega) = \epsilon'(\omega) + i\epsilon''(\omega) \quad (1.5)$$

where ϵ' is the material's real permittivity and ϵ'' is the imaginary permittivity. ϵ' is a measure of the dispersion of light within the material. ϵ'' is a measure of the damping of oscillating electric fields within the medium and is related to a material's extinction coefficient. The real and imaginary values of permittivity for silver are well known and are plotted in Figure 1.1.

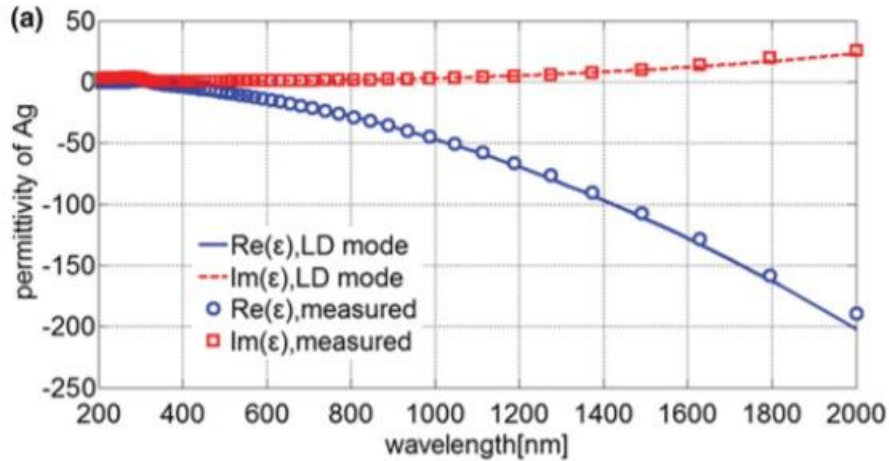


Figure 1.1. The permittivity of silver (reprinted with permission from reference 1). The measured values agree with the Lorentz Drude model.

From the plot above and recognizing from Equations 1.1 and 1.2 that k_{sppx} is real and k_{sppz} is imaginary as long as the value of $\epsilon_m + \epsilon_d$ is negative, surface plasmons can be excited at a silver dielectric interface across the window of optical energies and into the IR spectrum.

Further examination of Equation 1.1 yields a dispersion plot of the real momentum vector of the SPP along the surface x-direction with frequency (Figure 1.2). From the plot, it is clear that the linear dispersion curve of the k_x vector of light in free space does not intercept the SPP dispersion curve (see Figure caption). In practical terms this means that light cannot couple to the SPP excitation under normal conditions,

the k_x vector must be enhanced through optical coupling techniques such as prism and grating coupling to generate propagating SPPs.

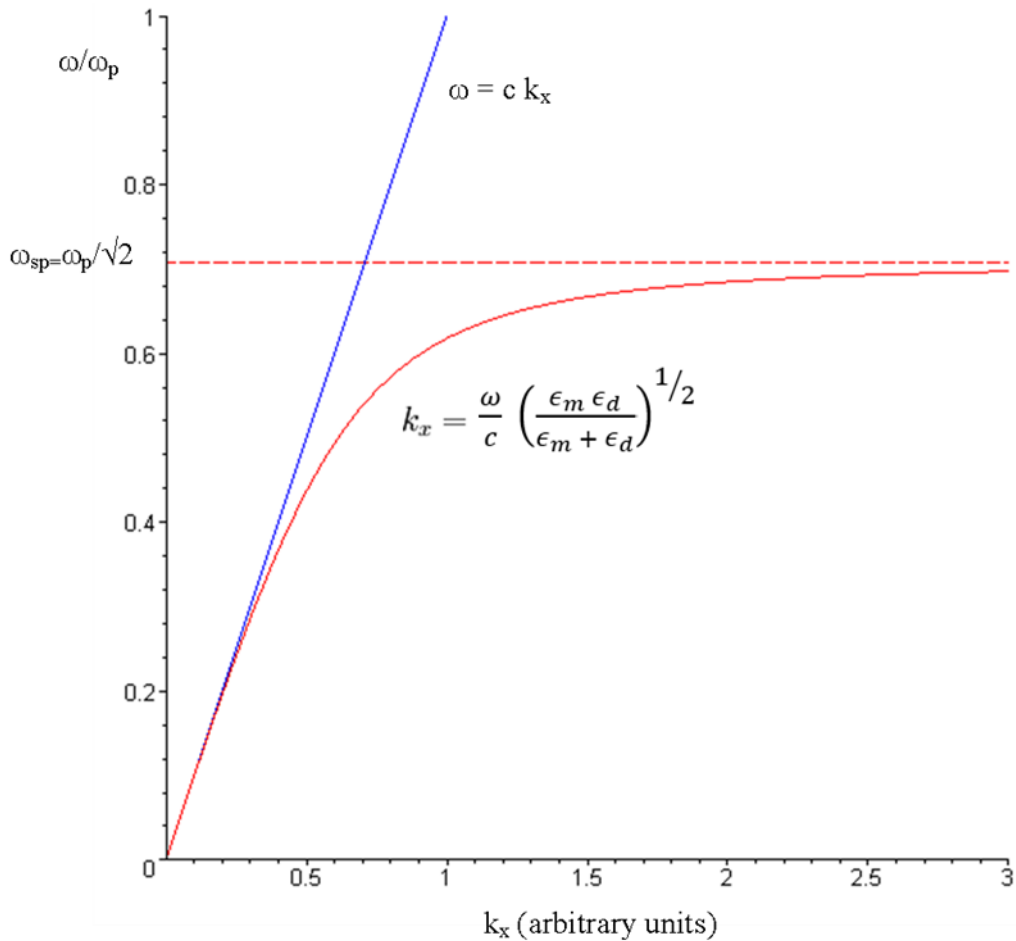


Figure 1.2. Surface Plasmon Polariton Dispersion Curve. For light in a vacuum $\omega = ck_x$. The dispersion curve relates oscillation frequency, ω , to the x component of the wave vector, k_x . The dispersion curve describes how momentum changes with frequency. The relative permativity of the dielectric, ϵ_d , is equal to 1 (vacuum) in the above plot.

Prism coupling of SPPs

Two prism coupling techniques, the Kretschmann configuration and the Otto configuration (Figure 1.3), are commonly used to overcome the momentum deficit of photons incident at a plasmonic metal dielectric planar interface described in Figure 1.2. The two techniques are both conceived to provide photons propagating through a prism with a dielectric constant that is higher than the that of the dielectric overlayer at the

metal surface with a momentum increase, to match the larger momentum component of the SPP along the x -direction (Figure 1.4). This momentum increase appears at angles larger than that required for total internal reflection (TIR) within the prism, and results from the creation of an evanescent wave propagating in the metal/dielectric interface.

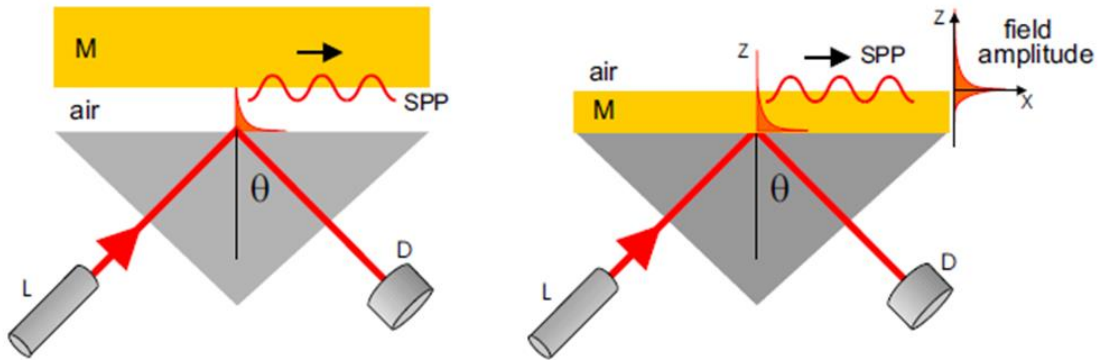


Figure 1.3. Left: Otto configuration and Right: Kretschmann configuration (reprinted with permission from reference 1)

In both cases the photons travelling through the high index of refraction prism have an altered dispersion relation that bends the slope of the frequency dependent k_x vector of the incident light and allows resonant excitation of the propagating SPP mode (Figure 1.4). In this work, the Otto configuration was selected as the method used to excite SPPs in order to improve the ease of fabrication and quality of the resultant photovoltaic devices (See Chapter 3).

Otto developed a semiquantitative theory demonstrating that for a given wavelength, photons with p -polarization, propagating through a prism with an index of refraction, n_p , greater than that of a spacer dielectric layer, n_s , there exists a range of angles that allow the excitation of an SPP at the spacer dielectric/metal interface. He further calculated the thickness of the spacer layer that allowed the maximum degree of incident photon absorption, and the minimum “halfwidth” or full width half maximum (FWHM), in modern parlance, of the absorption peak. Here, Otto coupling is achieved through the deposition of 3 thin film layers on a single-crystal TiO_2 prism (Figure 1.5). The first layer is comprised of conducting Al-doped zinc oxide (dZnO), the second, a semiconducting n-type zinc oxide (ZnO) layer, and finally, a silver top contact layer.

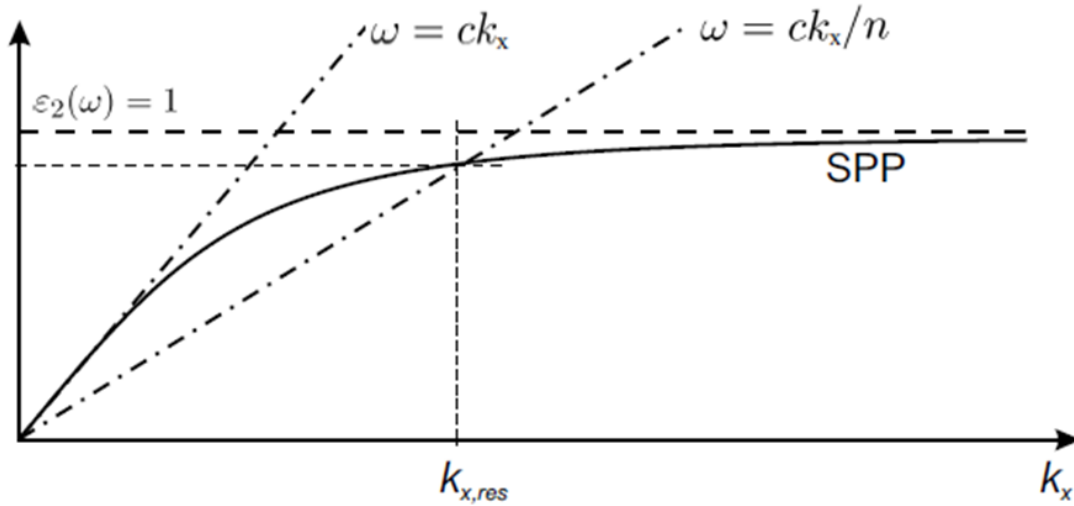


Figure 1.4. Dispersion curve depicting energy and momentum matching conditions for prism coupling of SPPs. (reprinted with permission from reference 1)

The degree of SPP coupling was modeled according to the Otto coupling requirements (Figure 1.5). From the simulated data, the maximum coupling, which corresponds to the reflection minima in Figure 1.5b, is seen to depend on the angle of incidence of incoming photons and the thickness of the dielectric spacer layer(s). The peak shape in Figure 1.5c shows the change in FWHM with dZnO/ZnO spacer thickness. 2% aluminum doped zinc oxide is here denoted dZnO. The narrowest peaks occur at the angle and thickness of maximum absorption.

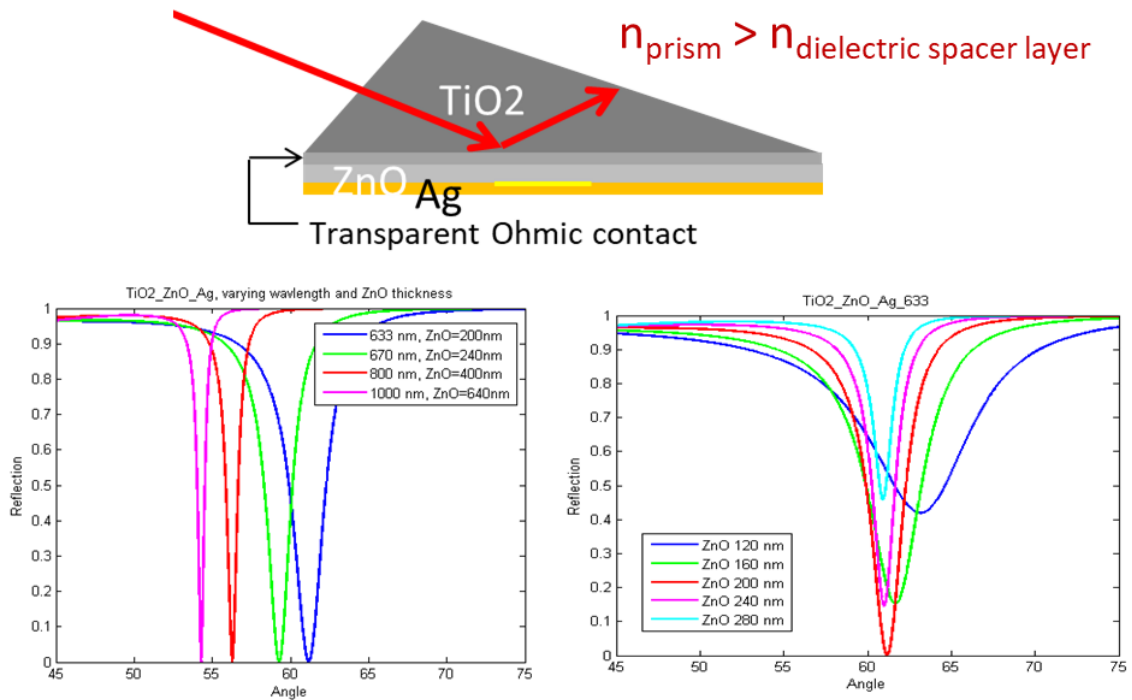


Figure 1.5. Otto coupling to photovoltaic prism devices. a) a device cartoon, b) simulated SPP coupling maxima for different ZnO film thicknesss c) peak shape at 633 nm for different ZnO thicknesses

SPPs propagate along the interface and decay into the metal and dielectric overlayer with a characteristic $1/e$ decay length that depends on the fully developed imaginary parts of the z momentum vectors ($1/k_{SPPz,m}$, $1/k_{SPPz,d}$). Typically, these values are in the range of 23 nm into the silver and a few hundred nanometers into the dielectric overlayer, depending on the overlayer refractive index. The $1/e$ decay length of SPPs propagating along the metal/dielectric interface in the x -direction depends on the imaginary component of the fully calculated k_{SPPx} vector. The propagation distance depends heavily on the material properties and surface quality of the metal, and for silver can range from a few microns to more than a hundred microns⁶ (Figure 1.6). SPPs propagate with a group velocity, v_g less than the speed of light, c^2 .

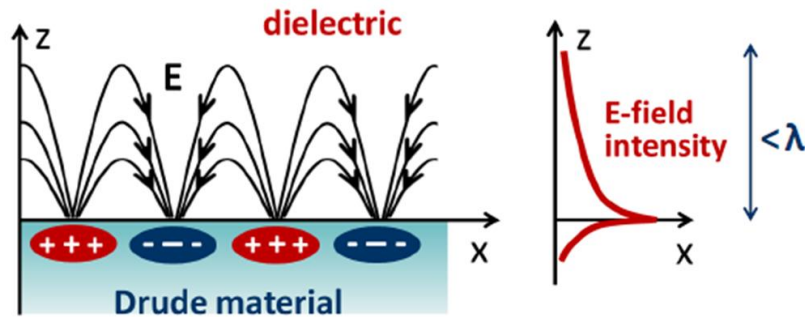


Figure 1.6. SPP electric field decay lengths propagating in the x direction.

SPPs are polaritons arising from strong coupling of a surface plasmon and a photon. In the work described here, the SPP geometry has been exploited to provide a direct measure of the potential use of plasmon excitation for hot carrier capture in a geometry that provides near unit light coupling efficiency to surface plasmons and that is not complicated by light scattering effects. This geometry provides a means of direct quantification of hot electron yield following plasmonic excitation, and a means to establish structure-function relationships that will lead to improved efficiency of plasmonic photovoltaics and other hot carrier-based devices. However, the restrictive geometries required to achieve the momentum and energy matching conditions required for efficient SPP generation limit the broader applicability of SPPs in practical situations. To overcome these challenges, the SPP-based platform described above has been extended to take advantage of the free space coupling of photons to surface plasmons through nanostructured plasmonic interfaces using a lattice resonant surface plasmon (LRSP) coupling strategy.

1.1.2. Locally Resonant Surface Plasmons

Locally resonant surface plasmons arise from direct excitation of surface plasmons and do not require the formation of a polariton at the surface of the metal/dielectric interface. Lattice resonant LRSPs are generated at nanostructured surfaces that have been patterned with arrays of plasmonically active surface features¹. In this work hexagonally patterned arrays of silver pillars are fabricated to generate an LRSP active surface. LRSPs can be excited by the free space coupling of incident photons directly to resonant plasmonic modes, greatly enhancing the possibilities for useful device designs and for applications in plasmonics.¹

Lattice resonant surface plasmons arise from the resonant coupling of light to individual localized surface plasmons (LSPs). LSPs are non-propagating surface plasmons resonantly excited in metals with boundary conditions that greatly constrain the metallic electron motion over that of the bulk metal. Of particular importance to the present work is the excitation of LSPs at plasmonic metal nanostructured surfaces, but the plasmonic excitation of symmetrical spherical nanoparticles provides a more convenient avenue towards a practical understanding of the phenomena.

For small nanoparticles, with diameters below the electric field penetration skin depth of the metal (~ 25 nm for silver at optical frequencies), electric fields can penetrate the entire particle and the plasma frequency cannot be calculated in the same way as for a bulk metal. Instead, the entire volume of free electrons within the particle are constrained by the surface. In the presence of an oscillating electric field, electrons are displaced to one side of the particle and a restoring potential is generated in the form of a dipole across the particle. The harmonic oscillation, with a period of τ , of this electron motion is what gives rise to the LSP (Figure 1.7).

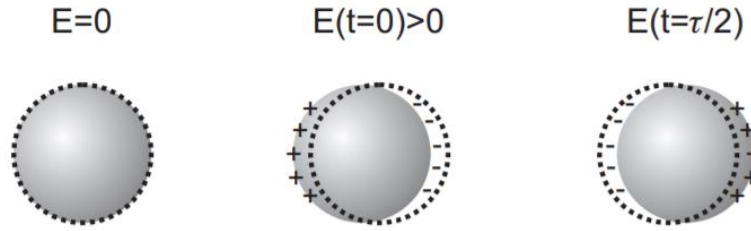


Figure 1.7. The harmonic oscillation of a plasmonic nanoparticle under the influence of an external field.

Using a quasi-static approximation for the electric field of the incoming photon, a Laplacian treatment of the potentials associated with LSP excitation of a sphere gives rise to an expression for the polarizability of the nanoparticle derived from its calculated dipole ². The polarizability, α , of the sphere is given by:

$$\alpha = 4\pi\epsilon_0 a^3 \frac{\epsilon_m - \epsilon_d}{\epsilon_m + 2\epsilon_d} \quad (1.6)$$

where ϵ_0 is the permittivity of vacuum, a is the diameter of the nanoparticle, ϵ_m is the permittivity of the metal, and ϵ_d is the permittivity of the surrounding dielectric. When the

frequency-dependent value of ϵ_m approaches the value of $-2\epsilon_d$ the polarizability of the nanoparticle becomes large and the resonant condition for SLR excitation is met.

The energy of the incident beam is lost from the plasmon through scattering and absorption, which together are called extinction. Both processes depend on the polarizability of the nanoparticle. The cross sections of these two processes, which are a measure of their probability, can be calculated by dividing the total radiated power of the dipole over the intensity of the exciting field for the scattering cross section, and using Poynting's theorem of power dissipation⁶ to arrive at the expressions:

$$\sigma_{scatt} = \frac{8\pi}{3} k^4 a^6 \left| \frac{\epsilon_m - \epsilon_d}{\epsilon_m + 2\epsilon_d} \right|^2 \quad (1.7)$$

$$\sigma_{abs} = 4\pi k a^3 \text{Im} \left(\frac{\epsilon_m - \epsilon_d}{\epsilon_m + 2\epsilon_d} \right) \quad (1.8)$$

where σ is the cross section, and k is the wave vector of the plasmon. For the absorption cross section, the imaginary parts of the permittivity are used in the calculation.

From Equations 1.7 and 1.8, it can be seen that the LSP scattering probability depends on the diameter of the particle to the sixth power, a^6 , and that the absorption probability depends on the smaller value of a^3 . This dependence is observed experimentally in the fact that larger nanoparticles tend to scatter more light than smaller nanoparticles, giving rise to a vibrant and varied colour pallet of plasmonic nanoparticles dependent on size and shape⁶. It is interesting to note that plasmonic nanoparticles have been used as decorative colouration since ancient Roman times. The most famous example of which is the Lycurgus cup (Figure 1.9), which, when illuminated from behind appears red because of the green absorption of nanoparticles in transmission, but green where the surface relief makes the scattered green component of the extinction visible.



Figure 1.8. Green absorption and green scattering from the plasmonic gold nanoparticle decoration of the Lycurgus cup (reprinted with permission from reference 1)

Isolated plasmonic nanostructures are polarizable structures that support characteristic oscillating dipole moments when excited at their resonant frequencies. In many ways this is analogous to the case for polarizable molecules. Well organized arrays of plasmonic nanostructures can be examined from this perspective as a metamaterial, a nanostructured surface geometry whose aggregate properties can be understood in ways that approximate bulk material lattices. A plasmonic metamaterial's properties arise from the aggregate contributions of its LSP-active constituents.

The absorption of plasmonic metamaterial arrays arises primarily from the coupling of the dipoles of the individual nanostructures. When the dipoles are taken together the absorption spectrum can be calculated using the coupled dipole approximation, CDA. The CDA approach was first developed to describe the mean polarizability of molecules in liquids and gases⁶ and the approach has been extended to the problem of plasmonic arrays of nanostructures¹.

CDA treats the polarization of each nanostructure as arising from the Equation:

$$\mathbf{P}_i = \alpha_i \mathbf{E}_{loc,i} \quad (1.9)$$

Where \mathbf{P}_i is the dipole polarization vector at position i , and $\mathbf{E}_{loc,i}$ is the local electric field vector that results from the incident photon and the sum of the contributions of the electric fields from the surrounding dipoles. For the case of an infinite symmetric array and assuming the polarizability at each position can be calculated according to Equation 1.6 the calculation of the polarization for each array position simplifies to:

$$P = \frac{E_0}{\frac{1}{\alpha} - S} \quad (1.10)$$

Where E_0 is equal to the field arising from the incident photon and S is the sum of the dipole contribution from the rest of the array. From the Equation it is evident that when the sum of the dipole contributions approaches the value of $1/\alpha$ the polarization of the nanostructures becomes large and the resonance condition for the plasmonic excitation of the lattice is met².

In the case of the work presented in Chapter 5, the plasmonically active silver nanostructured surface exhibits a complex absorption spectrum that arises from multiple possible modes of surface excitation that satisfy the combined dipole approximation for lattice resonant surface plasmon generation. From the perspective of a chemist, these complex interactions are best thought of as strong coupling that results in the mixing and splitting of energy levels, resembling the hybridization of atomic orbitals. The hybridization of individual plasmonic excitations leads to a familiar splitting of energy levels that is reflected in the field distribution of the surface plasmon excitation and ultimately in the absorption spectrum of the nanostructured lattice. For lattices of non spherical structures, such as those presented in Chapter 5 the absorption spectrum is further complicated by the fact that such features have angle dependent polarization properties that are reflected in the absorption spectrum of the surface (Figure 1.9)

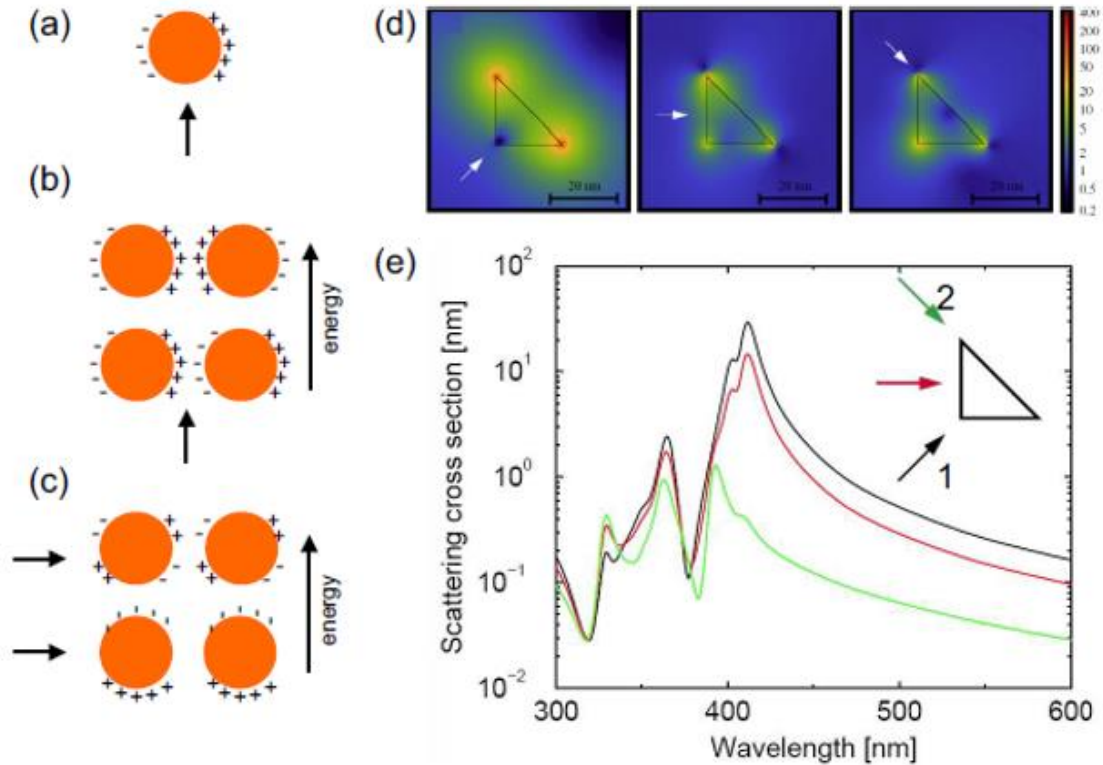


Figure 1.9. a,b,c) A single LSP excited nanoparticle. b) the splitting of excitation energies when a strongly coupled dimer is excited across the long axis of the dimer. c) along the the long axis d) A simulated triangular arrangement of LSP active centers from different directions (arrows). e) Simulated scattering from the structure in (d). (reprinted with permission from reference 1)

1.2. Surface Plasmon Decay

Both SPP and LRSP excitations have short lifetimes, on the order of tens of femtoseconds. Surface plasmons decay in two primary ways, through the scattering (re-emission) of a photon or by the creation of hot carriers (electron-hole pair generation) that coincides with material absorption.⁷ Both of these processes are the subject of intense study because of the broad range of optoelectronic phenomena they enable¹.

The scattering of surface plasmons has fueled the study of nano-optics allowing the manipulation of photons at subwavelength scales. Examples of advances enabled by surface plasmon scattering experiments include nanolenses⁸, nano-antennas⁹, new types of nanoscale lasers¹⁰ and enhancements in the efficiency of photovoltaics¹¹. The

study of surface plasmon scattering has also informed the design of other types of metamaterials, such as, all dielectric nano-optics that leverage the magnetic permeability of nanostructured materials like silicon to scatter light from collectively oscillating magnetically induced dipoles¹². These classes of materials are a focus because they have much lower losses than plasmonic materials, which have significant absorption losses from hot carrier generation.

Hot holes and hot electrons, collectively referred to as hot carriers, while considered to be a problem for nano-optic designs, are central to harnessing the energy of non-radiative surface plasmon decay within a metal. Hot electrons and hot holes are emitted when surface plasmons decay by intra- and interband electron transitions¹³. These transitions can either be direct, phonon-assisted, or surface-assisted (Figure 1.10)

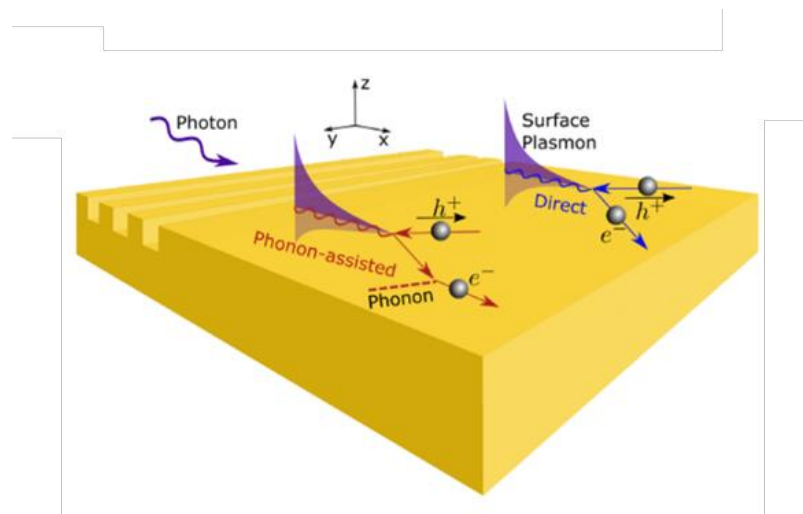


Figure 1.10. a) Cartoon of grating-coupled SPP decay generating hot carriers. Intra-band transitions can be surface- and phonon-assisted. Interband direct transitions are the most probable when photon energies are above the transition threshold, 3.4eV for silver. (adapted with permission from reference 13)

The different mechanisms of hot carrier generation have probabilities that depend on the energy of the metal's interband transition threshold. Below the threshold energy, phonon- and surface-assisted transitions dominate. Above the threshold, the probability of direct transitions dominates hot carrier generation from surface plasmon decay. For gold and copper the interband threshold is approximately 1.6-1.8 eV, giving

rise to their characteristic color through absorption at these energies. Silver has a higher threshold energy of ~ 3.4 eV¹³, and so it is very reflective across the optical spectrum.

The energy distribution of plasmonic hot carriers generated in coinage metals (Au, Cu, and Ag) has been well characterized.¹⁴ These metals, which are characterized by filled valence d-bands, whose energies reside well below the material's Fermi energy (E_F), and a diffuse sp-band with energies that extend from well below to well above E_F , exhibit large differences in the partitioning of excitation energy between holes and electrons depending on whether intraband or interband transitions occur (Figure 1.11).

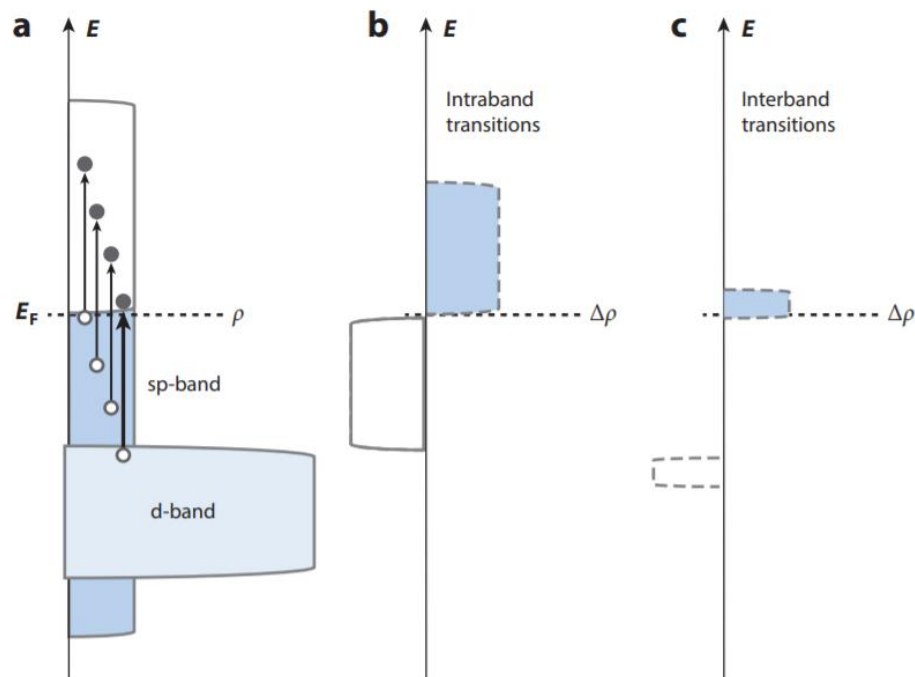


Figure 1.11. a) Simplified band diagram of silver, ρ is the equilibrium electron distribution. b) High energy hot electrons resulting from intra sp-band transitions. c) Low energy electrons and high energy holes resulting from interband transition from the d- to sp-band. (from ref 14)

For the case of silver, with a direct d to sp transition energy of ~ 3.4 eV it can be seen from Figure 1.11 that, for energies below that threshold, phonon- and surface-assisted transitions of electrons within the broad density of states (DOS) sp-band are excited into unoccupied levels well above the Fermi level. Conversely, at energies above

the threshold, direct transitions from the dense DOS d-band levels yield electrons with energies close to the Fermi level and hot holes with much higher energies.

This counterintuitive result means that harnessing the energy of hot carriers is more efficient for hot *electron* devices below the threshold for interband transitions, and that the opposite is true when harvesting energy from hot *holes* above the interband energy. Previous studies of silver nanoparticle covered surfaces, coated with evaporated discontinuous films from 0 to 1.2 nm deposition thickness (Figure 1.12), showed that the kinetic energy of photoemitted electrons from 2 photon photoemission (2PPE) experiments was dominated by sp-band emission, as predicted by the simplified band structure presented for illustrative purposes above.¹⁵ 2PPE is the study of electrons emitted from a material by two photon excitation (see Section 2.6).

The magnitude of the 2PPE from the plasmonic active nanostructured surface was seen to grow by 3 orders of magnitude over that of a flat silver film. The growing signals with deposition thickness from 0.1 to 0.9 nm results from the formation of discontinuous nanoparticles that precipitate on the surface of the substrate. The plasmonic absorption of the precipitated particles is seen to grow with size up to a steady state after 1.0 nm, corresponding to the 0.9 nm curve in Figure 1.12. 2PPE signals grow with the degree of plasmonic excitation. The energy distribution of hot electrons detected from 3.14eV photons, below the interband transition of silver, displays the hallmark energy distribution expected from the intraband transitions depicted in Figure 1.11b.

The underlying complexities that govern the energies of plasmonically generated hot carriers are not fully encompassed by this discussion as evidenced by the relatively narrow bandwidth of the sp-band emission spectrum of Figure 1.12 given the 3.14 eV photoexcitation energy. It is thought that prompt non-radiative decay mechanisms may cause the hot electrons to lose energy to thermalization processes between the first and second photon excitation, leading to the observed energy dependence of 2PPE emission intensity on kinetic energy. Though not flat, the spectrum justifies the assumption in Figure 1.11, that the DOS of the sp-band can be approximated by a diffuse continuum above and below E_f . Other effects, such as the presence of surface states, and chemical interface damping can enhance or suppress hot electron emission and must be considered when designing and analyzing the efficiency of hot electron

metal/n-type semiconductor plasmonic photovoltaics that are the focus of this work.¹⁶ Chemical interface damping has been observed to mediate charge transfer from plasmonically excited metals directly to strongly coupled surface states. Transient absorption³³, and photoelectrochemical³⁴ studies of TiO₂-gold nanoparticle structures exhibit quantum efficiencies that avoid electron transport losses.

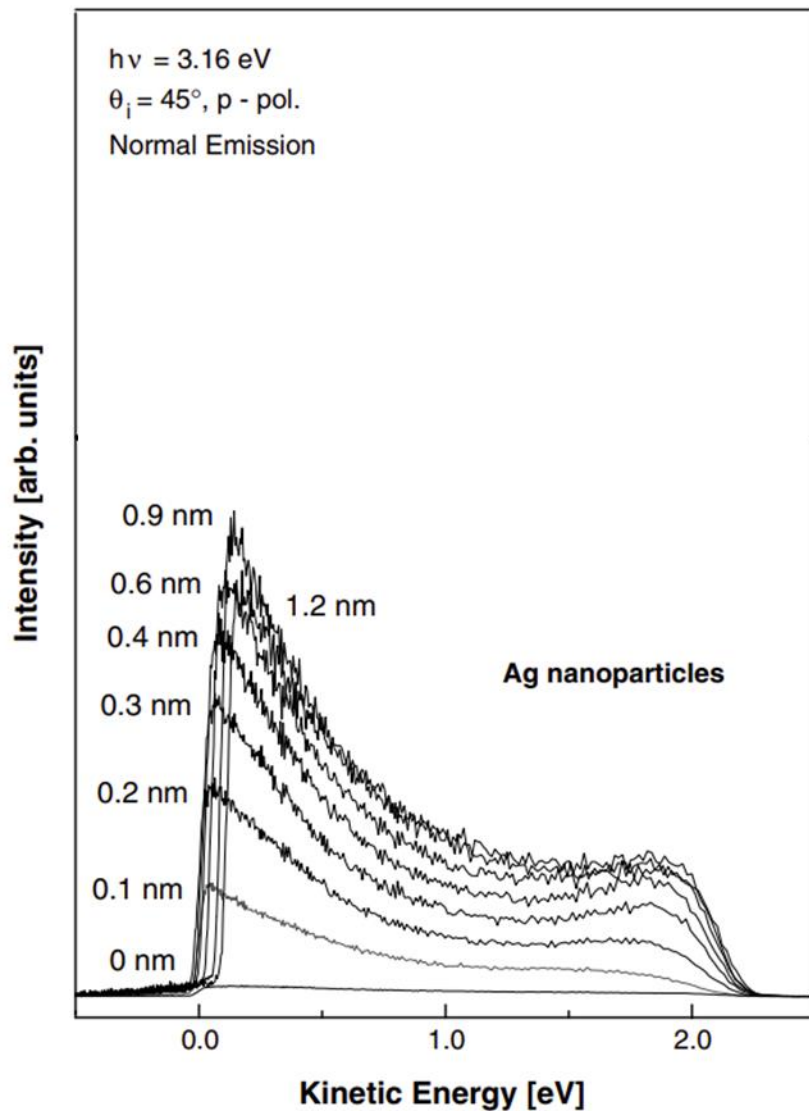


Figure 1.12. The kinetic energy of 2PPE generated electrons with increasing silver nanoparticle size under 3.16eV illumination (reprinted with permission from reference 15).

1.3. Schottky Junctions

The development of efficient plasmonic photovoltaics depends on three processes: 1) the absorption of photon energy through plasmonic excitation of the metal 2) the conversion of the plasmon excitation into energetic charge carriers and 3) the separation of charge to generate a voltage that can do work. The previous 2 sections introduced the concepts governing the first two processes. Here we discuss the details of the charge rectification element of plasmonic PV device design.

Though examples of plasmonic hot carrier charge separation using metal insulator metal (MIM) diode rectifiers¹⁷, and nascent progress towards 90+% efficient devices that operate by an elastic tunneling mechanism analogous to a microwave rectenna, have been reported¹⁸, the majority of plasmonic PV and sensor literature focuses on rectification across metal semiconductor Schottky junctions^{19,20,21}.

A Schottky junction is an interface between a metal and a semiconductor, where a barrier to the flow of charge forms as the Fermi levels (chemical potentials) of the system equalize. This process can be understood according to the following description. When a metal with a work function, Φ_M , comes into contact with a semiconductor with an electron affinity, X_{SC} , where X_{SC} is the energy difference between the conduction band and the energy of an electron in vacuum, charges move to equalize the Fermi energies of the system. This results in the bending of the semiconductor conduction and valence band energies in the region near the interface, creating a barrier to the flow of charge. In the case of an n-type semiconductor, considered in this work, the band diagram is depicted in Figure 1.13.

In the case of n-type semiconductors, such as the intrinsically doped n-type zinc oxide considered in this work, electrons residing in defects just below the conduction band define the Fermi energy of the material. Upon contact with the metal, electrons flow through the conduction band to the lower energy metal across the interface to equalize the Fermi energies of the two materials. This has the effect of depleting the charge carriers from the semiconductor region near the metal, forming a so-called depletion region. The concentration of negative charge in the metal at the interface creates an electric field that raises the energies of the conduction and valence bands within that region, in a process known as band bending. Band bending results in formation of a

Schottky barrier, Φ_B , to the conduction of electrons from the semiconductor to the metal with a barrier energy equal to:

$$\Phi_B = \Phi_M - X_{SC} \quad (1.11)$$

where Φ_M is the work function of the metal.

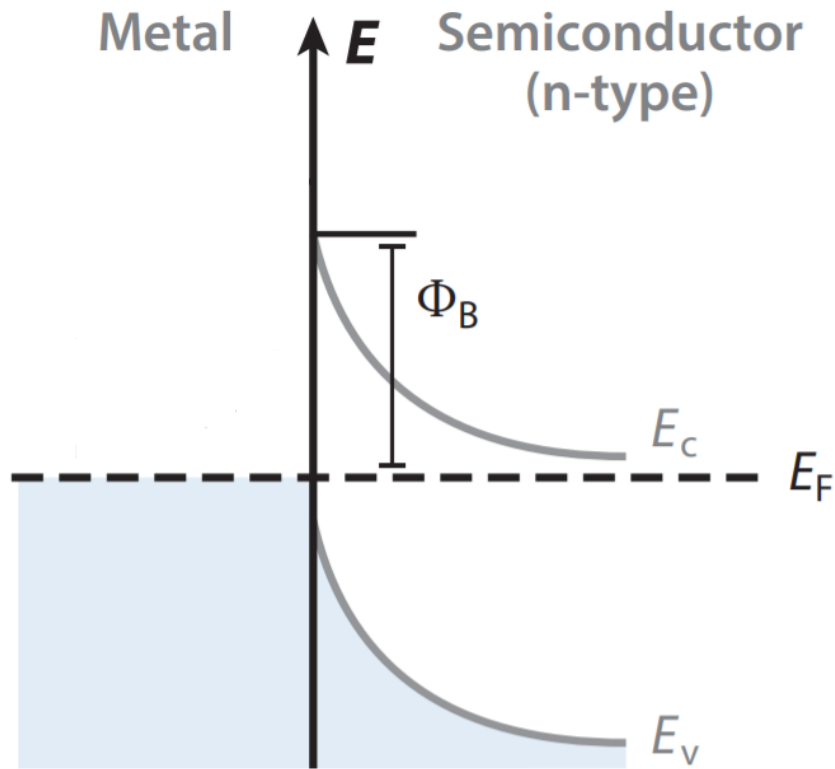


Figure 1.13. Band bending of an n-type semiconductor metal junction. E_V is the energy of HOMO, E_C is the energy of the LUMO (adapted from ref 14)

When a low positive voltage is applied to the metal side of the junction, electrons liberated from their low-lying n-type levels are prevented from flowing across the junction by the Schottky barrier. As the positive potential on the metal is increased the resultant buildup of negative charge in the semiconductor raises the energy of the conduction and valence bands. At the “turn-on” voltage of the junction, the band bending in the depletion region is almost completely reversed and electrons can flow from the semiconductor into the metal at a rate determined by thermionic emission (Figure 1.14). Diode properties are further described in Section 2.4.1.

Conversely, when a positive potential is applied to the semiconductor side of the junction, the energy of the conduction and valence bands is lowered. Electrons cannot flow from the metal to the semiconductor because the Schottky barrier at the interface is unaffected by the lowering of the semiconductor energy levels. At high voltages the effective width of the depletion region can be reduced by the extreme drop in the semiconductor band energies giving rise to a reverse tunneling current. Junctions under extreme potentials can suffer from dielectric breakdown and become ohmic contacts.

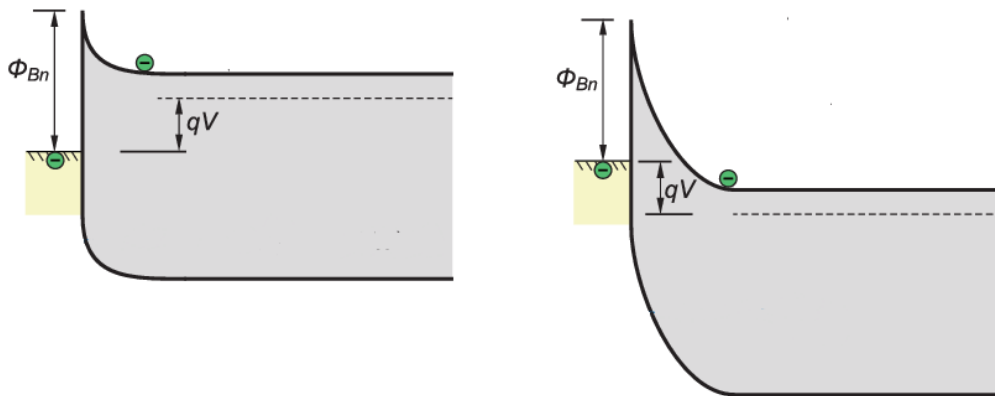


Figure 1.14. Schottky barrier under forward (left) and reverse (right) bias (V)

Schottky junctions can be formed from the contact of a variety of metals and semiconductors, but this work is focused on the particular properties of silver/zinc oxide contacts.

Zinc oxide is a wide bandgap (3.37eV) semiconductor with an electron affinity of ~4.2 eV. Though it can be found in the cubic zincblende form, its more common wurtzite structure gives it a non-centrosymmetric unit cell that can form either an oxygen polar or zinc polar surface (Figure 1.15). Zinc oxide is typically n-type as deposited because of its strong tendency to form low lying defects that can donate electrons to the conduction band. Previously, the origin of these n-type defects was thought to be oxygen vacancies²², but more recent studies have shown that the source of the low-lying defects is more complex. Intense interest in engineering ZnO with p-type character has led to

extensive research into the origin and control of defect formation during deposition. Current research indicates that hydrogen incorporated into the lattice behaves as an easily diffusing dopant or as a substitute for O in the lattice, accounting for ZnO n-type stability at elevated temperatures, where as interstitial H might be expected to diffuse out of the lattice²². Other impurities, such as Ga, Al, and In have been identified as potential shallow-donors, and may be present under the sputtering conditions discussed in Chapter 2.

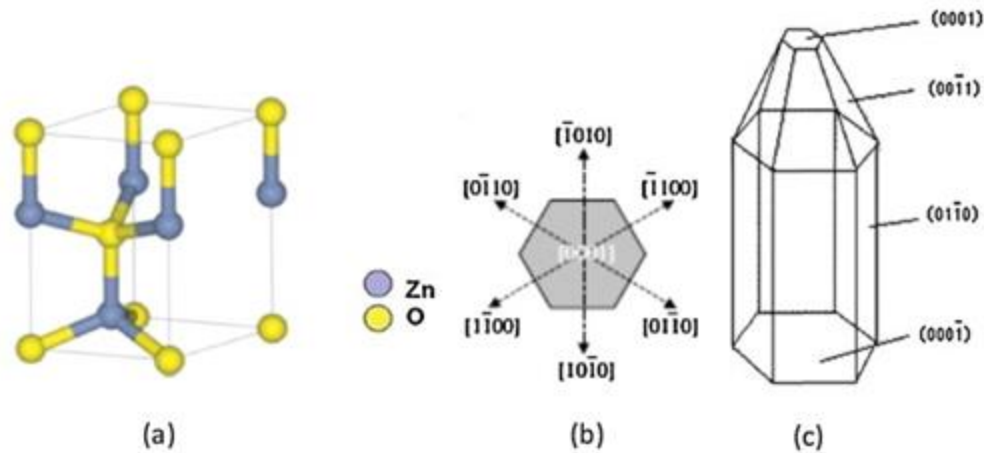


Figure 1.15. The crystal structure of wurtzite ZnO (adapted from ref 23)

Given that literature values for the work function of silver range from 4.26eV to 4.73²⁴, it appears from Equation 1.11 that the silver/ZnO contact should form a junction with a very low barrier, depending on the energy of the ZnO Fermi energy defined by the n-type donor levels. Counterintuitively, the Ag/ZnO contact gives rise to a Schottky diode with barrier heights typically measuring between 0.68eV and 1.1eV²⁵. In this work, the barrier heights of the Schottky devices tested were in the range of 0.5eV to 0.9eV, but many failed devices had ohmic junctions and great care was needed to observe diode behaviour repeatably.

Understanding this contradictory behaviour requires a discussion of the role of surface states, surface cleanliness, and silver interface oxidation on junction properties. Investigators have found that the formation of silver oxide at the junction has the effect of lowering the work function of the metal by 0.45eV²⁶, leading one to think that surface

oxidation may be necessary at the interface to generate a mismatch more amenable to junction formation. The adjusted work function value in the presence of a silver oxide interlayer is in the range of what is expected from Equation 1.11.

Surface cleanliness and treatments have also been found to be of critical importance to high quality junction formation²⁶. Because the interface is sensitive to contamination and the near surface region of zinc oxide can adsorb oxygen readily and deplete the near surface of electrons through charge transfer, ZnO Schottky barriers are highly variable when vacuum is broken during sample transfer between ZnO and Ag deposition (see Section 2.1.2).

Under these conditions, surface states and interface charges can screen the potential of the metal through the introduced dipoles giving rise to barrier heights that are insensitive to the metal work function. When surface states near the fermi level are prevalent, then applied voltage will simply charge the surface states, creating a surface dipole rather than the charge distribution in the depletion region. The presence of such surface states generates a junction with a “pinned” barrier. When the interface is thin enough, electrons can tunnel through the junction and in the extreme case the contacts become Ohmic. According to the Bardeen model²⁶, under these conditions, Equation 1.11 is modified by a factor $\Delta\chi$ representing the effect of interface dipoles and the Schottky barrier is modified to a new value ϕ_{SB}' (Figure 1.16)

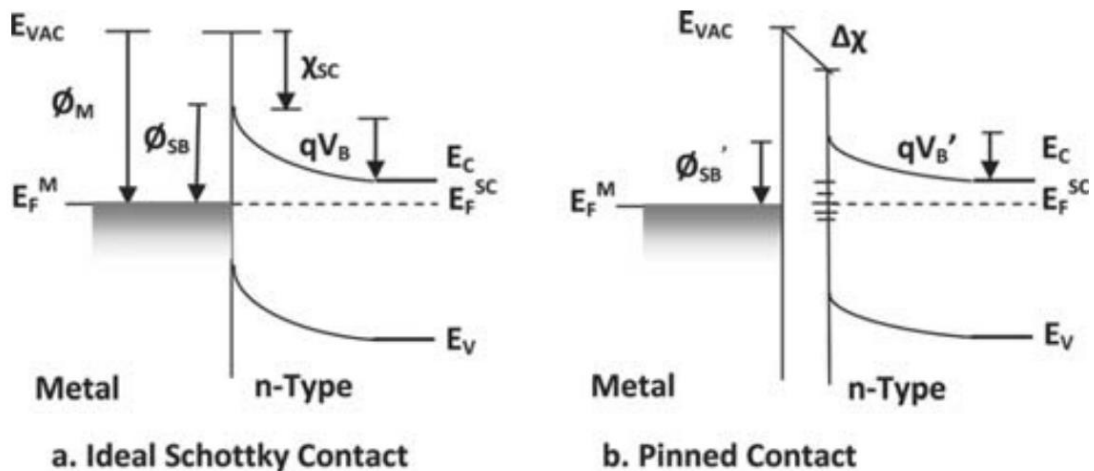


Figure 1.16. Schottky contact a) under ideal conditions, and b) pinned by interface dipoles (reproduced from ref 26).

When zinc oxide is intentionally doped with an element such as Al or In, the result can be a transparent conducting oxide (TCO) that has such a high number of shallow n-type donors that the material becomes conducting and has a low contact resistance to metals. Doped zinc oxide (dZnO) forms the back contact for the devices presented in Chapter 3 and the top contacts for the devices presented in Chapter 5. The diodes fabricated in this work are further explored in Chapter 2.

1.4. Internal Photoemission

The final step in the plasmonic photovoltaic mechanistic chain is internal photoemission (IPE). Hot electrons generated by plasmon decay that have energy greater than the Schottky barrier height, have a probability of being photoemitted from the silver into the conduction band of the zinc oxide where they can be rectified with a voltage equal to the barrier height minus the energy between the quasi-Fermi energy of the semiconductor and the bottom of the conduction band multiplied by the elementary charge of an electron. This is called the built-in potential V_b . Typically for ZnO the donor level is only 50 or 60 meV below the conduction band²² so $qV_b = \Phi_b - 50\text{meV}$, where q is the elementary charge of an electron. In the case of the devices presented in this work, the maximum rectifying voltage is therefore close to the value of the barrier height. Positive hot carriers, known as “hot holes”, can also undergo photoemission, though the details of these types of devices are not presented here⁷. The focus of the present work is on hot electrons.

The previous two sections, through the introduction of non-radiative plasmon decay, and the Schottky junction, play an important role in understanding the ultimate efficiency limits of plasmonic photovoltaics that operate by the internal photoemission mechanism. .

Hot electrons generated by plasmon decay are emitted according to the principles discussed in Section 1.3. These energetic electrons must cross the Schottky barrier in order to be rectified as a voltage that can do work. Only hot electrons with energy greater than Φ_B have any probability of crossing the barrier. From the discussion of Figure 1.11, this means that high efficiencies are achieved at incident energies that favour intraband transitions rather than at higher energies where interband direct transitions dominate. From Section 1.2, interband transitions from the d-band, deep

below the Fermi level, injects low energy hot electrons into the s-p band near the bottom of the conduction band with too little momentum to undergo IPE. Even in the case where intraband transitions dominate, because of the observed broad spectrum of possible intraband transitions that give rise to high energy hot electrons, many of the excited electrons will not have enough energy to be emitted (Figure 1.11a). Theoretical treatments of the efficiency limits of IPE for small nanoparticles have calculated the probability of electron emission according to a free electron gas model where the electron density of states (DOS) is assumed to be proportional to $E^{1/2}$ for hot electrons with energy above the conduction band of the metal²⁷. These simplified electron distribution joint density of states (EDJDOS) calculations give rise to a picture of IPE under idealized conditions (Figure 1.17), where every energetic electron excited by an intraband transition that has sufficient energy undergoes IPE.

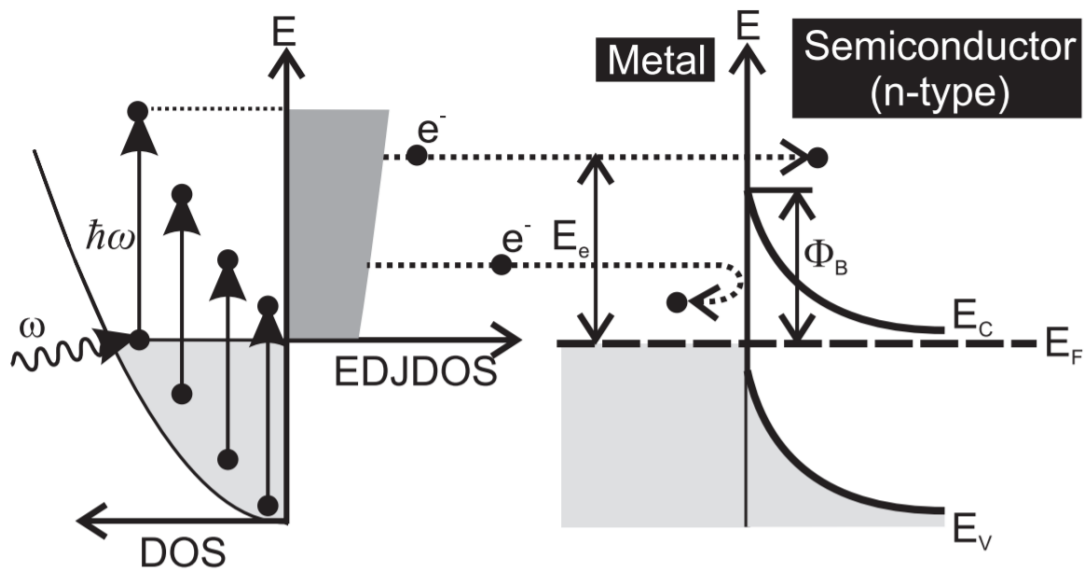


Figure 1.17. (left) Band diagram of a theoretical nanoparticle undergoing intraband plasmonic excitation of hot electrons, showing the distribution of energies as a function of EDJDOS (right) The interaction of hot electrons with the barrier. Electrons with energy $< \Phi_B$ are reflected. (adapted with permission from reference 27)

From the above model it is possible to calculate the maximum efficiency of internal photoemission from a plasmonic photovoltaic under solar illumination to be limited to 7.4% power conversion efficiency (PCE), assuming a continuous density of

states below the Fermi level. According to this simplified model, at single wavelengths above the energy of the barrier, IPE efficiencies can reach as high as 70% quantum efficiency (QE) at photon energies corresponding to 4 times the barrier height.

In practice, not only does the energy of the hot electron determine its probability for injection into the adjacent dielectric material, but so does its initial momentum. Electrons emitted by plasmon decay possess a momentum associated with its direction of propagation. Only the component of the electron momentum normal to the junction interface contributes to the emission process. For planar device geometries this calculation can be made through the introduction of the Scales “escape cap” model for a planar metal semiconductor Schottky junction³². The basis of this model is depicted in Figure 1.18. The image depicts a hot electron with an energy, E_d , where $E_d > \Phi_b$ and with a momentum, k_Ω . The sphere represents the surface of all possible propagation directions of the hot electron and its momentum vector. The ordinate k_x represents the direction of the metal semiconductor surface normal and $k_{x,e}$ is the momentum vector representing the minimum energy necessary to surmount the Schottky junction barrier. The key insight of the Scales model is that for any momentum k_Ω the angle Ω is that largest angle for which the component $k_{\Omega,x}$ is larger than Φ_B and the electron can overcome the barrier. The angle Ω can be found from the relation:

$$k_{x,e} = k_\Omega \cos \Omega \tag{1.12}$$

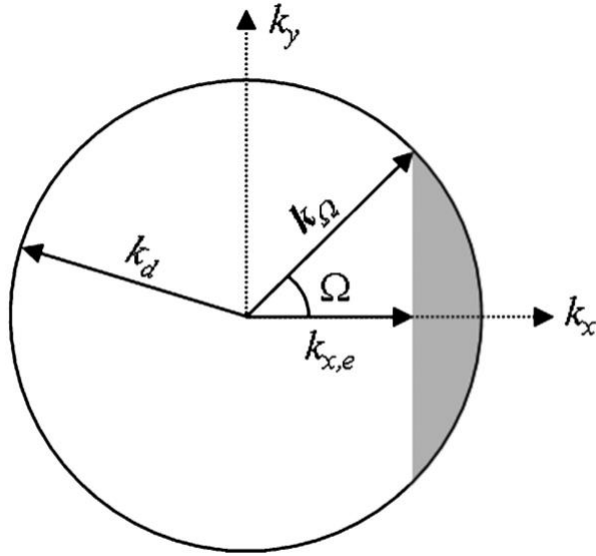


Figure 1.18 The escape cap model momentum diagram. (reprinted with permission from reference 32)

Recognizing the symmetry around the x axis in Figure 1.18, the momentum constraint allows the construction of a cone of angles where an electron of energy E_d will have sufficient momentum to escape. The probability of an electron being emitted in this direction is then simply the ratio of the solid angle of the escape cone to the solid angle of the complete k_Ω momentum sphere. Which is given by:

$$P(E_d) = \frac{1}{2} \left(1 - \sqrt{\frac{\phi_B}{E_d}} \right) \text{ (for } E_d > \phi_B \text{)} \quad (1.13)$$

Where $P(E_d)$ is the probability of IPE. Though Equation 1.13 is only valid for planar junctions, the mechanistic approach can be qualitatively extended to nanostructured surfaces. A three-dimensional interface with a size scale on the order of the mean free path of a hot carrier would allow a larger number of electrons with momentum k_Ω to overcome the Schottky barrier because emitted electrons would have a greater chance of possessing a sufficient momentum component in the direction normal to the interface. In the ideal case of an isolated small plasmonic metal sphere, almost all electrons will meet the interface with a well aligned momentum vector and a QE of 70% is possible for electrons with energies of 4 times the barrier height.²⁷

The probability of emission is always further lowered from the theoretical maximum by electrons that scatter their energy through thermalization processes. Hot

electrons scatter their energy through electron-electron and electron-phonon collisions until their energy is lost to the phonon bath as heat within the metal. Only electrons that retain sufficient energy to surmount the barrier can contribute to the photovoltaic current. Decay times within the metal are related to the mean free path of the electrons, in silver this is typically 50 nm, and scattering processes are energy dependent, occurring on characteristic timescales of 1 to 100 femtoseconds for electron-electron collisions and in the 1 to 10 picosecond range for electron-phonon scattering.^{28,29} Hot electrons, with energies >1eV above the Fermi energy, lose their energy to electron-electron scattering very quickly and must be emitted close to the Schottky interface to undergo IPE.

Internal photoemission of hot electrons, informed by the above discussion, can now be considered in terms of the energy dependent quantum efficiency of the process. This dependence was previously derived for infrared detectors³⁰ and is expressed by the Fowler relation:

$$\eta_e = C \frac{(hv - \Phi_B)^2}{hv} \quad (1.14)$$

Where η_e is the external quantum efficiency, h is Planck's constant, and ν is the frequency of the incident photon, $h\nu$ is equal to the energy of the absorbed photon and the resultant hot electron. The external quantum efficiency, η_e , is calculated from the internal quantum efficiency defined to be:

$$\eta_i = \frac{I_{sc}/q}{P_{abs}/h\nu} \quad (1.15)$$

where η_i is the *internal* quantum efficiency of IPE, I_{sc} is the measured short circuit photocurrent, P_{abs} is the light power coupled into the device, and q is the elemental charge of an electron. The external quantum efficiency is simply η_i multiplied by the fraction of incident power absorbed. If η_e is measured by experiment at different wavelengths of illumination, then, from 1.12, a plot of $\sqrt{\eta_e \times h\nu}$ versus incident energy gives a straight line with a y -intercept at Φ_b . For the planar devices presented in Chapter 3 see Figure 3.13 for the experimentally derived Fowler relation which establishes the IPE mechanism of plasmonically enhanced photovoltaic current generation.

The study of plasmonic hot carrier generation is a subject of intense and continuing interest³¹. Advances toward high efficiency devices require not only an understanding of the principles presented here, but an experimental platform that enables quantitative measurements of, plasmonic excitation, plasmon decay, the transport of hot carriers near an interface, and the internal photoemission yield of hot electrons across the interface. The focus of this work is to develop such an experimental platform towards a deeper understanding of plasmonic hot carrier dynamics and device design.

References

- 1 Novotny, L. and Hecht, B., 2012. *Principles of nano-optics*. Cambridge university press. Li, Y., 2017. Plasmonic optics: Theory and applications. Society of Photo-Optical Instrumentation Engineers (SPIE).
- 2 Maier, S.A., 2007. *Plasmonics: fundamentals and applications* (Vol. 1, p. 245). New York: Springer.
- 3 Willets, K.A. and Van Duyne, R.P., 2007. Localized surface plasmon resonance spectroscopy and sensing. *Annu. Rev. Phys. Chem.*, 58, pp.267-297.
- 4 Mejía-Salazar, J.R. and Oliveira Jr, O.N., 2018. Plasmonic biosensing: Focus review. *Chemical reviews*, 118(20), pp.10617-10625.
- 5 Zayats, A.V., Smolyaninov, I.I. and Maradudin, A.A., 2005. Nano-optics of surface plasmon polaritons. *Physics reports*, 408(3-4), pp.131-314.
- 6 Staelin, D.H., 2011. *Electromagnetics and applications* (pp. 1-442). Massachusetts Institute of Technology.
- 7 Khurgin, J.B., 2020. Fundamental limits of hot carrier injection from metal in nanoplasmonics. *Nanophotonics*, 9(2), pp.453-471.
- 8 Chen, X., Huang, L., Mühlenbernd, H., Li, G., Bai, B., Tan, Q., Jin, G., Qiu, C.W., Zhang, S. and Zentgraf, T., 2012. Dual-polarity plasmonic metalens for visible light. *Nature communications*, 3(1), pp.1-6.
- 9 Liu, Z., Boltasseva, A., Pedersen, R.H., Bakker, R., Kildishev, A.V., Drachev, V.P. and Shalaev, V.M., 2008. Plasmonic nanoantenna arrays for the visible. *Metamaterials*, 2(1), pp.45-51.
- 10 Song, P., Wang, J.H., Zhang, M., Yang, F., Lu, H.J., Kang, B., Xu, J.J. and Chen, H.Y., 2018. Three-level spaser for next-generation luminescent nanosensor. *Science advances*, 4(8), p.eaat0292.
- 11 Enrichi, F., Quandt, A. and Righini, G.C., 2018. Plasmonic enhanced solar cells: Summary of possible strategies and recent results. *Renewable and sustainable energy reviews*, 82, pp.2433-2439.
- 12 Cai, W. and Shalaev, V.M., 2010. *Optical metamaterials* (Vol. 10, No. 6011). New York: Springer.
- 13 Brown, A.M., Sundararaman, R., Narang, P., Goddard III, W.A. and Atwater, H.A., 2016. Nonradiative plasmon decay and hot carrier dynamics: effects of phonons, surfaces, and geometry. *ACS nano*, 10(1), pp.957-966.

- 14 Christopher, P. and Moskovits, M., 2017. Hot charge carrier transmission from plasmonic nanostructures. *Annual review of physical chemistry*, 68, pp.379-398.
- 15 Evers, F., Rakete, C., Watanabe, K., Menzel, D. and Freund, H.J., 2005. Two-photon photoemission from silver nanoparticles on thin alumina films: Role of plasmon excitation. *Surface science*, 593(1-3), pp.43-48.
- 16 Kale, M.J. and Christopher, P., 2015. Plasmons at the interface. *Science*, 349(6248), pp.587-588.
- 17 Hobbs, P.C., Laibowitz, R.B., Libsch, F.R., LaBianca, N.C. and Chiniwalla, P.P., 2007. Efficient waveguide-integrated tunnel junction detectors at 1.6 μm . *Optics express*, 15(25), pp.16376-16389.
- 18 Donchev, E., Pang, J.S., Gammon, P.M., Centeno, A., Xie, F., Petrov, P.K., Breeze, J.D., Ryan, M.P., Riley, D.J. and Alford, N.M., 2014. The rectenna device: From theory to practice (a review). *MRS Energy & Sustainability*, 1.
- 19 Mubeen, S., Lee, J., Lee, W.R., Singh, N., Stucky, G.D. and Moskovits, M., 2014. On the plasmonic photovoltaic. *ACS nano*, 8(6), pp.6066-6073.
- 20 Tagliabue, G., Jermyn, A.S., Sundararaman, R., Welch, A.J., DuChene, J.S., Pala, R., Davoyan, A.R., Narang, P. and Atwater, H.A., 2018. Quantifying the role of surface plasmon excitation and hot carrier transport in plasmonic devices. *Nature communications*, 9(1), pp.1-8.
- 21 Sobhani, A., Knight, M.W., Wang, Y., Zheng, B., King, N.S., Brown, L.V., Fang, Z., Nordlander, P. and Halas, N.J., 2013. Narrowband photodetection in the near-infrared with a plasmon-induced hot electron device. *Nature communications*, 4(1), pp.1-6.
- 22 Janotti, A. and Van de Walle, C.G., 2009. Fundamentals of zinc oxide as a semiconductor. *Reports on progress in physics*, 72(12), p.126501.
- 23 Skompska, M. and Zarębska, K., 2014. Electrodeposition of ZnO nanorod arrays on transparent conducting substrates—a review. *Electrochimica Acta*, 127, pp.467-488.
- 24 Chelvayohan, M. and Mee, C.H.B., 1982. Work function measurements on (110),(100) and (111) surfaces of silver. *Journal of Physics C: Solid State Physics*, 15(10), p.2305.
- 25 Özgür, Ü., Alivov, Y.I., Liu, C., Teke, A., Reshchikov, M., Doğan, S., Avrutin, V.C.S.J., Cho, S.J. and Morkoç, A.H., 2005. A comprehensive review of ZnO materials and devices. *Journal of applied physics*, 98(4), p.11.
- 26 Brillson, L.J. and Lu, Y., 2011. ZnO Schottky barriers and Ohmic contacts. *Journal of Applied Physics*, 109(12), p.8.

- 27 White, T.P. and Catchpole, K.R., 2012. Plasmon-enhanced internal photoemission for photovoltaics: theoretical efficiency limits. *Applied Physics Letters*, 101(7), p.073905.
- 28 Aeschlimann, M., Bauer, M., Pawlik, S., Knorren, R., Bouzerar, G. and Bennemann, K.H., 2000. Transport and dynamics of optically excited electrons in metals. *Applied Physics A*, 71(5), pp.485-491.; Bauer, M., Marienfeld, A. and Aeschlimann, M., 2015. Hot electron lifetimes in metals probed by time-resolved two-photon photoemission. *Progress in Surface Science*, 90(3), pp.319-376.
- 29 Groeneveld, R.H., Sprik, R. and Lagendijk, A., 1995. Femtosecond spectroscopy of electron-electron and electron-phonon energy relaxation in Ag and Au. *Physical Review B*, 51(17), p.11433.
- 30 Shepherd, F.D., Yang, A.C. and Taylor, R.W., 1970. A 1 to 2 μm silicon avalanche photodiode. *Proceedings of the IEEE*, 58(7), pp.1160-1162.
- 31 Tan, S., Argondizzo, A., Ren, J., Liu, L., Zhao, J. and Petek, H., 2017. Plasmonic coupling at a metal/semiconductor interface. *Nature Photonics*, 11(12), pp.806-812.
- 32 Scales, C. and Berini, P., 2010. Thin-film Schottky barrier photodetector models. *IEEE Journal of quantum electronics*, 46(5), pp.633-643.
- 33 Furube, A., Du, L., Hara, K., Katoh, R. and Tachiya, M., 2007. Ultrafast plasmon-induced electron transfer from gold nanodots into TiO₂ nanoparticles. *Journal of the American Chemical Society*, 129(48), pp.14852-14853.
- 34 Vahidzadeh, E., Zeng, S., Alam, K.M., Kumar, P., Riddell, S., Chaulagain, N., Gusarov, S., Kobryn, A.E. and Shankar, K., 2021. Harvesting Hot Holes in Plasmon-Coupled Ultrathin Photoanodes for High-Performance Photoelectrochemical Water Splitting. *ACS Applied Materials & Interfaces*, 13(36), pp.42741-42752.

Chapter 2.

Experimental Methods

The work presented here is the result of the combined efforts of many researchers. The techniques used and insights that enabled this research emerged from a consolidated group effort whose goal was the development of a new plasmonic photovoltaic technology. Major portions of this work to which the author contributed significantly are presented in Chapters 3, 4, and 5. Aspects of the work not directly involving the efforts of the author are not described in this thesis. The author contributed materially to a large fraction of the research activities and design decisions that made this work successful, particularly in the area of device fabrication, the development of the nanostenciling technique, electrical characterization, material characterization and data analysis. This Chapter presents details of those techniques and how they were applied to the study of plasmonically enhanced photovoltaics.

2.1. Physical Vapour Deposition

Physical vapour deposition (PVD) broadly refers to thin film growth techniques that use physical mechanisms to grow thin films in a vacuum chamber. This work utilizes two such techniques: thermal evaporation and magnetron sputtering. Both deposition techniques were performed in dedicated instruments purchased specifically for the task. In total, four Kurt J. Lesker PVD 75 vacuum chambers (Figure 2.1) were installed in the SFU 4D LABS class 100 clean room. Two of the instruments were configured with three magnetron sputtering sources driven with RF and DC power supplies. The second pair of instruments were installed with different configurations, the first with 2 thermal evaporation sources and the second with a sputtering source and 2 thermal evaporation sources.



Figure 2.1. The PVD 75 modular deposition instrument.

The systems were all equipped with rotating chucks and quartz lamp substrate heaters capable of heating the steel substrate platen to 450°C. Each chamber was maintained with extreme care to minimize the risk of contamination and maintain tight control of the vacuum environment during deposition. The vacuum system of the PVD 75 comprises a scroll backing pump and turbo pump assembly. The base pressure of each instrument was maintained in the 10^{-8} Torr regime, through consistent overnight chamber bake-outs using the substrate heater at maximum output and cleaning of the chamber shielding. Chamber shielding was cleaned through soaking in tubs of dilute nitric acid solution, gentle mechanical abrasion with cleanroom wipes, extensive rinsing in deionized water, and baking overnight in drying ovens. In addition, special deposition-dependent precautions were taken to maintain chamber conditioning, as outlined in the next two sections.

2.1.1. Thermal Evaporation of Silver

Though many materials can be deposited by thermal evaporation (TE), the technique is most commonly applied to metals. The thermal evaporation of metals is a PVD technique that utilizes heating under vacuum to deposit thin films on a substrate. Metal source material, generally in the form of high purity pellets (99.999%+ pure silver metal pellets purchased from Kurt J. Lesker in this work) are placed in a crucible, which is resistively heated under vacuum. Silver depositions reported here were carried out from alumina coated tungsten wire crucibles shaped into conical baskets (R.D. Mathis). Metal deposition was conducted under high vacuum conditions, below 1×10^{-6} Torr.

Metal evaporation in a vacuum is primarily governed by three important factors: the properties of the material being evaporated, the geometry of the chamber, and the

substrate-metal interactions that govern the nucleation and growth of the film (see Chapter 4 for details of the silver on silicon material combination).

The principal material property of a metal of importance to the TE process is the equilibrium vapour pressure of the source material. The equilibrium vapour pressure is defined as the pressure in a closed container containing a solid or liquid material, at which the rate of atoms evaporating from the condensed phase equals the rate at which gas phase atoms recondense on its surface. A material's vapour pressure increases with temperature and a value of 10^{-2} Torr is widely accepted as the threshold above which the rate of evaporation in the TE process becomes practical for the fabrication of thin films ¹ (Figure 2.2).

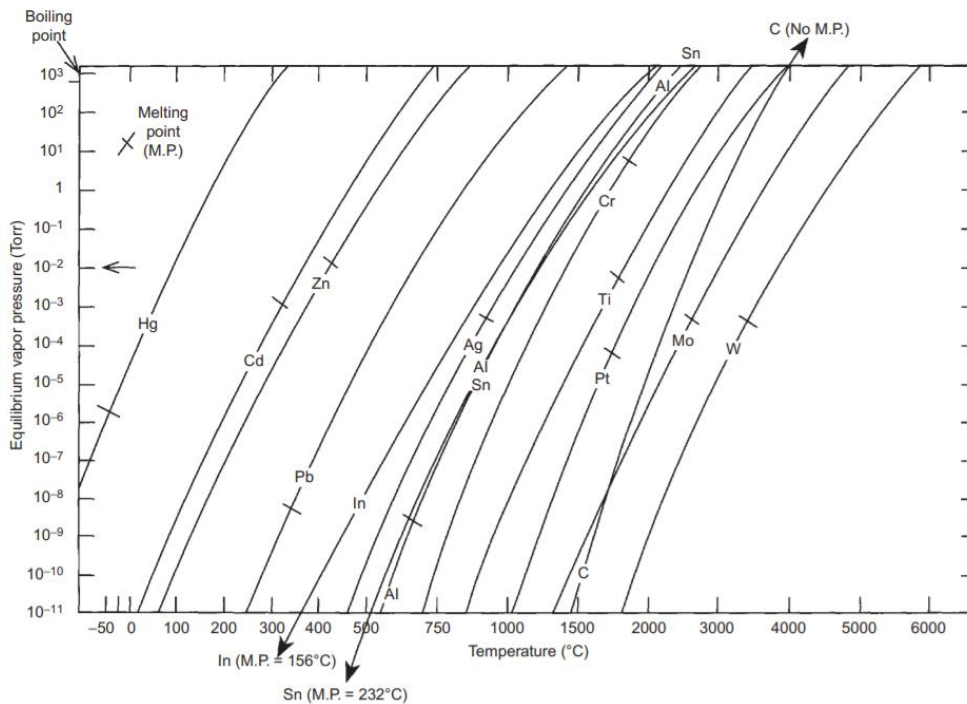


Figure 2.2. Equilibrium vapour pressure for a selection of metals (reprinted with permission from reference 1)

The geometry of the vacuum vessel and the relative orientation of the sample and source are also important to experimental design. Because metal atoms that are evaporated leave the hot surface with an energy given by $3/2kT$, where k is the Boltzmann constant and T is the absolute temperature in Kelvin, they propagate at speeds of ~ 1 km/sec and possess on the order 0.1-0.2 eV of kinetic energy at relevant

temperatures. In high vacuum environments atoms can have mean free paths on the order of 1 metre and travel from source to substrate in virtually a straight line. Because the number of atoms colliding with the substrate depends on its radial distance to the source with a $1/r^2$ dependence, the thickness of a deposited film on a flat substrate varies over the surface of the film depending on the angle to the source (Figure 2.3). More complete descriptions of the radial thickness of TE deposited films also account for the angle dependent rate of evaporation from the source if the vapour pressure of evaporated atoms in the near surface region is accounted for. As metal atoms leave the surface, their path length through this higher density surface layer depends on position and their angle of propagation relative to the surface normal. This suppresses off normal deposition rates due to increased metal-metal scattering collisions in these directions.²

These geometric considerations generate a trade-off in the selection of substrate-source positioning to maximize the deposition rate while minimizing radial thickness variations. For the devices presented here, a 60cm throw distance was utilized and surface thickness variation across a 4 inch sample holder diameter was found to be less than 10% when the 6MHz quartz crystal thickness monitor (QCM) was calibrated to the center of the substrate.

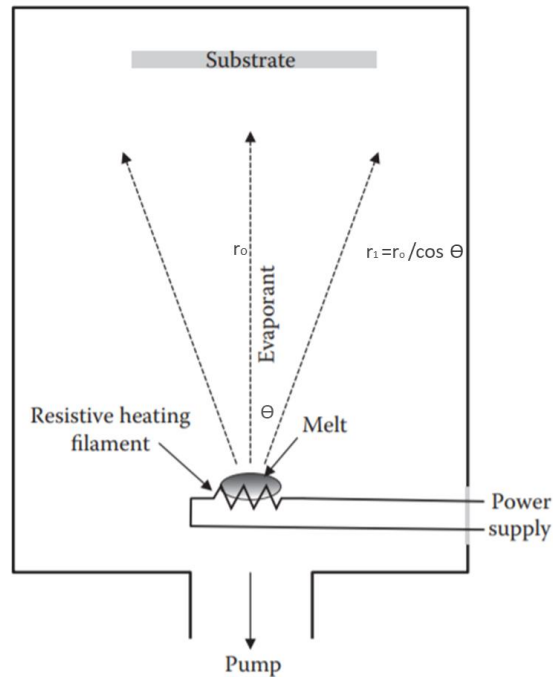


Figure 2.3. Angle dependent thickness of Thermal evaporation. (adapted with permission from reference 7)

Two principle TE methods were developed over the course of this research. The first was a low temperature technique utilized in top contact deposition for prism devices and nanostencil-based nanostructuring. This procedure consisted of inserting samples clamped to a 4-inch platen into the vacuum chamber immediately after venting the chamber. Fresh silver pellets of “5-nines” purity were inserted into the heater basket and the chamber was pumped down to 5×10^{-6} Torr before being preheated to 80°C for one hour. After one hour the chamber was allowed to cool to 55°C . The silver evaporation began upon achieving a chamber pressure of less than 1×10^{-6} Torr or the cooling reached the 55°C target temperature. In almost all cases the chamber pressure was well into the 10^{-7} Torr range before the cooling was complete. The source was heated resistively and upon the onset of evaporation the rate was allowed to stabilize and 20 nm of silver was pre-evaporated prior to the opening of the substrate shutter (better results were achieved when the source shutter was removed). The deposition was conducted at a QCM monitored rate of $0.7\text{\AA}/\text{s}$ or to thickness of variously 50, 100 or 150 nm without sample rotation.

The difference between the low temperature deposition step for the prism samples in Chapter 3 and the nanostructuring deposition of samples presented in Chapters 4 and 5 are in the pre-deposition preparation steps (Section 2.3).

The high temperature TE of silver method included a thorough precleaning of the silicon substrate prior to deposition. The cleaning steps consisted of two 15min soaks sequentially in very large-scale integration (VLSI) grade acetone (ACE) and VLSI isopropyl alcohol (IPA). This was followed by 3 spray-immersions for 1 minute in deionized (DI) water. The samples were dried under a stream of ultra pure (99.999+%) nitrogen before undergoing the RCA cleaning process³. All wafers were prime grade 1-10 ohm p-type (100) oriented and purchased from a variety of vendors. It was found that for some batches of silicon wafers the RCA cleaning step could be omitted, but for others, the RCA step was necessary to achieve the desired film quality. The last step in the cleaning process was a 1-minute immersion of the wafer in a buffered oxide etch (BOE) solution of hydrofluoric acid and ammonium fluoride in deionized water (various vendors). The etch step removes the native oxide layer from the silicon wafer surface and is a critical factor in the quality of the silver films (Chapter 4). The etched silicon wafer is rinsed with DI water and blown dry with a jet of N₂ before being immediately transferred to the PVD chamber. This step was generally performed within 10 minutes of the BOE step in order to minimize the regrowth of the native oxide layer in air or during rinsing with DI water. The chamber was prepared with fresh Ag pellets prior to sample insertion, with special attention to timing the chamber vent to prevent excessive adsorption of atmospheric water to the chamber walls. The system was then evacuated to a pressure of $<5 \times 10^{-6}$ Torr before the gradual heating of the substrate to 350°C at a rate of 10°C/min. Upon reaching the set temperature, the sample was baked for 1 hour or longer, until the chamber pressure reached $<5 \times 10^{-7}$ Torr. The target pressure was almost always achieved within the hour heating step. The source was heated gradually, and the evaporation rate was allowed to stabilize, with a further 50 nm of silver evaporated prior to opening the substrate shutter. The source shutters were not used in these experiments. Deposition of silver was then conducted at a rate of 3 Å/s to a thickness of 300 nm without substrate rotation. The 300 nm target film thickness was required to achieve the coalescence of the growing film (Chapter 4).

2.1.2. Magnetron Sputtering of Zinc Oxide

Sputtering is a widely used thin film deposition technique. Popularized in the 1970's, today sputtering processes are ubiquitous in commercial microfabrication. There are many variants of sputtering instruments, such as DC, RF, and reactive, which are used to deposit metals, dielectric insulators, and semiconductors.

The basic design of a sputtering system can be understood as two electrodes separated by a space filled with low pressure gas (Figure 2.4). The cathode is replaced by a target composed of the material to be deposited in a film on the substrate, which is placed near the anode. Positively charged ions impacting the cathode eject neutral target atoms which travel through the inter-electrode space and deposit on the substrate. In this work 99.99+ pure ZnO, and 2%Al:ZnO 3" targets purchased from Kurt J. Lesker were used for zinc oxide and doped zinc oxide film deposition respectively.

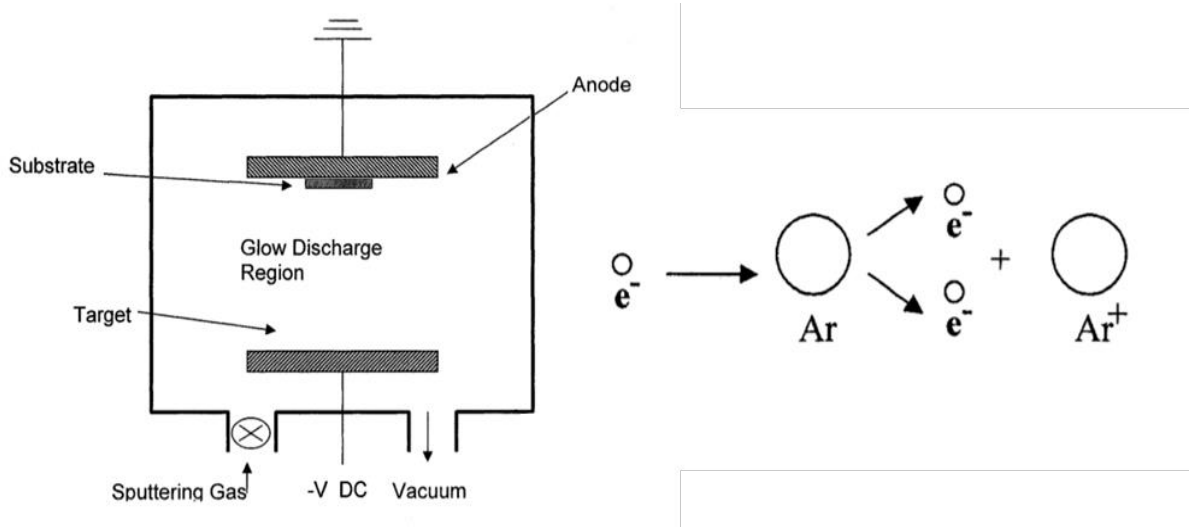


Figure 2.4. a) Schematic of a simplified DC sputtering system (adapted with permission from reference 7) b) The ionization cascade for argon gas.

A mechanistic description of the sputtering process is complex,^{4,5} but, for the purposes of the present case, can be described to an acceptable level with relative brevity. When DC voltage is applied to the cathode in a system like the one shown schematically in Figure 2.4, stray electrons are accelerated towards the anode by the resulting electric field. If the voltage and pressure are of an appropriate value, the

electron gains enough kinetic energy to ionize a neutral gas atom, generating a second electron and a cation. The two electrons are both accelerated towards the anode and in turn generate more electrons and cations. This process causes a cascade of ionization that generates the plasma. At the same time the generated cations (argon ions in the above Figure) are accelerated towards the cathode. The impact of the massive positive ions on the cathode liberates more electrons (secondary electrons), which then join in the cascade of ion generation. When the number of electrons generated by collisions within the gas and by impact of cations on the cathode equals the number of electrons neutralized by de-excitation and by impact on the anode the plasma is in equilibrium and becomes self-sustaining at a given applied voltage.

Above a kinetic energy threshold, determined by the binding energy of the target atoms, the mass ratio of the cations to the mass of the target atoms, and a number of other factors⁶, cations impacting the target surface will impart sufficient energy to the target surface to eject a neutral atom. Ejected atoms propagate through the vacuum chamber ballistically, undergoing collisions with atoms in the gas phase until they collide with the substrate, forming a growing film. Scattering in the gas phase increases the angular distribution of sputtered atoms, so they can cover the substrate surface conformally. This is in contrast to thermal evaporation where the evaporated metal atoms are likely pass through the vacuum collision-free, and regions without direct line of sight to the source have much thinner coverage. Because of the large number of cation-surface interactions possible for cations that are commonly accelerated to energies 100s of eVs, sputtered atoms possess a continuum of energies around a peak value, often in the range of 10eV. The high energies of the sputtered atoms are a key feature of the sputtering technique that differentiates it from TE where the energies are in the range 0.1 to 0.2 eV¹. Energetic sputtered atoms are advantageous for forming dense continuous films with good surface coverage at low thickness, but due to the high energy of the sputtered atoms, can also lead to damage to the substrate and excessive heating⁷.

Magnetron sputtering instruments employ a modified cathode in order to increase sputtering deposition rates relative to those for simple DC instruments. Currents in magnetron sputtering instruments are one or two orders of magnitude higher, and plasma gas pressures are much lower than for their non-magnetron counterparts. This effect is achieved through the placement of small permanent magnets behind the target

in a "racetrack" type configuration (Figure 2.5). The intense magnetic field generated above the target surface is parallel to the field at the edges, and perpendicular to the electric field above the centre of the track. Electrons are confined inside the magnetic field because electrons emanating from the target are directed towards the centre of the track by the magnetic field normal the target surface, and the perpendicular magnetic and electric fields in the centre region of the track confine the electrons, causing them to be directed in a cycloidal fashion along the axis of the field lines. This has the result of lowering the electron mean free path component in the direction normal to the target. More electron collisions in the near-surface region generate cations that can more efficiently sputter the target, rather than lose energy through non-ionizing collisions in the greater bulk of inter-electrode volume. The greater ion density also allows the generation of stable plasmas at much lower pressures ($1-10 \times 10^{-3}$ Torr) than for simple DC systems ($1-5 \times 10^{-1}$ Torr).

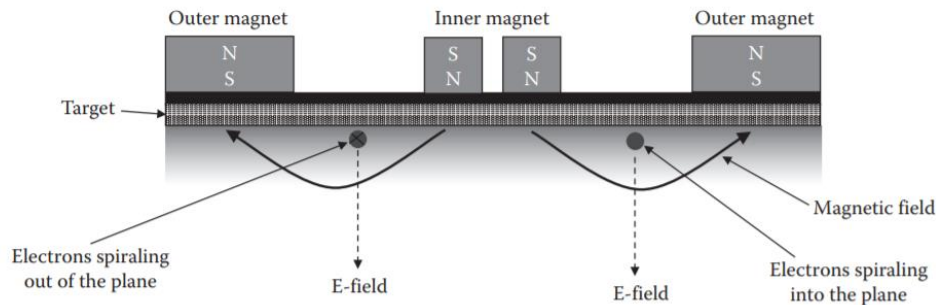


Figure 2.5. Cross section of a circular sputtering target in a magnetron configuration. (reprinted with permission from reference x)

Radio frequency (RF) sputtering is a technique used for non conducting targets like zinc oxide. A radio frequency generator (often at 13.56 MHz) is used to generate oscillating currents within the plasma by placing a copper backing plate on the nonconductive target. The resultant capacitive circuit supports the motion of electrons and cations. The electrons have much lower momentum than the cations and move much more quickly towards the target during the positive part of the RF cycle, giving it an average negative DC bias. This bias contributes to the field driving the cation bombardment, extending the length of the cycle where cations bombard the surface between short periods of the RF oscillation, where fast moving electrons return to the

target⁶. RF sputtering was used for the deposition of the semiconducting zinc oxide films studied in this research.

Optimizing the deposition conditions of the zinc oxide film device layers for high efficiency plasmonic photovoltaics was an empirical process that required hundreds of recipe iterations and some physical modifications of the PVD systems. The complexity of the electronic and material properties of zinc oxide is well known⁸ and the limitations of the PVD equipment available imposed some constraints on the study. It was found that in order sputter films that allowed good Schottky barrier formation, and the highest efficiency PV response, the deposition chamber needed to be maintained in pristine condition. All easily accessible parts, including target retention rings, chamber shielding, substrate gas diffusion rings, and substrate and target shutters were consistently swapped and cleaned according to the same schedule outlined in section 2.1.1. The chamber was regularly baked out with a custom designed quartz lamp assembly that was placed within the chamber to complement the quartz substrate heater, the positioning of which did not allow uniform heating of the chamber. The combination of the two heaters was found to enhance bake-out performance, helping to eliminate adsorbed water from the shielding walls. The sputter gas delivery equipment was also upgraded to include a high purity regulator, eliminating contamination of the 99.999% argon gas and ultra pure 5% O₂:Ar gas mixtures during tank changes. The 5% O₂:Ar mixture was a necessary component of the setup because it was found that a tightly controlled low concentration of reactive oxygen in the plasma stream was required to achieve good quality Schottky contacts. At these low concentrations the PVD 75's mass flow controller was too inaccurate to ensure repeatable film quality, so a prediluted mixture was required. Tight, reproducible control of the plasma gas mixture was the motivation for the extreme care and effort devoted to chamber cleaning and gas purity.

Best results were achieved for zinc oxide deposited on TiO₂ prisms (Chapter 3), according to the following process steps. A clean, dry, single-crystal TiO₂ right angle prism, with a c-axis cut normal to its hypotenuse, was positioned on a custom machined PVD chamber sample platen. The prism was previously coated with a 100 nm thick film of conducting, 2% Al doped ZnO (Section 2.1.3). The platen was machined with slots that could accept prism samples in such a way that the hypotenuse was level with the platen surface, and the remainder of the prism protruded above the downward facing platen. The platen was inserted into the vacuum chamber and the system was pumped

down to a base pressure $<2 \times 10^{-6}$ Torr, before gas line purging. Sputter gas lines were purged by allowing gas to flow at 100 sccm in the Ar and Ar:O₂ lines for 10 minutes under 80% turbo pump power. Then the system was pumped down with no gas flow below the base pressure. The purge step was run 3 times. After that, the substrate heater was set to the deposition temperature (300-400°C) and the sample pre-baked for 2.5 hours. Subsequent to baking, the ZnO target was pre-sputtered for 30 mins at a power of 80W and a pressure of 10 mTorr with a 200:1 argon to oxygen ratio in the sputter gas supply. After pre-sputtering, the pressure was lowered to 2 mTorr and the source and substrate shutters were opened. Sputtering was conducted for 1230 seconds (12.3 second/nm) with the platen rotation active. Upon completion of the sputtering step the chamber was pumped down and the sample was allowed to cool to $<80^\circ\text{C}$ before removal of the sample.

The best results achieved for ZnO films deposited on nanostructured silver substrates (Chapters 4 and 5) were achieved by transferring freshly deposited silver on silicon substrates directly into the sputtering vacuum chamber and immediately pumping the chamber to a base pressure $<2 \times 10^{-6}$ Torr. The pump and purge cycles described for prism ZnO films were repeated. Because the silver substrate is easily oxidized in plasma, the pre-sputtering step was conducted before venting the chamber to insert the sample. The sample was heated to 100°C for 30 minutes under vacuum before the deposition was started with a 200:0.7 argon to oxygen sputter gas ratio at a pressure of 3.5 mTorr and a power of 50W. The deposition lasted 4500s at a rate of 30s/nm.

2.1.3. Magnetron Sputtering of Doped Zinc Oxide

Doped zinc oxide is a material of intense interest to the electronics industry because of its good optical transparency and reasonably high conductivity⁹. Doped ZnO (dZnO) can be sputtered from a ceramic composite target composed of ZnO and 2% Al₂O₃. Though dZnO targets are not themselves conducting, the sputtered films that result from RF magnetron sputtering of the mixed ceramic materials are. Low resistivity dZnO films were achieved under high and low temperature deposition conditions.

“High temperature” dZnO was deposited as the bottom contact for prism-coupled devices (Chapter 3). TiO₂ prism samples were loaded in a custom machined, slotted platen holder, the platen was placed in a PEIIA oxygen plasma cleaner and subjected to

a 60s plasma clean at 50W under 10mTorr of oxygen pressure. The platen was immediately inserted into the PVD chamber, and the system was pumped down. The 3-cycle pump and purge step was conducted (see 2.1.2) and then the substrate heater was set to 400°C for 4 hours. Prior to beginning the deposition, the target was pre-sputtered for 30 minutes at 100W with the target and substrate shutters closed. The deposition was conducted at a pressure of 2 mTorr under 100% argon gas flow for 3660 seconds to a thickness of 100 nm (36.6 seconds/nm) with platen rotation active. The sample was allowed to cool under high vacuum conditions to 80°C before venting.

“Low temperature” dZnO films were deposited as the shadow masked top contacts for the silver bottom contact nanostructured samples (Chapters 4 and 5). The deposition was shadow masked by clamping a nickel mask perforated with 250 μm holes to the platen, in contact with the surface of the sample. The sample was loaded into the chamber and the pump and purge method was conducted as described above. The substrate heater was set to 100°C for 1 hour. After a 30-minute pre-sputter step with the substrate and target shutters closed, the samples were deposited for 5300s to a thickness of 150 nm (35.2 seconds/nm) with no platen rotation. The chamber was allowed to cool under vacuum to below 80°C prior to venting.

2.2. Nanostructuring techniques

The nanostructuring of surfaces, often termed nanolithography, is the practice of generating surface features or surface patterns on the nanometer scale. Traditionally, nanolithography was considered to be patterning at dimensions below the diffraction limit of traditional “i-line” 365 nm UV lithography¹⁰, but this definition is increasingly antiquated with the advent of 13.7 nm extreme UV lithography and its nanometer-range critical dimension capabilities. Nevertheless, the expense of such technologies puts them out of consideration for research purposes or large-area, high-throughput applications such as optical metamaterials¹¹, superhydrophobic surfaces¹², high surface area hetero-catalytic devices, and advanced battery and fuel cell electrodes¹³.

The techniques presented here were developed initially as part of the group research project, which enabled the vast majority of the devices described in this work. However, they were later refined and re-imagined as “rapid electron area masking”

(REAM) lithography, which is the subject of the recently issued patent included as appendix A of this thesis. It is also briefly summarized at the end of this Section.

Both REAM and the nanostenciling technique utilized to build the free space-coupled plasmonic PV devices described in Chapters 4 and 5 leverage the use of nanostencils¹⁴. Nanostencils can be fabricated through custom microfabrication or purchased from vendors. The standard nanostencils used for the majority of this work were purchased from Aquamarijn Micro Filtration BV.

The nanostencils that enabled the high throughput device design presented in Chapters 4 and 5 utilize a stress-free silicon nitride (SiN) membrane that has been patterned with 450 nm holes arranged in a hexagonal array with a 900 nm period (Figure 2.6). The SiN membrane, which is approximately 500 nm thick, is supported by a silicon scaffold backing fabricated from a 450 micron silicon substrate. The scaffold supports a 150 μm span laterally, and 3 mm trench vertically. Each nanostencil supports 14 trenches (Figure 2.6c)

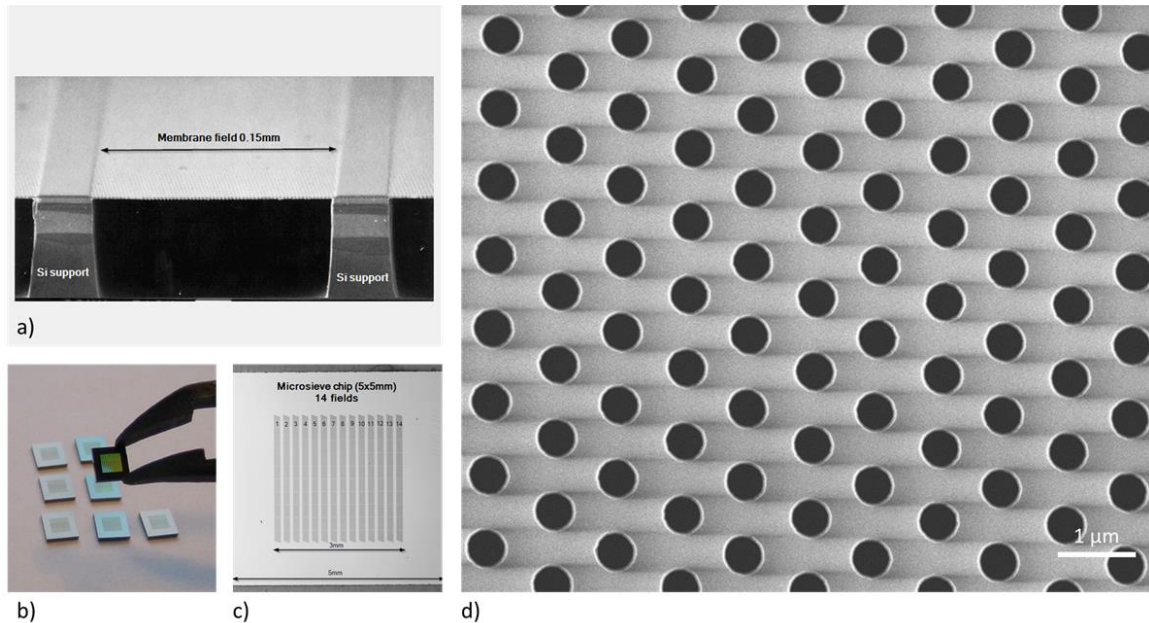


Figure 2.6. Nanostencil images. a) cross-section of the membrane and scaffold. b) Transparent, iridescence of the thin stress-free SiN. c) Trench geometry. d) SEM image of the nano-hole array.

Nanostenciling is a simple and effective technique for additive fabrication of nanostructured surfaces. The quality of the deposited features is greatly increased if the nature of the substrate and the substrate-surface interactions are selected to template the growth of the nanomasked layer (see Chapter 4). This “bottom-up” refinement of the nanostenciling technique sets this work apart from other research, where nanostenciling leads to features with poor crystallinity and irregular shapes^{15,16,17}.

The nanostenciling process used for device fabrication consisted of clamping a nanostencil to the top surface of the silver substrate (2.1.1) on a PVD platen. The process was simplified by the fact that the nanostencil was the same thickness as a standard 4 inch silicon wafer and could easily be supported around the edges by sacrificial silicon wafer chips. The additive nanostructuring deposition was conducted according to the process outlined in 2.1.1 for low temperature silver deposition.

Nanostencils were robust to reuse and, with care, could be reclaimed through soaking in 10% nitric acid solution until the silver deposited on the top surface of the stencil was dissolved. After copious rinsing in DI water, the individual stencils were placed in the barrels of cut disposable glass pipette tips to protect the sensitive front surface and dried in an oven at 120°C before re-use. Stencils were robust to dozens of uses if handled carefully.

Along with enabling low cost, high throughput, nanopatterning of silver pillars, the nanostencil technique afforded the benefit of minimizing the surface contamination of the underlying silver films. Traditional nanolithography using electron beam resists or other techniques such as colloidal bead lithography²⁵ carry the added complexity of interface contamination and interface cleaning steps. Nanostencilling, since it is a direct patterning technique, maintains good interface quality with no cleaning steps required when the process is done with extreme care towards nanostencil pre-cleaning.

The utility of nanostencils for subtractive nanopatterning was also investigated and this led to the invention of a novel nanolithography process termed rapid electron area masking, REAM, lithography. Briefly, it was found that a gold/SiN composite membrane could block electron beams to a voltage of 15keV and generate sufficient contrast to expose polymethylmethacrylate (PMMA) electron beam resist, generating features as small as 50 nm over a 3000 μm^2 area in under 10 seconds, under the instrumental

constraints outlined in Appendix A. This proximity contact, wide area, rapid technique holds promise for application to broad areas of metamaterial development, such as large scale inexpensive flat optics¹¹, and architectural glass with passive optical properties that reduce heating and cooling costs.

2.3. Material Characterization Techniques

The silver, zinc oxide and doped zinc oxide films that comprise the devices described in the next three chapters were characterized with a suite of material characterization techniques. The basic operating principles of these techniques and details of how they were applied are presented in the following subsections.

2.3.1. Scanning Electron Microscopy

Scanning electron microscopy (SEM) uses a focused electron beam that is raster-scanned by means of dynamic magnetic and electrostatic electron optics across the surface of a sample. The beam interacts with the sample at a focused point and signals, in the form of backscattered electrons, secondary electrons, and x-rays are collected. The signal from the rastered area is composed into an image that represents the combined signal collected from the points scanned. Figure 2.7 depicts the major components of a SEM instrument. The advanced technical details of SEM instrumentation and procedures are well-treated elsewhere,¹⁸ but some details are presented below to inform the reader's thinking about the sample images and the REAM process (appendix A).

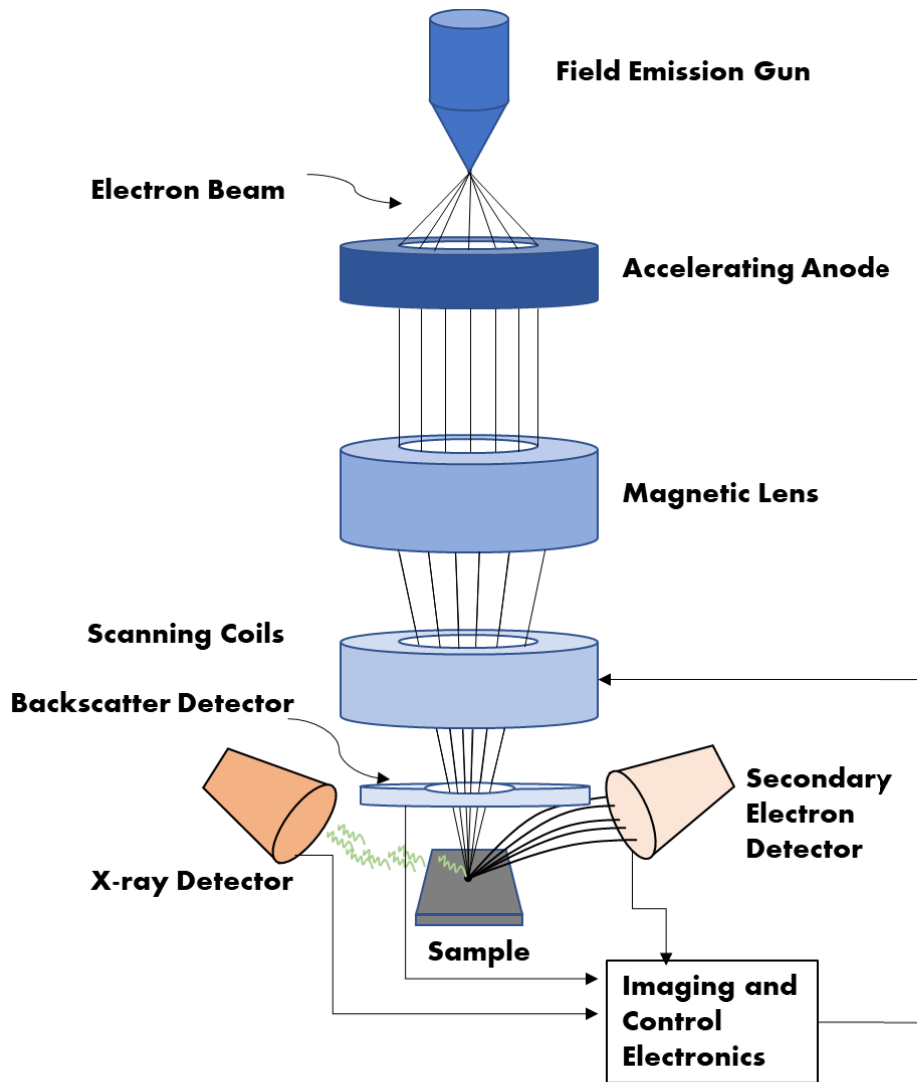


Figure 2.7. Basic elements of a scanning electron microscope.

SEM is a versatile, and rapid technique that enables visual analysis of nanoscopic surface features and film morphology, as well as elemental analysis through spectroscopic analysis of X-ray emissions from the sample under electron bombardment. Major variables that govern image quality and the type of information that can be acquired from SEM are beam energy and detector type.

Typically, electron beam energies are between 5 and 30 keV and are developed by the anode beam accelerator assembly. Modern instruments with precision field emission gun electron sources and refined magnetic focusing optics can generate spot

sizes in the 100s of picometre range. High quality detectors with low noise and sensitivity can resolve signals into high resolution images at sub pA beam currents.

Two commonly encountered electron detector types were used for imaging in these studies, a backscatter detector that measures backscattered electrons (BSEs), and a secondary electron detector that measures the signal from secondary electrons (SEs). BSEs are defined by convention, as electrons scattered from the sample surface with energies ranging from 50eV to the energy of the primary electron (PE) beam (Figure 2.8). The BSE detector measures primary electrons that scatter within near surface of the sample, at depths of 10 nm to 10 μm , depending on the density and composition of the sample and the PE beam energy. Backscattered electrons lose energy to collisions within the sample before re-emitting into the sample chamber. BSE detectors are usually in the form of an annular ring around the PE beam path.

Secondary electrons are generated through PE collisions with valence and near valence level electrons with energies near the Fermi energy of the sample. If these electrons are near the surface of the sample, PE collisions can raise their energy such that they are emitted from the surface. Secondary electrons, in the most common Everhart-Thornley configuration¹⁸, are first attracted to a collection grid charged to +100-200V, before being collected by a combination of a scintillator and photomultiplier tube.

SEM was used extensively in this work to characterize surface quality, while bulk morphology of deposited films, and film interfaces between device layers were investigated by cross sectional imaging. Imaging work was done on a FEI Nova NanoSEM 430, FEI Strata DualBeam (SEM/FIB) 235, or FEI Helios NanoLab 650 scanning electron microscope. Thousands of images were collected and analyzed in the iterative effort to optimize device properties. A survey of the myriad of micrographs collected are presented in Figure 2.7

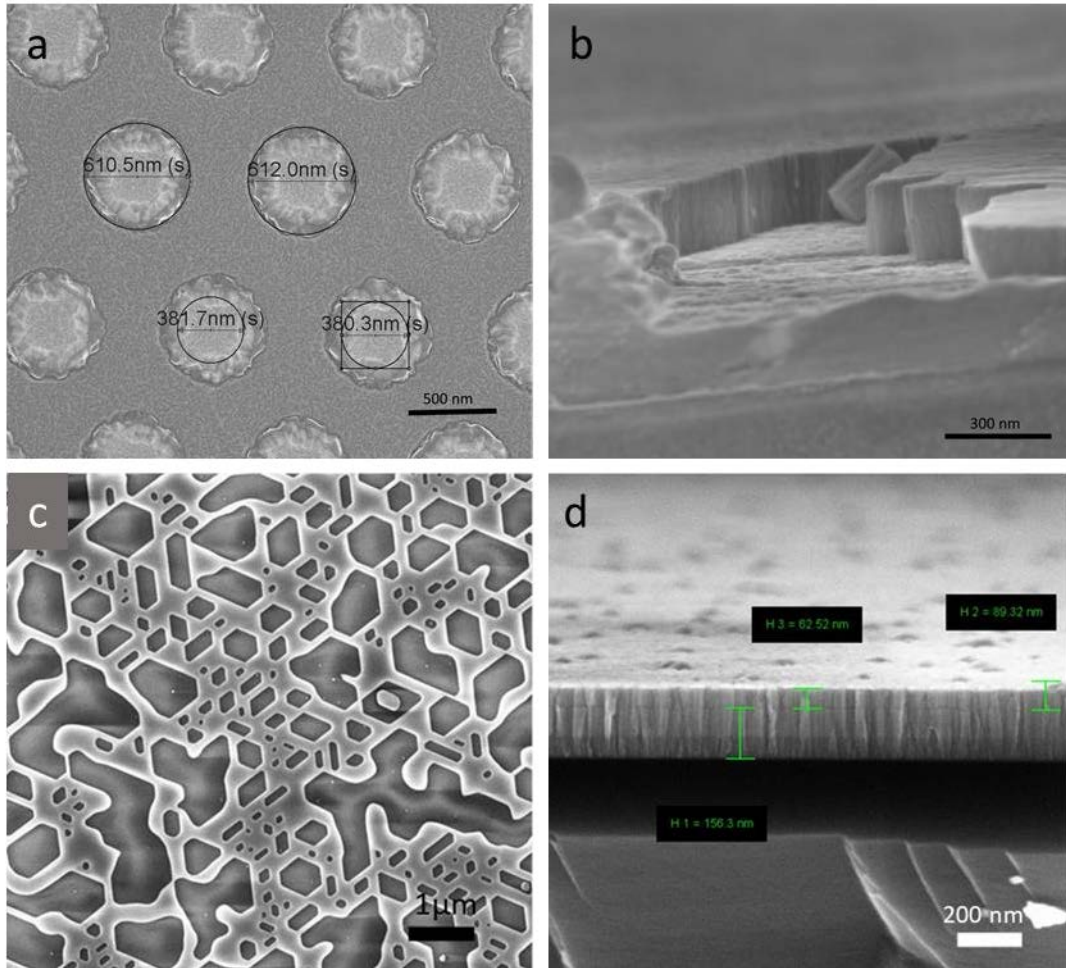


Figure 2.8. Examples of SEM images. a) Top surface of samples presented in Chapter 5, b) cross section of the ZnO, dZnO interface, c) discontinuous growth of silver on a mica substrate, d) cross section of experimental three layer deposition of dZnO/ZnO/ZnO on Si(100).

2.3.2. Focused Ion Beam Milling and Transmission Electron Microscopy

The major components of a transmission electron microscopy – focused ion beam instrument are depicted in Figure 2.9. In contrast to SEM, TEM uses higher energy primary beams, 200 keV in the case of the instrument used in this research, to probe the crystal structure of very thin samples. The diffraction of the high energy PE beam as it passes through the lattice generates a diffraction pattern that is captured on a fluorescent screen at the end of the TEM beam path. The fluorescent light is then captured by a high-resolution camera and converted into a digital image¹⁹. Because the

wavelength of high energy electrons is so small, the diffraction limit of the PE beam is on the order of the atomic dimensions of the material being imaged. Sensitive instruments can magnify the diffracted electron signal to project images onto the fluorescent detector screen with high enough resolution to image the atomic lattice of the sample.

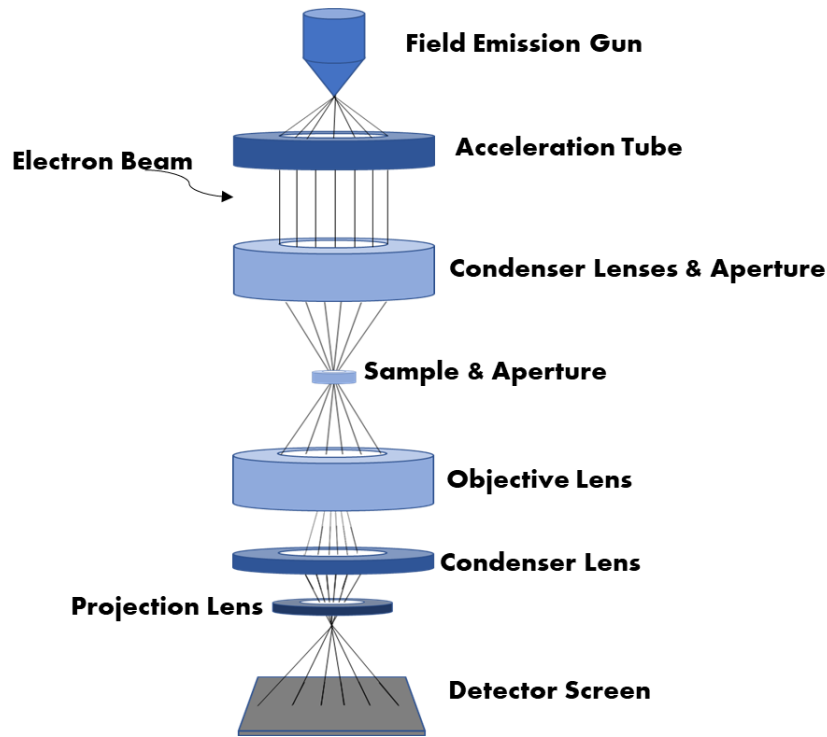


Figure 2.9. Simplified schematic of a transmission electron microscopy instrument.

Sample preparation is a major challenge for TEM. In order to achieve the highest resolution imaging and reasonable image contrast, the thickness of samples must lie below the depth of focus of the electron lens, usually in the range of 100 nm or less. For the TEM imaging presented in Chapter 4, and below in Figure 2.10, samples were prepared as free-standing vertical slabs. The slabs of the sample were prepared by a focused ion beam (FIB) “lift-out” technique. Lift-out was conducted in the FEI Helios NanoLab 650 SEM instrument. The technique uses a beam of gallium ions that are field emitted from an electrostatically charged tungsten needle coated in the liquid metal. The gallium ion beam kinetic energy is high enough to sputter atoms from the surface of the sample. The beam is precisely controlled to “mill out” a trench into the sample surface

and liberate a sliver of the sample that comprises a representative profile of the depth morphology (see inset of Figure 2.10). The sliver can then be transferred to a TEM sample holder by first attaching the sample to a transfer needle tip using amorphous platinum deposited from gas assisted selective deposition GASD²¹. The sample is transferred to the TEM sample holder and further thinned by a series of milling and GASD steps, removed from the SEM chamber and imaged in the transmission electron microscope.

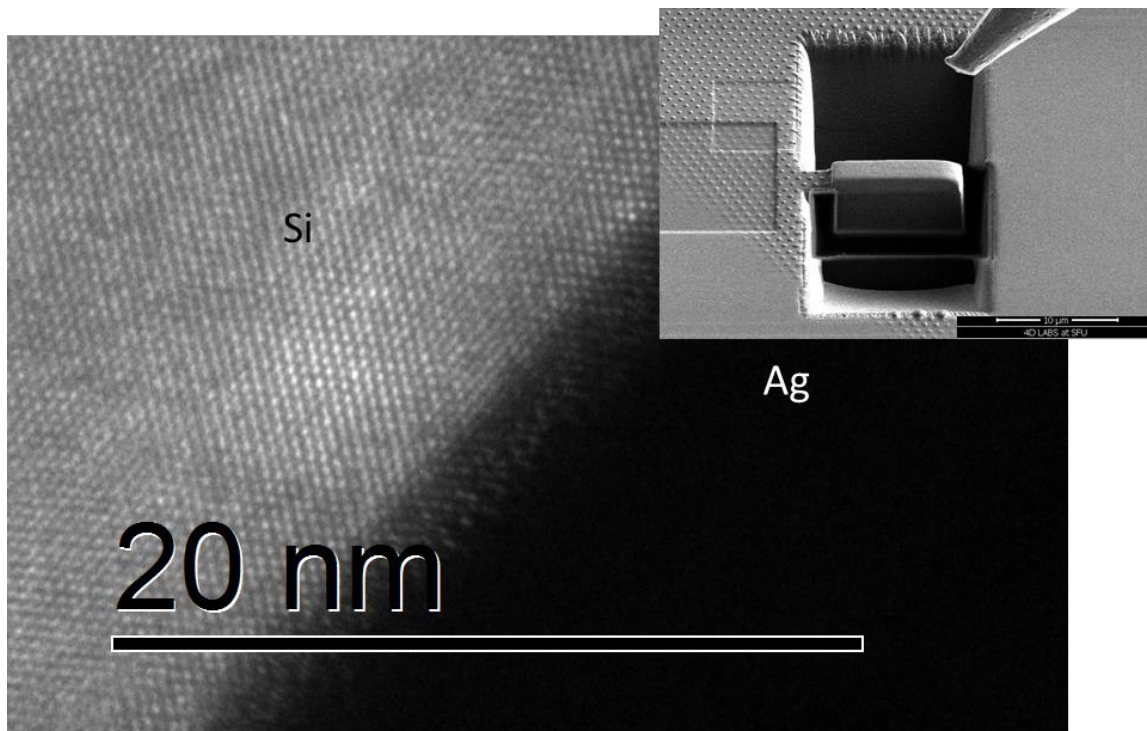


Figure 2.10. High resolution TEM cross section of the Ag-Si interface (inset the focused ion beam prepared sample being lifted out).

2.3.3. Two-Dimensional X-Ray Diffraction

X-Ray Diffraction is a non-destructive technique that uses X-rays to measure the lattice parameters and crystallinity of materials. The X-Rays, in the case of the instrument used in this work, are generated by a sealed tube source. This source uses cathode ray tube-generated, high energy electrons to ionize copper, emitting electrons from the 1s deep lying orbital. The resultant K_{α} transitions of copper atoms from the deep lying 2p to 1s orbitals emit x-ray photons with wavelengths, λ , near 1.54 Å. These

photons are collimated and directed at a sample, where their diffraction from atomic crystal lattice planes with spacing, d , is given by Bragg's law:

$$n\lambda = 2d\sin(\theta) \quad (2.1)$$

where n is the diffraction order, and d is the lattice spacing. By changing the angle of incidence of the X-rays, the angles of incidence that satisfy the Bragg condition are diffracted at an angle 2θ relative to the propagating beam (Figure 2.11). Through angle scanning, diffraction from the different lattice spacings that define a crystal's unit cell can be collected by a detector and lookup tables allow the identification of materials from characteristic 2θ separations²⁰.

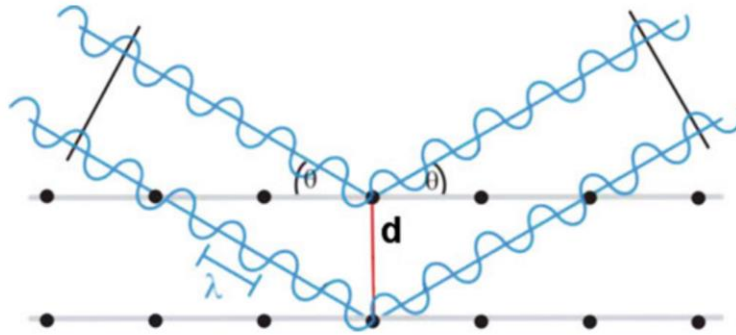


Figure 2.11. Graphical representation of diffraction according to Bragg's law.

The Bragg Equation is derived from the assumption that the x-rays are diffracting from an infinite lattice. If a material is composed of smaller crystallites, the observed diffraction angle is broadened from the ideal single peak. The effect of crystallite size on the full width half maximum, FWHM, of the diffraction angle peak was quantified by Scherrer and is expressed by:

$$L = \frac{K\lambda}{(FWHM)\cos(\theta)} \quad (2.2)$$

where L is the mean crystallite size and K is the Scherrer constant, which is a shape factor with a value close to one. By examining the peak widths of XRD peaks it is possible to calculate values for crystallite size, but often instrumental and sample geometry factors make the calculation inaccurate. For similar samples on the same

instrument however, it is possible to make relative judgements of crystallite size (see Chapter 3).

Two-dimensional (2D) XRD is an extension of the technique which not only measures 2θ angles but, with the instrumentation under discussion, uses an area detector to measure x-rays diffracted in off axis arcs called Debye rings²⁰. Debye rings result when samples are composed of crystallites that are not all oriented in the same way. Diffraction from grains with different orientations results in different 2D diffraction patterns. A polycrystalline sample with randomly oriented grains will give rise to a diffraction spectrum that looks like a ring, with a diameter of 2θ and a 360° sweep of the Debye cone signal. If the grains are partially aligned, instead of a ring, an arc with angular sweep angle of X is detected. A single-crystal sample will have a small instrument limited angle X that appears as a diffraction spot (Figure 2.12). The 2D XRD pattern in Chapter 4, reproduced in part here, highlight how the technique informed device design and process optimization.

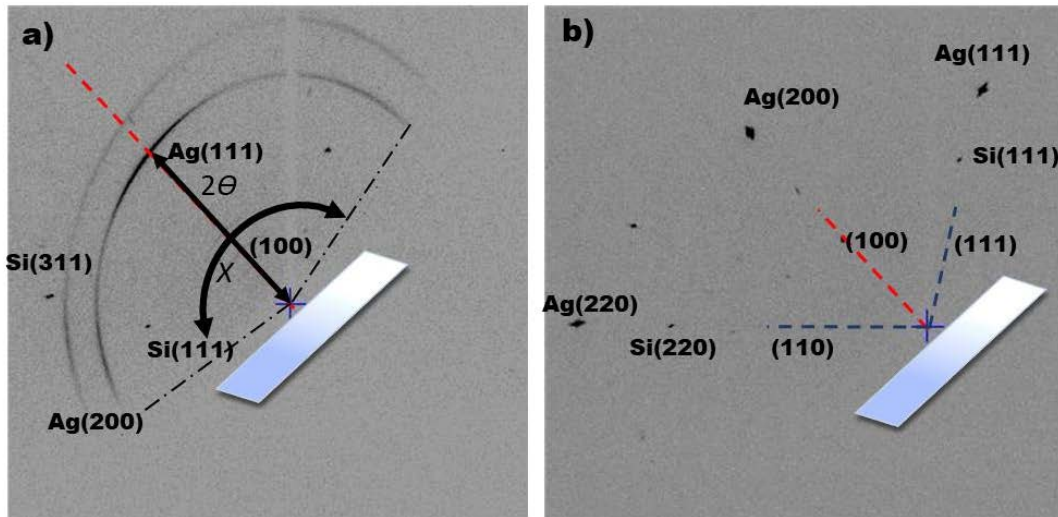


Figure 2.12. 2D X-Ray diffraction spectra. a) Polycrystalline silver with ring angle X and 2θ angular distance from the point of origin. b) Single-crystal silver results in point diffraction spots. The dashed red line is the orientation normal to the surface.

All 2D XRD patterns reported in this work were acquired with a Rigaku Rapid Axis X-Ray Diffractometer utilizing a Cu source operated at 46 kV power, 42 mA current, and a 0.3 mm collimator for the Cu radiation ($K\alpha = 1.5406 \text{ \AA}$).

2.4. Electrical Characterization Techniques

Electrical characterization of the devices and films developed over the course of this project was critical to the high throughput iterative approach to optimizing the fabrication process. The success of this approach is evident in the observed improvements over time in device performance (see Section 2.5). Outside the cleanroom, a Keithley 2400 source meter with serial interface was used to characterize devices. Inside the cleanroom, a Cascade Microtech MPS150 probe station and Agilent Technologies B1500A semiconductor device analyzer (Figure 2.13) was utilized. In all systems, tungsten needle probes were used to make low contact resistance contact with the samples. Electrical measurements were principally conducted to measure the current-voltage characteristics of fabricated Schottky junctions (see Section 1.3).

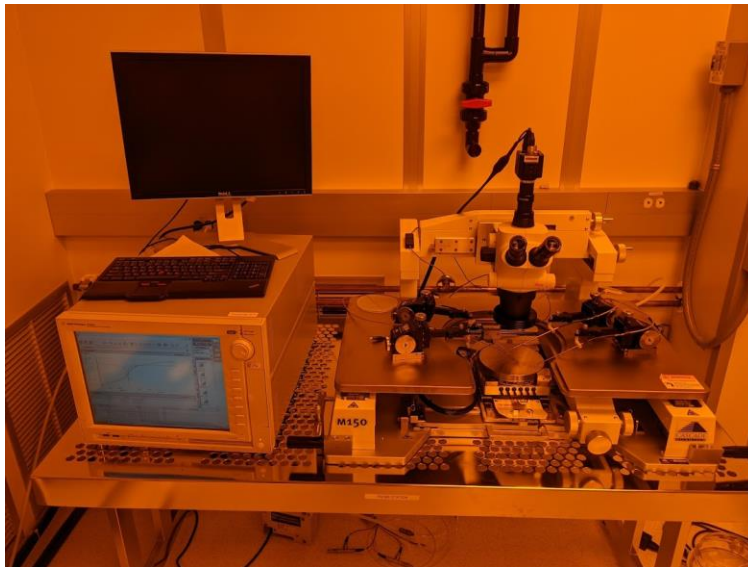


Figure 2.13. The M150 probe station. Samples were placed under the microscope on the circular vacuum sample stage and probed with tungsten needles attached to manually operated probe manipulators. Experiments were conducted under the control of the Agilent 1500A analyzer.

2.4.1. Diode characterization

The quality of a Schottky diode is usually evaluated by its current-versus-voltage (IV)-curve, which is obtained by measuring the current flowing through the diode while scanning the voltage bias. The last deposited layer is masked with a hexagonal-array of shadow-masked, 250 μm , 100 nm thick, circular contacts. The top contacts for the devices presented in Chapter 3 are silver, and dZnO for those in Chapter 5. Depending on the configurations, this last layer can be anode or cathode.

Theoretically, a good Schottky diode should have high forward bias conductivity and low reverse bias current. Here, the current at +1 or +2 V forward bias and the asymmetry, the ratio of the current at +/- 1 V, are chosen as the basic parameters for diode performance. Figure 2.14 shows a good diode curve characteristic of a well-formed Schottky contact and a non-ideal diode curve characteristic of an ohmic contact obtained from different samples.

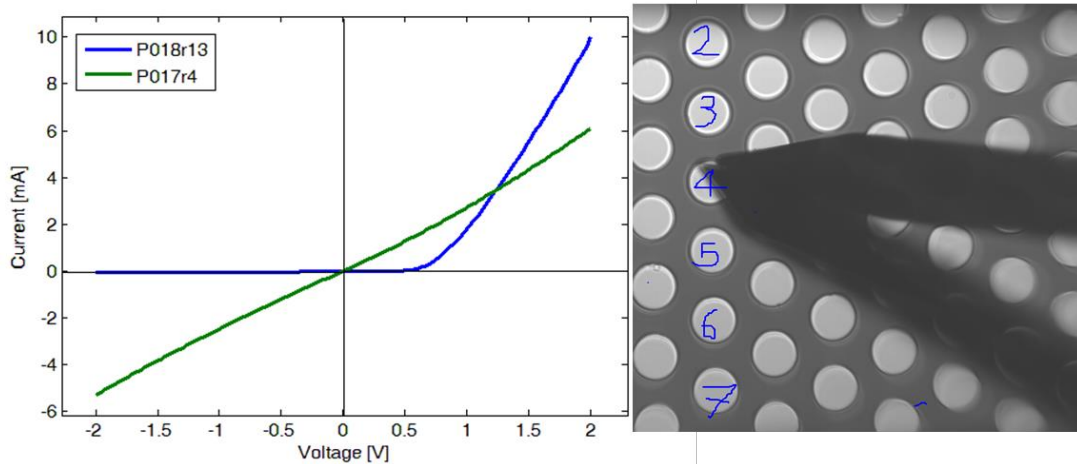


Figure 2.14. Left: Diode curve (blue) of sample P018r13 and ohmic junction of a failed device. Right: Image of the silver top contacts of prism sample P018r18 and probe tip.

The IV curves were fitted by using the typical diode current-voltage relation for a Schottky diode given by:

$$I = I_0 \left(e^{q(V-IR_s)/nkT} - 1 \right) + \frac{V-IR_s}{R_{shunt}} \quad (2.3)$$

where I_0 is the saturation current, which is related to the barrier height of the junction, kT is thermal energy (0.025V at room temperature), n is the ideality factor, R_s is the series resistance, R_{shunt} is the shunt resistance, I is the current through the diode, and V is the voltage applied across the diode. The fitting parameters are I_0 , n , R_s and R_{shunt} . A fitting program was written to extract the fitting parameters as well as their fitting errors to help assess the large number of devices studied. The fitting parameters can supply information about diode performance of the measured devices and their dependence on material deposition methods. These parameters were compared to the photovoltaic test results to search for correlations between the diode quality and the photovoltaic response, and their connection with material deposition parameters. Details of the fitting procedure and parameter extraction of the diode curves are presented in Appendix B.

2.5. Optical and Optoelectronic Characterization Techniques

The characterization of the optical response of the devices presented in Chapter 3 and Chapter 5 are modeled after the standard metrics used for silicon photovoltaic characterization. The principal figures of merit are: open circuit voltage (V_{oc}), short circuit current (I_{sc}), fill factor (FF), internal quantum efficiency, (IQE), and external quantum efficiency (EQE).

V_{oc} is the voltage that develops across the device contacts under illumination when no current flows. I_{sc} is the current that flows across the device under illumination when the voltage across the device is zero. The FF (see Equation 2.4) is given as a percentage, and it measures the fraction of the area of the IV curve defined by the product of V_{oc} and I_{sc} that is encompassed by the smaller area defined by the voltage and current measured at the device's maximum power output (Figure 2.15). Quantum efficiency is defined in Section 1.4 of the previous Chapter.

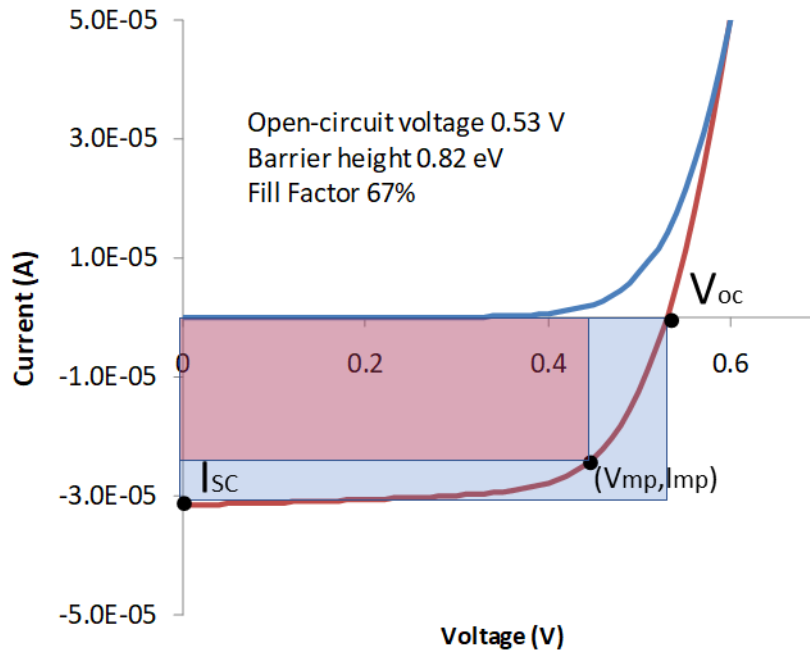


Figure 2.15. Fill Factor of prism sample P011r21. The red area fraction of the blue area is the fill factor.

2.5.1. Otto Coupled Devices

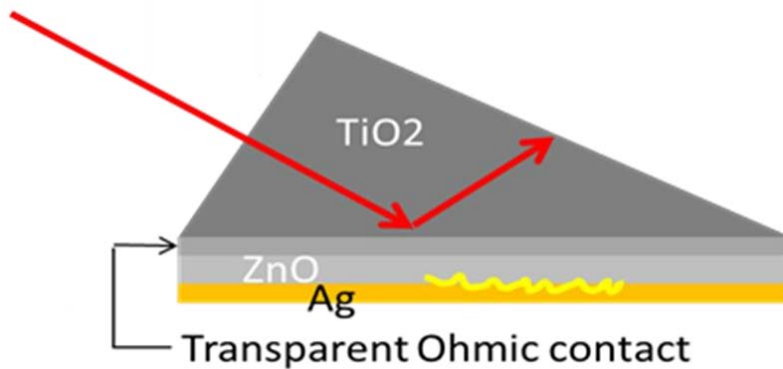


Figure 2.16. Cartoon of the Otto configured prism devices. 2%AlZnO doped zinc oxide is the transparent contact.

The device design presented in Chapter 3 exhibits an SPP-mediated photovoltaic response. The design considerations to maximize device performance discussed in the next chapter necessitated the selection of the Otto coupling mechanism. Degree of

optical coupling, and SPP excitation of a prism sample were dependent on the index of refraction, and the thickness of the dZnO, ZnO, and Ag layers according to the coupling equations outlined in Otto's seminal work from 1968²².

By modeling these equations computationally, a map of the TiO₂ prism/dZnO/ZnO/Ag optical coupling behavior with layer thickness can be obtained. The stack of dZnO/ZnO, (treated as a uniform layer of ZnO) should be tuned to support efficient SPP excitation within the accessible angle range. Figure 2.17 shows the minimum reflectivity (a measure of maximum optical coupling) from the multilayer as a function of both the ZnO and Ag thickness. When the Ag layer is thicker than 100 nm, the coupling will not depend on Ag thickness. Thus, for prism top contacts, the Ag layer target thickness is safely chosen to be 150 nm. The ZnO thickness, referring to the dZnO/ZnO stack, on the other hand, should have a combined thickness of approximately 200 nm for 633 nm light to achieve minimum reflectivity. Note the optimal ZnO thickness depends on its refractive index, which could be different under different deposition conditions. These calculations were performed for all wavelengths tested in Chapter 3.

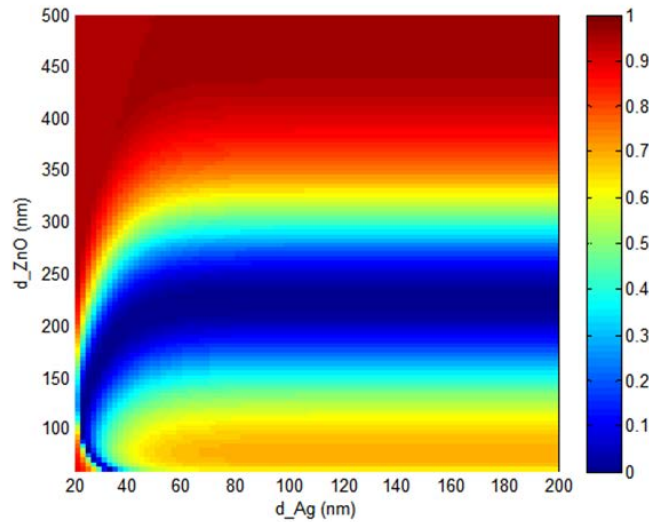


Figure 2.17. Otto configuration TiO₂/ZnO/Ag The coupling (reflectivity, R) as a function of ZnO and Ag thickness, d, at 633 nm. The colour scale represents reflectivity (Coupling is insensitive to Ag thickness beyond ~80 nm)

The calculations were refined with a constant thickness of 150 nm of silver in order to explore the dependence of ZnO stack layer thickness on coupling angle at a wavelength 633 nm (Figure 2.18). The angle of maximum theoretical coupling was calculated to be 61.8°. The optimal thickness of the ZnO stack was also confirmed to be 200 nm.

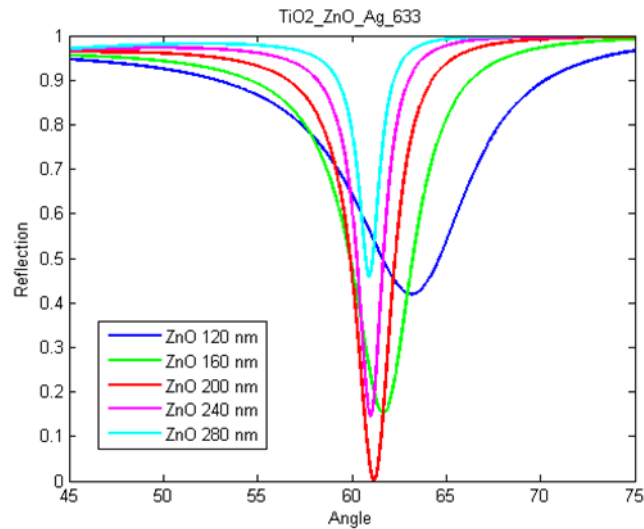


Figure 2.18. Otto configuration TiO₂/ZnO/Ag Effect of ZnO stack thickness for 633 nm light.

In order to design prism devices that could efficiently support SPPs at different incident photon wavelengths a computational study was conducted to determine the optimal ZnO stack thickness and coupling angle for different photon energies. The large range of angles that resulted necessitated the use of hemispherical prisms as the TiO₂ substrates for some of the subsequent experiments (Figure 2.19)

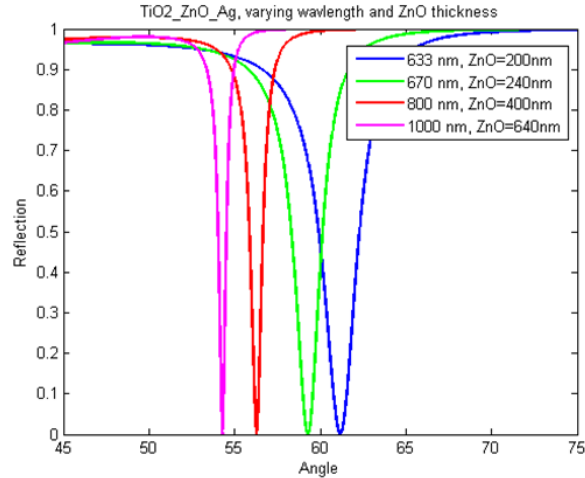


Figure 2.19. Calculated wavelength and ZnO stack thickness dependence for optimal coupling for devices with 150 nm thick Ag top contacts.

The electric field intensity at the SPP active interfaces of the prism sample designs were modeled using finite difference time domain (FDTD) simulations²⁴ with the commercially available software package, Lumerical FDTD Solutions. The FDTD method is a grid-based method for solving differential equations. Lumerical employs a 3-dimensional mesh to solve Maxwell's equations by computing the electric and magnetic fields (E and H) at grid points spaced by Δx , Δy , and Δz apart, with E and H interlaced in all three spatial dimensions. As the name implies, FDTD methods provide a time domain solution to Maxwell's equations. Frequency analysis is obtained through fast Fourier transform methods. The Maxwell equation solutions provide for an accurate and reliable understanding of the effects of scattering, transmission, reflection, absorption, etc. These methods have been employed to simulate the optical properties of the fabricated structures described in Chapters 3-5. Details of FDTD simulation parameters utilized in Chapter 5 are presented in Appendix B.

FDTD simulations were employed to deduce the field intensities of the standard 633 nm prism design structures as shown in Figure 2.20. Consistent with the expectations of Equation 1.2, the field decays exponentially normal to the interface with decay length determined by the material permittivity.

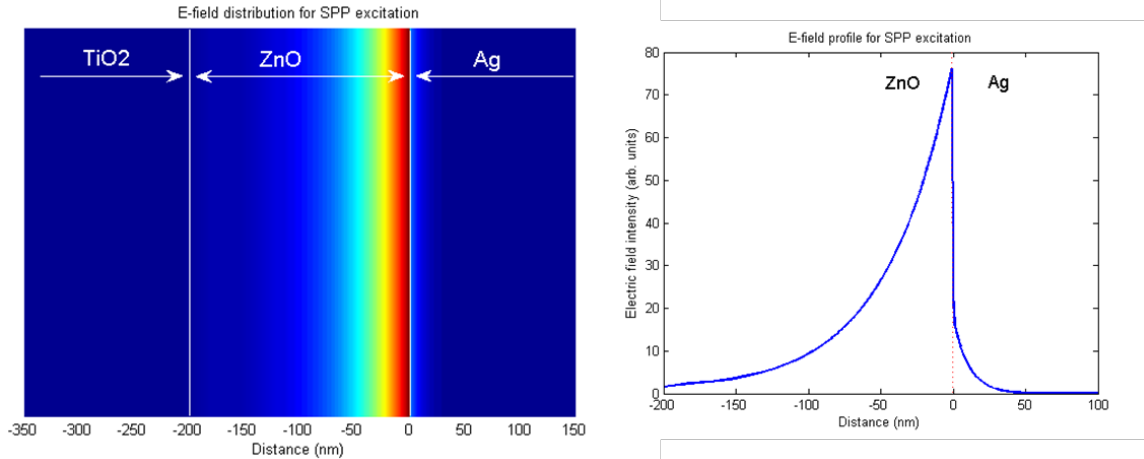


Figure 2.20. FDTD simulation of field enhancement at the Ag/ZnO interface. The field at the surface is enhanced 77 times over the field of the incident photon and decays exponentially into the dielectric and metal layers (see Section 1.11).

The degree of coupling was also investigated as a function of surface roughness using Lumerical simulations (Figure 2.21). The trend of decreasing coupling efficiency, and absorption peak broadening with increasing surface roughness is apparent. Though some have argued that surface roughness at the SPP active interface could increase the probability of IPE²³, it was found experimentally that the opposite was true for prism devices. This is likely due to the fact that surface roughness increased the interface defect density leading to surface charges and local non-uniformities that provided pathways for IPE emitted electrons to recombine with the silver through tunneling (Section 1.3 and 1.4).

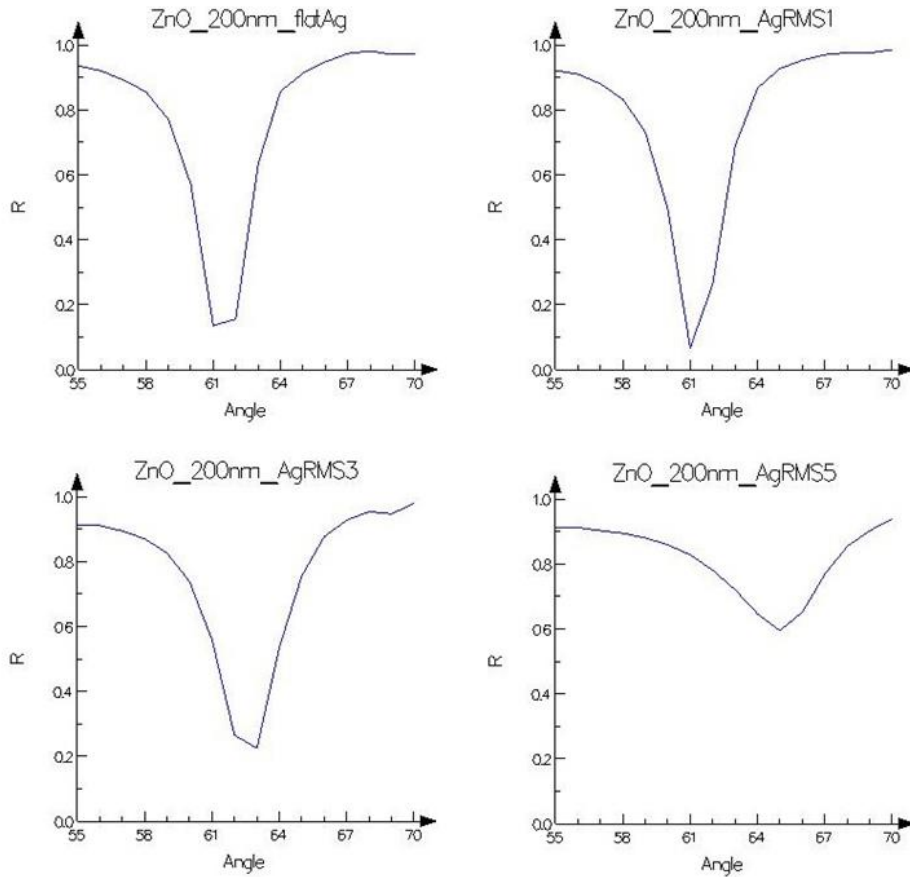


Figure 2.21. Otto configuration TiO₂/ZnO (200 nm)/Ag with surface roughness: the simulated reflectance vs angle for flat (top left) Ag, and rough ZnO-Ag interfaces with RMS roughness = 1 nm (top right), 3 nm (bottom left), and 5 nm (bottom right),

Prior to photovoltaic response testing, the coupling efficiency of the prism samples was measured systematically by mapping out the angle-dependent reflection from the thin film stacks. Surface reflections and transmissions were calculated to correct the angle-dependent error. Figure 2.22 shows a typical coupling curve for the Prism series samples. It is clearly seen at the coupling angle the reflectance from the sample almost vanishes. For this particular sample, the coupling efficiency is approximately 99%. Figure 2.23 shows a histogram of coupling efficiencies for the sample set over time. After refining the fabrication conditions, the coupling efficiency of the devices was seen to reach a reproducibly high level.

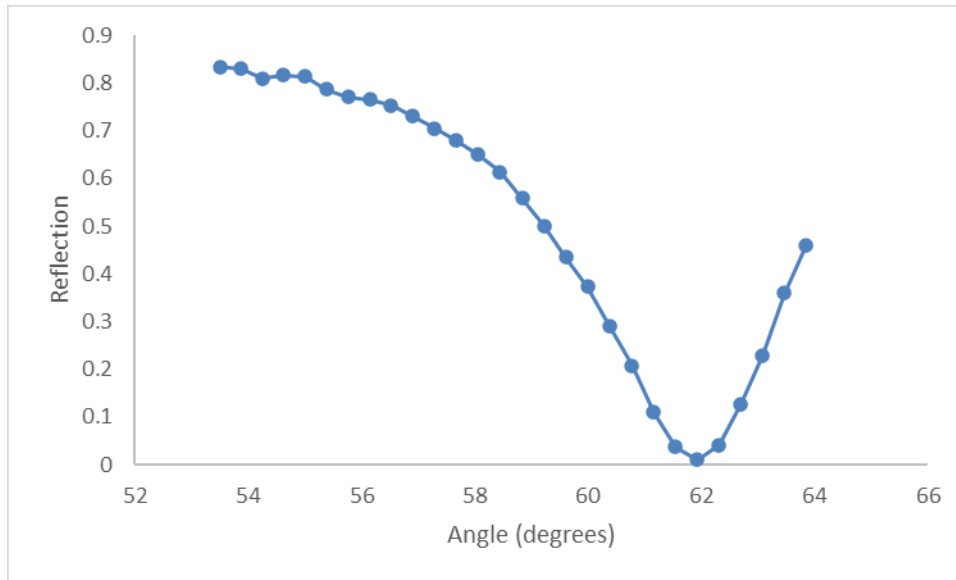


Figure 2.22 Reflectivity versus coupling angle for prism sample P015r7 with ~99% coupling efficiency at 633 nm

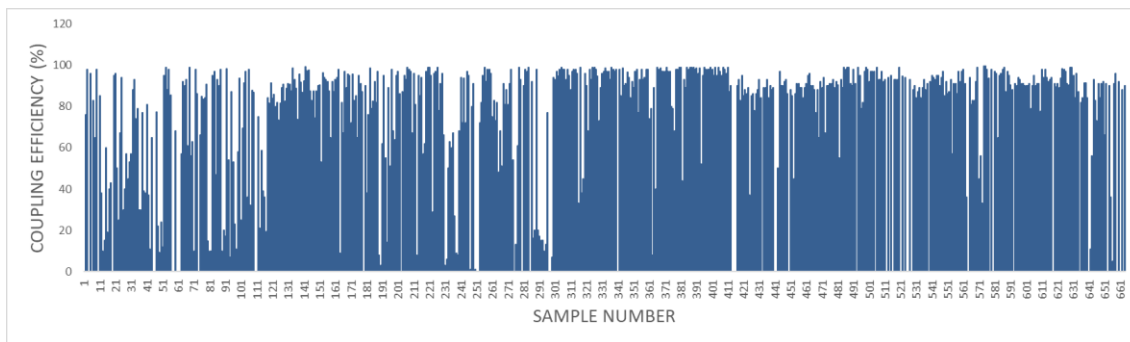


Figure 2.23 Coupling efficiency of prism samples over time showing reproducibility increasing over time.

Photovoltaic characterization of the prism sample set was carried out by measuring the photocurrent under illumination with different wavelengths at an intensity equivalent of one sun. Most samples were built to maximize coupling at 633 nm. The photovoltaic response was measured under static conditions to extract quantum efficiency (QE) and open-circuit voltage (V_{oc}). The IV curve under illumination was also recorded to extract additional information such as the device fill factor. The IQE and EQE were calculated according to Equations 1.14 and 1.15 and the FF was calculated according to Equation 2.4:

$$FF = (I_{mp} \times V_{mp}) / (I_{sc} \times V_{oc}) \times 100\% \quad (2.4)$$

Where I_{mp} is the current at maximum observed device power and V_{mp} is the voltage at that same point. Figure 2.24 presents a histogram of the change in internal quantum efficiency and open circuit voltage of the prism sample set over time for several hundred devices. The improvement of efficiency with iterative improvements in the device fabrication process is readily observed.

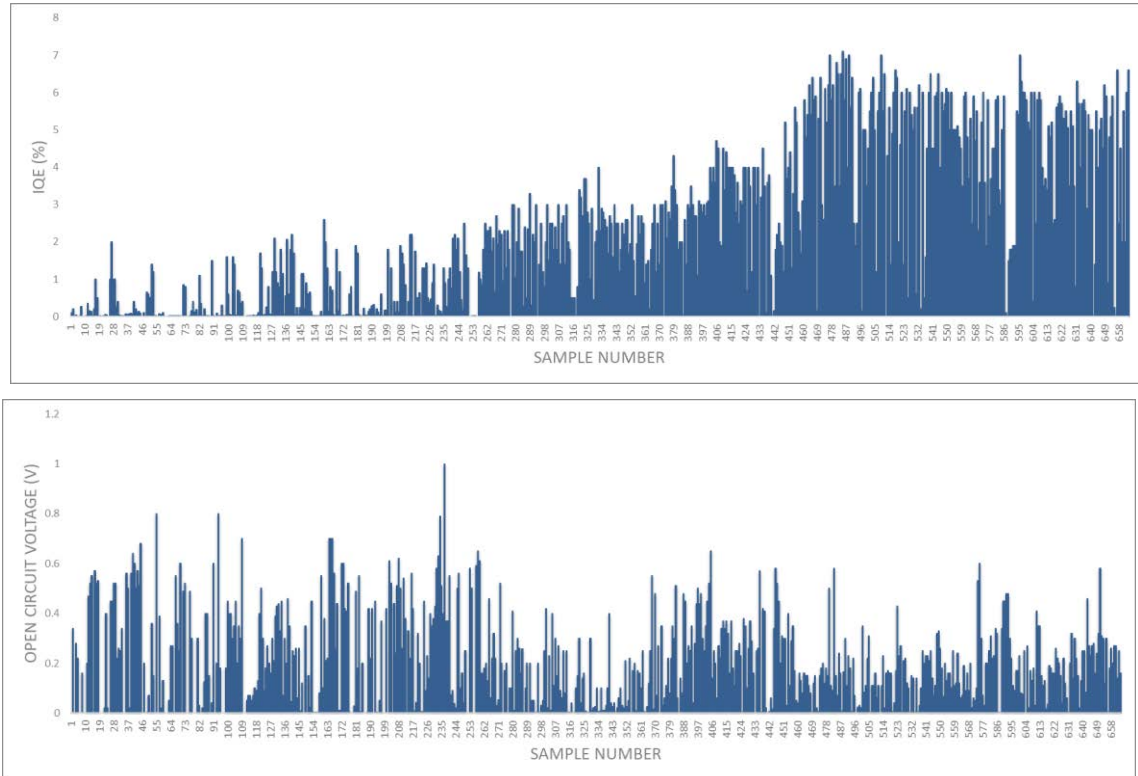


Figure 2.24. Photovoltaic response (upper) and open circuit voltage (lower) over time for the prism device sample set.

The large majority of devices were characterized using a Thorlabs HTPS-1 tunable helium-neon laser at a wavelength of 633 nm, focused to a spot size of 50 μm , and attenuated to 1 sun of intensity. The wavelength dependent response reported in Chapter 3 was obtained by making measurements with the HeNe laser tuned to 543 nm and 594 nm. Longer wavelength photoresponse was obtained with a Ti:Sapphire (Spectra Physics Tsunami) operated in continuous wave mode tunable from 720 to 800 nm, leading to the Fowler plot presented in Figure 3.13.

2.5.2. Free-Space Coupled Nanostructured Devices

The characterization of photovoltaic response from the nanostructured sample set, presented in Chapter 5, was complicated by the fact that the high throughput design was tailored for ease of iterative improvement in the quality of the device layers enabled by the commercially available nanostencils, and not for exploring the plasmonic response in the wavelength range explored with the prism-based devices. Unfortunately, nanostencil patterns with periodicity and feature size that would have yielded plasmonic response in the optical region were not available. Rather, the available nanostencil-enabled plasmonic response appears in the near infrared (NIR), necessitating alternative optical characterization methods than those employed for the prism devices. Use of the Thorlabs HTPS-1 tunable helium-neon laser at a wavelength of 633 nm resulted in low absorbance of the substrates at this wavelength, far from the NIR absorption peaks calculated from FDTD simulations (Figure 5.6). Quantifying the response of these free space-coupled structures was further complicated by the inherent scattering characteristics of the nanostructures and the difficulty in capturing scattered light from the sample surface, required to properly quantify device efficiency.

A new NIR-based optical characterization set up was commissioned using a 75 MHz repetition rate, Ti:sapphire excitation laser (Coherent, Chameleon) tunable from 680-1080 nm. The tunable laser was used to illuminate the samples at 1 sun incident intensity, across the bandwidth of the intense narrow resonant absorption peaks of the LRSP-based nanostructured devices (see Figure 5.6). Absorption, reflection and scattering from the samples required light capture with an integrating sphere to accurately measure the absorbance of the samples under irradiation. The limitation of this setup was that the measurements could not be made at normal incidence, due to the geometry of the integrating sphere. Since the absorption of resonant plasmonic nanostructure arrays is sensitive to light incidence angle and polarization, a small off-normal incident angle of 10 degrees was employed so that a meaningful comparison to the FDTD simulations performed assuming normal incidence could be maintained. The resultant absorption spectrum is presented in Figure 5.7.

The IQE, EQE, V_{oc} , and FF photovoltaic response of the nanostructured samples was measured, using the Keithley 2400 source meter with serial interface, in a manner similar to that used for the prism samples, except that the absorbed power was adjusted to match the value extracted from integrating sphere measurements, in order to compensate for undetected light scattered from the surface.

2.6. Confocal Microscopy and Plasmonically Enhanced Nonlinear Optical Techniques

Optical characterization of the nanostructured Ag/ZnO devices in the NIR spectral range of their resonant response required the use of the ultrafast Ti:sapphire laser combined with an integrating sphere, as described. While the characterization of the device photovoltaic efficiency was carried out under conditions of low illumination intensity (with an incident intensity equivalent of 1 sun), the high peak intensity of these ultrashort laser pulses also affords their use in other characterization methods, including multiphoton confocal microscopy when this laser is coupled to a confocal microscope. At the focus of the microscope objective, the peak intensities of the laser can reach levels where the nonlinear optical response of the sample becomes measurable and can provide new avenues to probe the nanostructured devices, beyond those available with the sample's linear optical response. In this thesis, two primary nonlinear optical methods have been employed. The first is known as two photon photoluminescence (2PPL) microscopy and the second is second harmonic generation (SHG) microscopy. In practical terms, their implementations are very similar and rely only on different detection mechanisms within the laser confocal microscope. However, they result from very different physical phenomena and can provide complementary information about the sample.

Confocal microscope images discussed in this thesis were obtained with a Leica TCS SP5 II microscope equipped with a HCX PL APO CS 10x/0.4 IMM objective and a 75 MHz repetition rate, dispersion compensated, Chameleon excitation laser with pulse widths of 140 femtoseconds (Coherent) tunable from 680-1080 nm with a typical output power of 3.5 W at 800 nm (low resolution SHG image), and with a Zeiss LSM 510 MP microscope equipped with an LD Plan-Neofluar 63x/0.75 NA Korr objective lens and a

75MHz repetition rate, 140 fsec Chameleon Ultra excitation laser tunable from 710-980 nm (pillar-resolved SHG images and fluorescence lifetime imaging (FLIM) measurements). In practice, a small portion of the available short pulse laser output (typically on the order of 10 mW) is incident on the sample to prevent rapid sample degradation and burning that can occur at higher incident intensity. Nevertheless, even at these relatively low average powers, the peak intensities of the ultrashort pulses can drive nonlinear optical material response.

Nonlinear optics (NLO) can be understood, from the most straightforward perspective, as an optical phenomenon that results from an intensity-dependent change in the polarizability of a material interacting with the oscillating electric field of an incident light pulse. The resultant induced dipole gives rise to a nonlinear polarization summarized by Equation 2.5:

$$P = \chi^{(1)}E + \chi^{(2)}E^2 + \chi^{(3)}E^3 + \dots \quad (2.5)$$

Where P is the induced dipole per-unit volume, $\chi^{(1)}$ is the linear susceptibility that describes classical linear optics, and $\chi^{(2)}$ describes second order effects such as second harmonic generation (SHG), and two photon photoluminescence (2PPL), two processes that feature in Chapter 4 and Chapter 5. The simplicity of Equation 2.5 belies the underlying complexity of nonlinear processes²⁶. χ is often treated as a complex mathematical tensor that reflects material symmetry- and polarization-dependent response. In short, complex lattice structures combined with photon electric fields oscillating in myriad ways with respect to each other, give rise to non-intuitive electromagnetic processes. The first order susceptibility $\chi^{(1)}$ is by far the simplest to understand and calculate. Even so, through a reading of Chapter 1 and its basic treatment of the linear polarizability of materials, it is apparent that it is by no means trivial.

The second order susceptibility $\chi^{(2)}$ governs two-photon nonlinear processes and is orders of magnitude smaller than $\chi^{(1)}$ ($\chi^{(2)}$ is approximately 10^{12} times smaller than $\chi^{(1)}$). From Equation 2.5, second order nonlinear polarization changes depend on the electric field amplitude squared (E^2). The small relative value of $\chi^{(2)}$ and the square dependence on the intensity of the field means that second order optical processes only become significant at large incident intensities, such as the peak intensities of ultrashort

laser pulses. Some common second order nonlinear optical phenomena include two-photon absorption, second harmonic generation, sum frequency generation, difference frequency generation, and optical parametric generation, among others.

The plasmonic response of the nanostructured samples was investigated through 2PPL – a process in which the sample undergoes two-photon absorption, followed by relaxation and luminescence. Though 2PPL from organic systems is well understood and generally accepted to originate from instantaneous two-photon absorption (Figure 2.28 Left) followed by relaxation and luminescence²⁷, some controversy about the mechanism of 2PPL in noble metal plasmonic structures remains^{28,29}. Recent pump-probe studies present strong evidence for a mechanism that is dominated by two sequential one-photon absorption processes (Figure 2.28 Right).

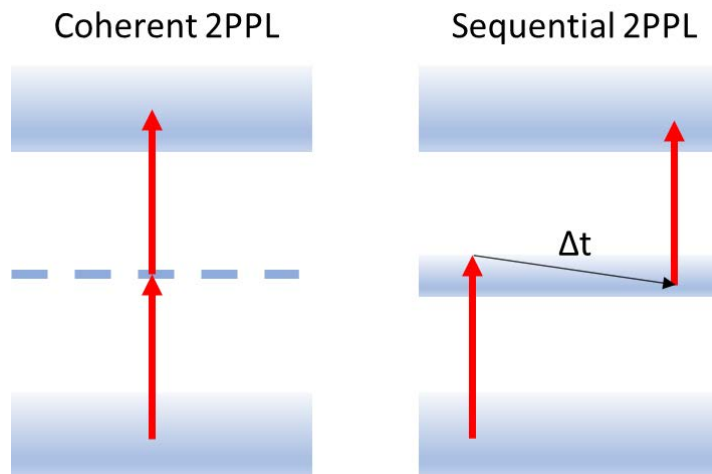


Figure 2.25. The excitation mechanism of two photon photoluminescence (2PPL), Left) the instantaneous two photon excitation common for organic dyes. Right) two sequential excitations. Δt indicates a nanoparticle shape dependent relaxation time on the order of picoseconds.

The sequential 2PPL mechanism is thought to involve a first photon-induced intraband excitation to a real excited state above the Fermi level. The excited electron loses energy to thermalization processes such as electron-electron and electron-phonon scattering within the s-p band before the second photon further excites the system, leading to broad bandwidth 2PPL emission with an energy less than or equal to twice the incident energy. The pump-probe decay time of the sequential 2PPL excitation was

observed to be 3-4 picoseconds, depending on the shape of the gold nanostructure studied. It should be noted that in the absence of time resolution in the multiphoton absorption process, the signatures of instantaneous two-photon absorption followed by relaxation and luminescence result in very similar 2PPL emission characteristics and the two mechanisms cannot readily be distinguished in most 2PPL experiments. As a result, regardless of the mechanism, 2PPL has become a well-accepted proxy for measurement of the plasmonic field distribution in these noble metal nanostructures.

This thesis also describes the results of experiments in which time correlated single photon counting (TCSPC) methods have been employed to monitor the fluorescence lifetime characteristics of the photoexcited device nanostructures. TCSPC methods combined with confocal microscopy enables confocal fluorescence lifetime imaging microscopy (FLIM)³⁰, a method that provides a map of lifetime information from the sample, providing a link between spatial position and local dynamics. The instrument used in this research had an effective time resolution of ~100 picoseconds. FLIM imaging of the luminescence from the nanostructured devices presented later in this thesis employ time-resolved spectroscopy methods to deconvolute the emission from different distinct processes on the basis of their different lifetime behaviour.

In addition to 2PPL imaging, this thesis also describes the results of second harmonic generation imaging performed with the laser confocal microscope. Second harmonic generation is the most commonly observed second order nonlinear optical effect and it results from the simultaneous excitation of a material by two incident photons to generate a 3rd photon at twice the frequency (Figure 2.25). SHG, and all other second order NLO processes, can only occur when the medium possesses a non-centrosymmetric structure. SHG is a consequence of the non-linear polarizability of electron density within an anharmonic potential environment. When electrons within these environments experience the sinusoidally oscillating electric field of a photon, their polarization is constrained by their anharmonic environment. The asymmetry of the oscillating polarization can be described mathematically as a superposition of sinusoidal frequencies with one component at the frequency of the incident field and a second component with twice the frequency. SHG results from the emission associated with the polarization component at twice the incident frequency. SHG is only observed in non-centrosymmetric environments because symmetry considerations mean that SHG is suppressed by destructive interference in the centrosymmetric case. .

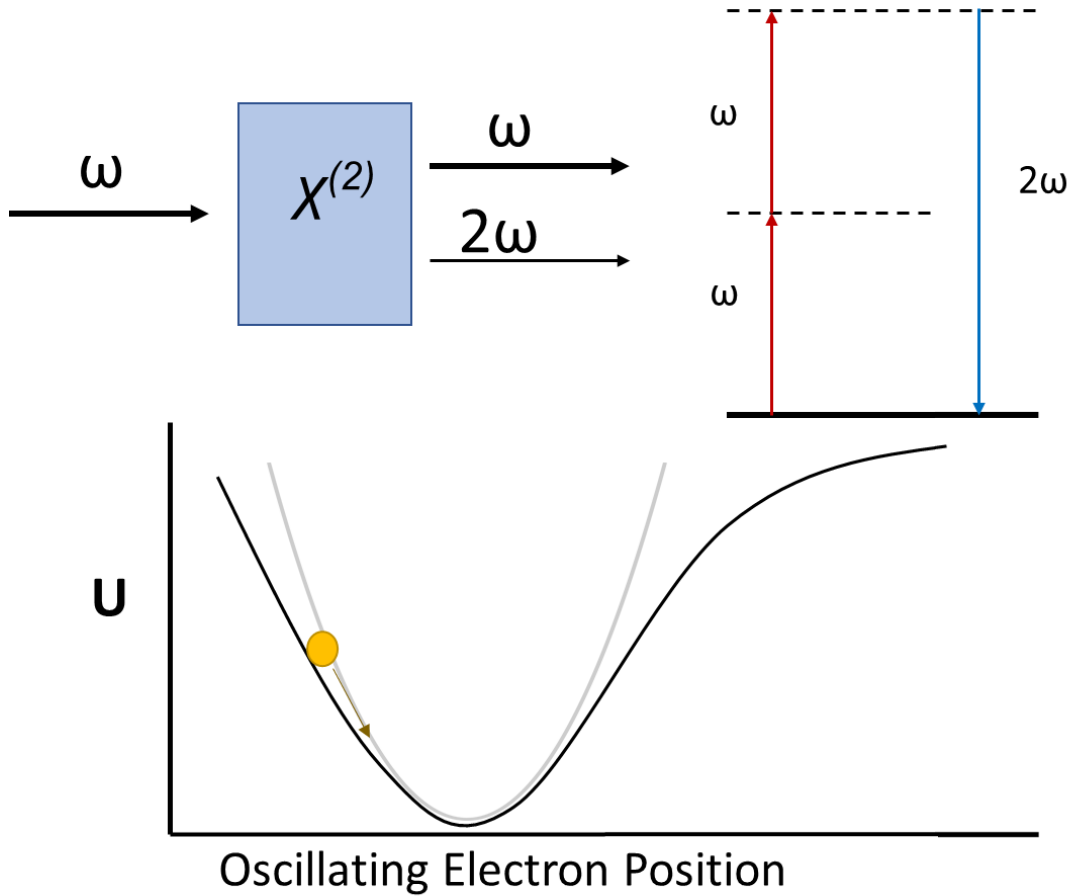


Figure 2.26. top) The SHG process mediated by a virtual transition state. bottom) The anharmonic potential environment that supports second order non linear optical processes in a non-centrosymmetric environment.

A consequence of this wave mixing for light travelling in a medium is the requirement that the momentum of the incident light and that of the SHG light be matched to prevent phase mismatch and destructive interference. This wave vector matching is a rare condition, partly because a mathematical treatment reveals that maximum intensity is achieved when:

$$\mathbf{k}_{\omega SH} = \mathbf{k}_{\omega 1} + \mathbf{k}_{\omega 2} \tag{2.6}$$

where k is the momentum of the SHG photon and the 2 incident photons, respectively. The value of k is given by:

$$\mathbf{k}_\omega = n(\omega) \times \frac{\omega}{c} \quad (2.7)$$

where $n(\omega)$ is the frequency-dependent value of the refractive index and c is the speed of light. Because of the tendency for dispersion to increase the index of refraction with frequency (see Section 1.1), in most geometries the momentum of the higher energy emitted photon will never match the momentum of the two incident photons. Carefully selected birefringent geometries can give rise to excellent momentum matching, resulting in intense SHG²⁶ and other NLO phenomena.

In the case of the plasmonically active structures presented in Chapters 3 and 4, the zinc oxide (~100 nm thick) and doped zinc oxide (~100 nm thick) films are deposited by sputtering (see section 2.1) to conformally coat the silver nanostructured layers. Zinc oxide is a polar material and displays non-centrosymmetry along its $\langle 0001 \rangle$ c -axis direction which deposits preferentially normal to the silver surface on planar silver films. The plasmonic absorption of light by the silver surface generates very high surface fields in the vicinity of the nanostructures. Since the second order nonlinear contribution to the induced dipole is dependent on the electric field amplitude squared (Equation 2.5) and the intensity of light emitted from a dipole is proportional to the square of the dipole polarization, the intensity of the SHG scales as the fourth power of the electric field amplitude. The intensity of the electric field (E^2) in the near surface region, observed to be very high for SPPs (Figure 2.2), can be assumed to be significantly enhanced through plasmonic excitation and decays exponentially into the ZnO overlayer within tens of nanometers. Such intense fields enhance the SHG within the excited volume by the square of the intensity. For plasmonic fields confined to the few tens of nanometers of the Ag/ZnO interface, phase mismatch between fundamental and second harmonic photons are expected to be inconsequential. Thus, SHG microscopy images obtained in this work result from the convolution of plasmonic field enhancements in the vicinity of the Ag/ZnO nanostructures and how these enhanced local fields are distributed and interact within the non-centrosymmetric ZnO overlayer. SHG microscopy of the Ag/ZnO structures is discussed in more detail in Chapters 4 and 5.

References

- 1 Mattox, D.M., 2010. *Handbook of physical vapor deposition (PVD) processing*. William Andrew.
- 2 Seshan, K., 2002. *Handbook of Thin Film Deposition Techniques Principles, Methods, Equipment and Applications, Second Edition*. CRC Press.
- 3 Kern, W., 1990. The evolution of silicon wafer cleaning technology. *Journal of the Electrochemical Society*, 137(6), p.1887.
- 4 Ohring, M., 2001. *Materials science of thin films*. Elsevier.
- 5 Venables, J., 2000. *Introduction to surface and thin film processes*. Cambridge University Press.
- 6 Seshan, K., 2002. *Handbook of Thin Film Deposition Techniques Principles, Methods, Equipment and Applications, Second Edition*. CRC Press.
- 7 MacNab, F., 2006. Thin film transistors from II-IV semiconductors on polymer substrates.
- 8 Janotti, A. and Van de Walle, C.G., 2009. Fundamentals of zinc oxide as a semiconductor. *Reports on progress in physics*, 72(12), p.126501.
- 9 Özgür, Ü., Alivov, Y.I., Liu, C., Teke, A., Reshchikov, M., Doğan, S., Avrutin, V.C.S.J., Cho, S.J. and Morkoç, A.H., 2005. A comprehensive review of ZnO materials and devices. *Journal of applied physics*, 98(4), p.11.
- 10 Mack, C., 2008. *Fundamental principles of optical lithography: the science of microfabrication*. John Wiley & Sons.
- 11 Chen, H.T., Taylor, A.J. and Yu, N., 2016. A review of metasurfaces: physics and applications. *Reports on progress in physics*, 79(7), p.076401.
- 12 Simpson, J.T., Hunter, S.R. and Aytug, T., 2015. Superhydrophobic materials and coatings: a review. *Reports on Progress in Physics*, 78(8), p.086501.
- 13 Lahiri A, Shah N, Dales C. Building a safer, denser lithium-ion battery. *IEEE Spectrum*. 2018 Feb 28;55(3):34-9.
- 14 Du, K., Ding, J., Wathuthanthri, I. and Choi, C.H., 2017. Selective hierarchical patterning of silicon nanostructures via soft nanostencil lithography. *Nanotechnology*, 28(46), p.465303.

- 15 Speets, E.A., te Riele, P., van den Boogaart, M.A., Doeswijk, L.M., Ravoo, B.J., Rijnders, G., Brugger, J., Reinhoudt, D.N. and Blank, D.H., 2006. Formation of Metal Nano-and Micropatterns on Self-Assembled Monolayers by Pulsed Laser Deposition Through Nanostencils and Electroless Deposition. *Advanced functional materials*, 16(10), pp.1337-1342.
- 16 Du, K., Ding, J., Liu, Y., Wathuthanthri, I. and Choi, C.H., 2017. Stencil lithography for scalable micro-and nanomanufacturing. *Micromachines*, 8(4), p.131.
- 17 Vazquez-Mena O, Sannomiya T, Tosun M, Villanueva LG, Savu V, Voros J, Brugger J., 2012 High-resolution resistless nanopatterning on polymer and flexible substrates for plasmonic biosensing using stencil masks. *ACS Nano.*, 6(6):5474-81.
- 18 Reimer, L., 2000. Scanning electron microscopy: physics of image formation and microanalysis.
- 19 Fultz, B. and Howe, J.M., 2012. *Transmission electron microscopy and diffractometry of materials*. Springer Science & Business Media.
- 20 Le Bail, A., Cranswick, L.M., Madsen, I., Fitch, A., Allmann, R., Giacobozzo, C., Altomare, A., Cockcroft, J.K., Caliandro, R., Norby, P. and Scardi, P., 2008. *Powder diffraction: theory and practice*. Royal society of chemistry.
- 21 Munroe, P.R., 2009. The application of focused ion beam microscopy in the material sciences. *Materials characterization*, 60(1), pp.2-13.
- 22 Otto, A., 1968. Excitation of nonradiative surface plasma waves in silver by the method of frustrated total reflection. *Zeitschrift für Physik A Hadrons and nuclei*, 216(4), pp.398-410.
- 23 Grajower, M., Levy, U. and Khurgin, J.B., 2018. The role of surface roughness in plasmonic-assisted internal photoemission schottky photodetectors. *Acs Photonics*, 5(10), pp.4030-4036
- 24 Kunz, K.S. and Luebbers, R.J., 1993. *The finite difference time domain method for electromagnetics*. CRC press.
- 25 Sarangan, A., 2016. *Nanofabrication: Principles to Laboratory Practice*. CRC Press.
- 26 Boyd, R.W., 2020. *Nonlinear optics*. Academic press.
- 27 Jiang, X.F., Pan, Y., Jiang, C., Zhao, T., Yuan, P., Venkatesan, T. and Xu, Q.H., 2013. Excitation nature of two-photon photoluminescence of gold nanorods and coupled gold nanoparticles studied by two-pulse emission modulation spectroscopy. *The journal of physical chemistry letters*, 4(10), pp.1634-1638.

- 28 Wang, H., Huff, T.B., Zweifel, D.A., He, W., Low, P.S., Wei, A. and Cheng, J.X., 2005. In vitro and in vivo two-photon luminescence imaging of single gold nanorods. *Proceedings of the National Academy of Sciences*, 102(44), pp.15752-15756.
- 29 Imura, K., Nagahara, T. and Okamoto, H., 2005. Near-field two-photon-induced photoluminescence from single gold nanorods and imaging of plasmon modes. *The Journal of Physical Chemistry B*, 109(27), pp.13214-13220.
- 30 Datta, R., Heaster, T.M., Sharick, J.T., Gillette, A.A. and Skala, M.C., 2020. Fluorescence lifetime imaging microscopy: fundamentals and advances in instrumentation, analysis, and applications. *Journal of biomedical optics*, 25(7), p.071203.

Chapter 3.

High Efficiency Plasmonic Hot Electron Rectification at Planar Ag/ZnO Schottky Junctions*

3.1. Introduction

The dynamics of plasmonic hot carrier generation and their emission across interfaces has been a focus of investigation in recent years.^{1,2,3} Interest in the emission of hot carriers that result from surface plasmon decay stems from their broad application to new forms of photovoltaic conversion, optical and IR detectors, redox active surfaces, and catalysis.^{4,5,6}

Research in this area has primarily focused on photovoltaic conversion across Schottky junctions.³ Hot carrier plasmonic devices of this type, rectify current through an inelastic internal photoemission mechanism. By matching a plasmonically active metal surface to a suitably chosen semiconductor junction, hot carriers (electrons or holes), generated by plasmon decay and with sufficient momentum, can ballistically emit from the plasmonic metal surface by surmounting the Schottky junction energy barrier (Figure 3.1). Photovoltaic current with a voltage equal to the Schottky barrier energy can be rectified in this manner. Several research groups have fabricated devices of this class and explored the theoretical constraints on the ultimate efficiency of the internal photoemission mechanism.^{7,8,9}

In most cases, a comprehensive study of hot carrier device performance has been hampered by material and fabrication challenges, and by nanopatterned, free space-coupled device designs that are prone to scattering, and that make wavelength-dependent efficiency measurements difficult. Identifying and overcoming fabrication, material, and design obstacles towards high quantum efficiency plasmonic photovoltaics

* The author had a major contribution to device design and fabrication, and electrical characterization (along with Dr. Claire McCague, Dr. Kourosh Khosraviani, Dr. Jayna Chan, Steven Gou, and Greg Wong), as well as analysis of data (all team members; see acknowledgements). The author had a minor contribution to the SEM imaging and XRD measurements (along with Dr. Xin Zhang and Dr. Enrico Bovero), and minimal contribution to optical characterization and simulation (along with Dr. Murat Cetinbas, Dr. Tom Johansson, and Dr. Haijun Qiao). The majority of the data presented in Chapter 3 was gathered as part of a commercially-funded research project.

that serve as an effective experimental platform for the study of hot carrier dynamics in plasmonic systems is a major focus of this work.

In the case of the devices presented here, careful consideration of material combinations, device geometry, and fabrication processes must be undertaken in order to achieve the most efficient photoconversion possible. Device performance depends on three mechanistic processes that occur in sequence: i) coupling of free space photons to surface plasmons, ii) the decay of the excited surface plasmons into hot electrons with energy $h\nu$, and iii) the inelastic internal photoemission of the generated hot electrons over the Schottky barrier into the conduction band of the adjacent dielectric material. The present work explores the performance of hot electron Schottky junction rectifying devices, rationally designed to explore the structure-function relationships between device efficiency and the above factors.

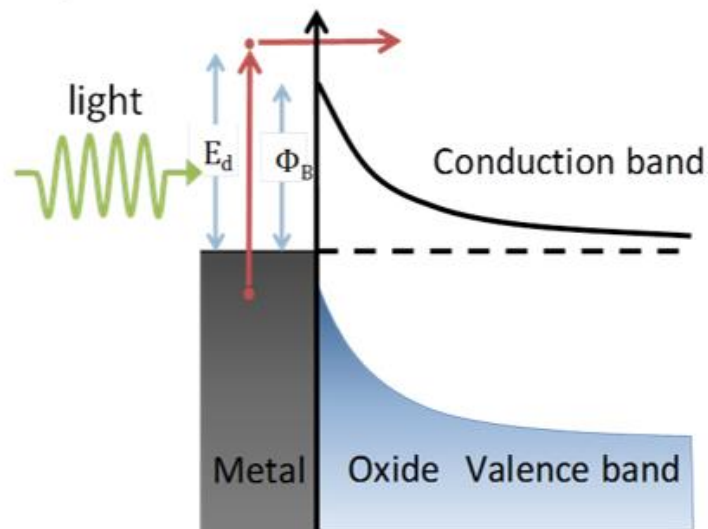


Figure 3.1. Three step internal photoemission mechanism across a Schottky junction: i) coupling of free space electromagnetic waves (green wavy arrow) to surface plasmons, ii) the decay of the excited surface plasmons into hot electrons with energy $h\nu$ (red vertical arrow), and iii) the inelastic internal photoemission of a generated hot electron over the Schottky barrier (red horizontal arrow).

3.2. Results and Discussion

Iterative experimentation led to the development of a design depicted schematically in the accompanying image (Figure 3.2). It consists of a 10mm c-cut TiO₂ single-crystal prism as a surface plasmon polariton (SPP) coupling element and substrate for a DC-sputtered, <0001> dZnO/ZnO (~250 nm combined thickness) conductor/semiconductor layer. The top contacts are 150 nm thick thermally evaporated silver disks of 250 μm diameter, deposited, in either square or hexagonal arrays, through nickel shadow masks. The three mechanistic processes that govern the photovoltaic response of the device were studied to develop a deeper understanding of the structure-function requirements governing high efficiency hot electron extraction.

i) Plasmon coupling: Though many existing examples of plasmonic hot electron photocurrent generation utilize a nanostructured approach to excite locally resonant surface plasmons (LRSPs), the present approach uses a planar geometry to capture photocurrent from propagating SPPs (see Section 1.1). Of the principal approaches to SPP excitation that also include grating, and Kretschmann coupling, the Otto prism-coupled configuration greatly simplified the fabrication challenges associated with junction formation and device performance quantification. The choice of the Otto configuration, and thus SPP-mediated light coupling, simplifies photocurrent measurement considerations. Not only can the coupling efficiency be maximized at all measurement wavelengths below the semiconductor bandgap by simply changing the transparent conducting oxide (TCO) film thickness, but unlike LRSP excitation of nanostructured interfaces which suffer large scattering losses, SPP excitation on planar interfaces exhibit minimal scattering losses resulting in optical coupling efficiencies that can approach 100%. Since the SPP electric field intensity distribution is not complicated by 3D structure, measurement complications associated with LRSP field intensity distributions at the Schottky junction interface are eliminated (see section 2.5). In order to implement the Otto design, a single-crystal, c-axis cut, anatase TiO₂ prism with index of refraction (n) close to 2.5 was selected as a substrate to enable efficient evanescent

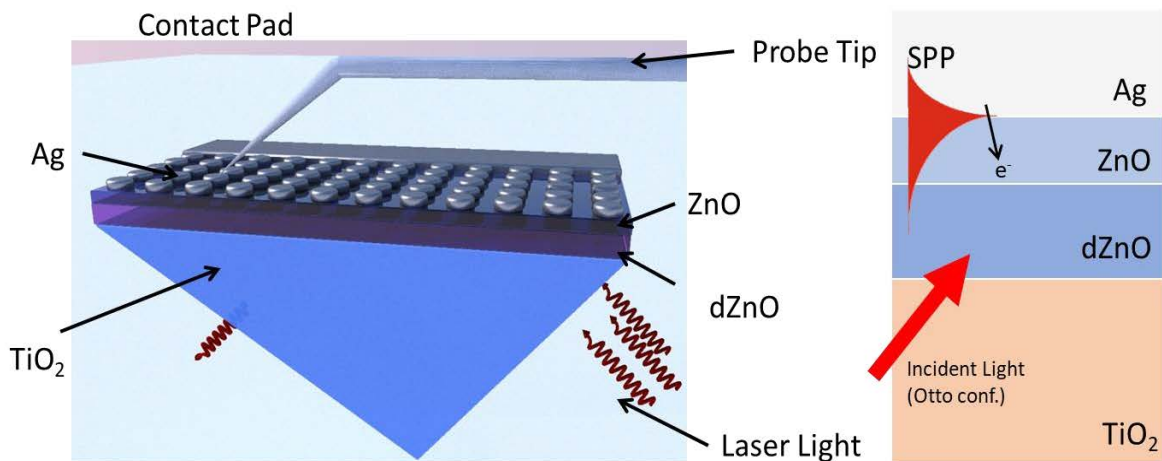


Figure 3.2. a) Otto configuration prism-coupled device enabling evanescent wave coupling of light to SPPs supported at the Ag/ZnO interface. b) Device layer schematic depicting SPP excitation, and hot electron internal photoemission across the Ag/ZnO Schottky interface

wave coupling of light to surface plasmons, across a ~250 nm ZnO/dZnO sputtered semiconductor layer ($n \sim 2$), to the SPP-active silver top contact/ZnO junction. By utilizing a TiO₂ prism and selecting a ZnO/dZnO thickness that satisfies the Otto coupling constraint¹⁰, coupling efficiencies of ~ 95% can be achieved at the wavelengths tested.

The incident angle of maximum attenuated internal reflection for samples designed for 633 nm HeNe laser light excitation was 61.8°. A survey of samples tested reveals a correlation between coupling angle and measured quantum efficiency (Figure 3.3). Of the 539 samples tested, 90% of the devices with quantum efficiencies higher than 5% are observed to couple within 0.5° of the designed coupling angle. IQE was also observed to correlate weakly (~0.2) with the degree of attenuated reflection and full width half maximum (FWHM) of the reflection minimum (see Section 2.5).¹¹

Survey of Quantum Efficiency vs Coupling Angle (N=539)

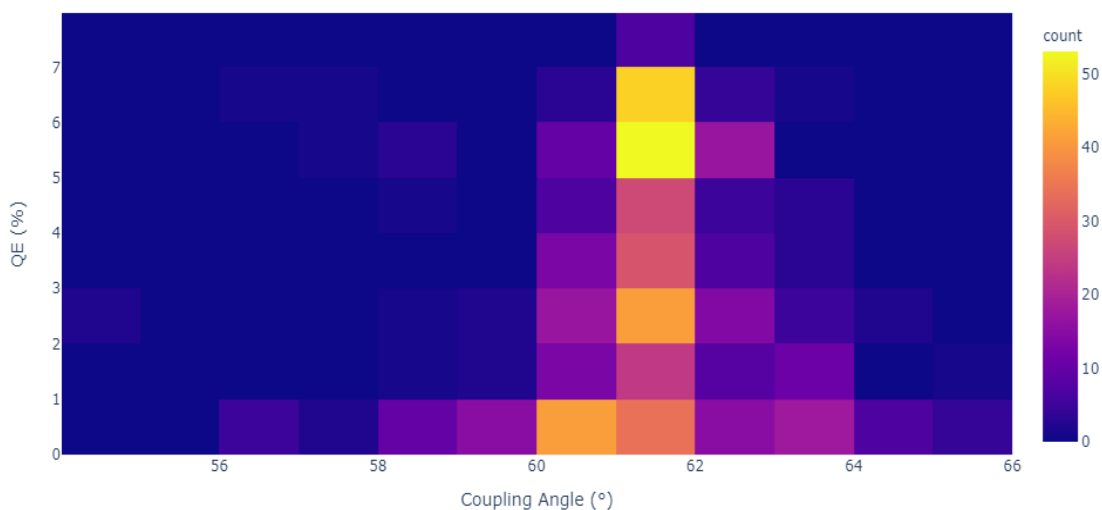


Figure 3.3. Heatmap of QE vs Coupling Angle for 539 Otto-coupled prism device samples at 633 nm excitation wavelength.

These correlations are consistent with reports that surface roughness influences the magnitude of the SPP coupling absorption minimum and its FWHM¹¹ and indicate that the quality of the device interface and its rectifying junction properties influence QE and the efficiency of SPP generation. Samples designed to couple at different wavelength for the purpose of exploring the wavelength vs QE relation were also observed to exhibit higher internal efficiency when the coupling quality and coupling angle approached the values expected from the Otto coupling equations.

ii) Hot electron generation: The decay of surface plasmon excitations to hot electrons with the energy of the incident photon has been explored experimentally and theoretically.^{8,12,13} In order to maximize current generation over the largest optical window, silver was selected as the plasmonic absorbing metal instead of gold. This selection was informed by its superior plasmonic properties, due to the lack of energy adsorbing d-d intraband transitions above 2.5eV.¹³ The influence of metal uniformity and crystallinity on hot electron lifetime is a focus of study here since previous studies on gold films indicate that less scattering of hot electron energy occurs in more uniform metal films, resulting in longer hot electron lifetimes. The silver absorbing layer was

deposited epitaxially by thermal evaporation onto the highly oriented ZnO underlayer generating a highly oriented metal film (Figure 3.4). The quality of the metal films was confirmed by characterizing the surface using scanning electron microscopy (SEM) and 2D X-ray diffraction (2D XRD). Qualitatively, the silver surface appears well oriented and large-grained through imaging, and this characterization is confirmed by the 2D XRD peaks for (111) surface normal-oriented silver, with a narrow off-normal orientation distribution (the angular width of the X-ray diffraction spot). The 2D XRD also reveals that the silver film growth is templated by the orientation of the underlying ZnO (002) surface normal (Figure 3.4-center right inset).

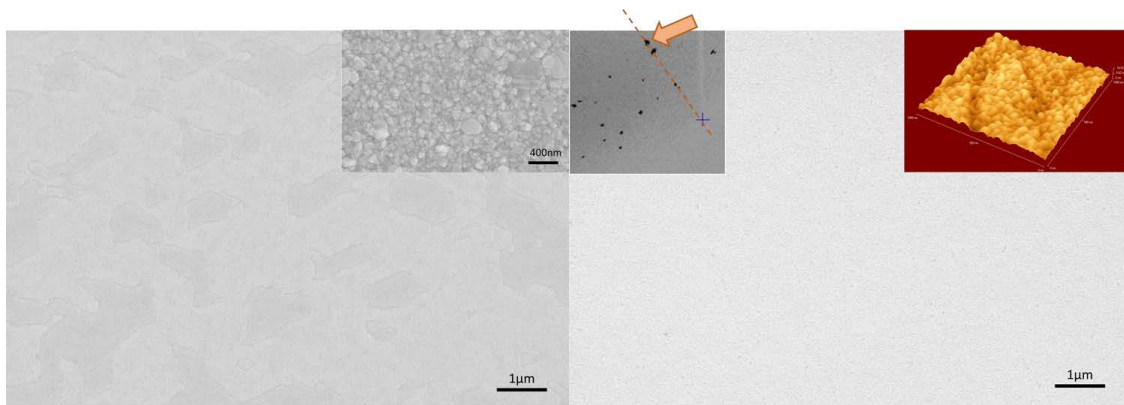


Figure 3.4. Morphology of the Ag film surface. left) SEM image of the large-grained smooth silver film on a prism sample. (inset) polycrystalline silver deposited under the same conditions on glass. right) smooth oriented ZnO prior to Ag overcoating. (inset) Atomic force microscope scan $1\ \mu\text{m} \times 1\ \mu\text{m}$ area RMS roughness = 1.3 nm, Ra = 1.0 nm. And 2D-XRD of the prism sample showing the alignment of the Ag<111> and ZnO <002> diffraction spots

iii) Internal Photoemission: Subsequent to hot electron generation, photovoltaic current results from charge separation across the Schottky interface. Plasmon decay that promotes electrons from energies close to the Fermi level of silver to unoccupied states sufficiently above the energy of the Ag/ZnO Schottky barrier can emit into the semiconductor layer where they can decay to the bottom of the ZnO conduction band. The probability of photoemission for hot electrons with energies above the barrier is governed by the momentum component of the electron in the direction normal to the rectifying interface and can be calculated according to a “cone of escape” model (see Section 1.6).⁷ The planar interface of the present device design lends itself well to the

resultant calculation of observed current vs. incident photon energy and follows a Fowler relation according to Equation 1.13.

The ultimate efficiency of the device is also heavily influenced by the electrical properties of the bulk films and of the metal/semiconductor junction. Careful iteration of fabrication processes and material choices allowed for the fabrication of high quality Schottky interfaces and resulting diodes with excellent asymmetry ($>10^5$), high forward current ($\sim 1\text{A}/\text{cm}^2$ @ 1V), and ideality factors of $n=1.1$ (Figure 3.5).

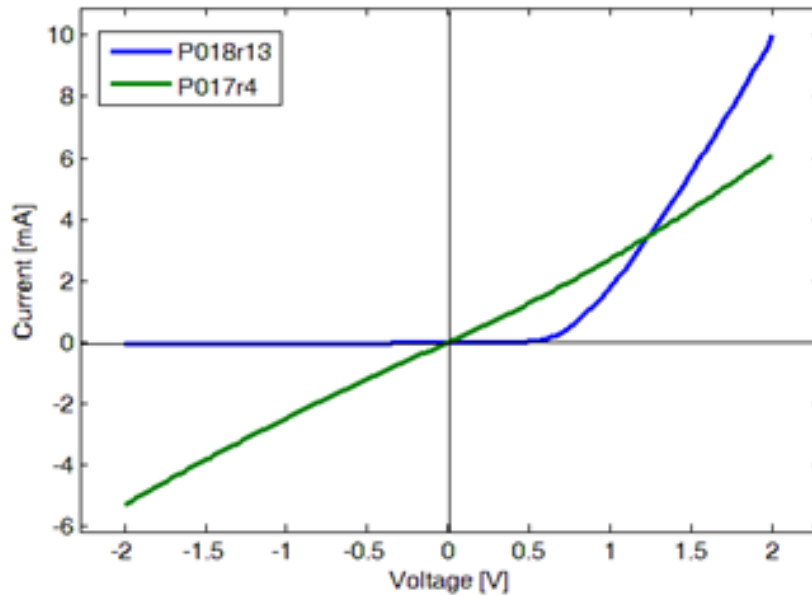


Figure 3.5. IV curve of a Ag/ZnO diode from representative prism devices The blue curve is an example of a prism sample with a Schottky junction interface (Section 1.5). The green curve was from an ohmic junction (rejected sample). See Appendix B for

The diode curves obtained for the hundreds of samples tested were numerically fitted to the data using a diode resistor circuit equation (see Section 2.4) to obtain values for barrier height (Φ_b) series resistance (R_s), shunt resistance (R_{shunt}), and diode ideality factor (n), in addition to diode asymmetry. A scatter plot of QE vs diode ideality reveals that the highest currents were achieved for diodes with ideality factors close to 1.0 (Figure 3.6).

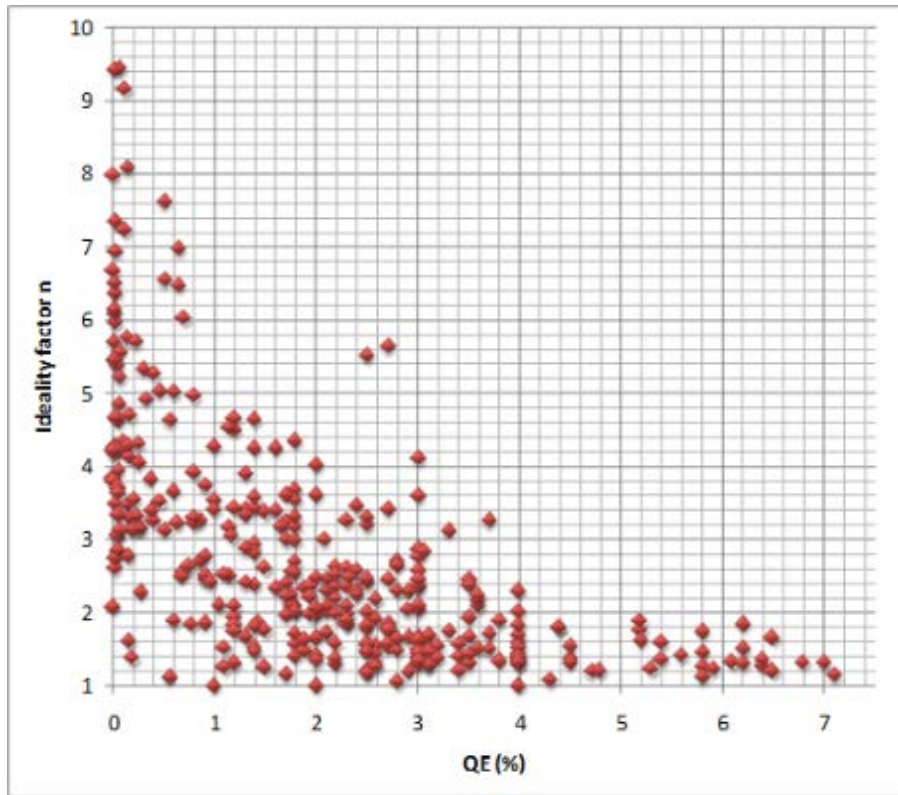


Figure 3.6. A representative sample of prism devices reveals the correlation between QE and ideality factor.

The selection of the Otto-coupled architecture greatly enhanced the device electrical properties. The templated sputter deposition of dZnO/ZnO onto single-crystal TiO₂ prism substrates resulted in a deposited film with large, oriented grains with a [002] surface normal and a columnar morphology. Subsequent silver deposition was also large-grained and highly oriented with a [111] surface normal owing to the templating effect of the underlying ZnO (see Section 2.3). 2D XRD (Figure 3.7) measurements reveal the templated orientation of the film layers, while scanning electron microscope imaging shows characteristic uniformity over large areas. (Figure 3.4). Film quality correlated well with higher device quantum efficiency, fill factors (FF), and open circuit voltage (V_{oc}) (see Section 2.5.1). This is likely due to the elimination of interface regions where surface trap-related Fermi pinning (see Section 1.3) lowers the local Schottky barrier¹⁴.

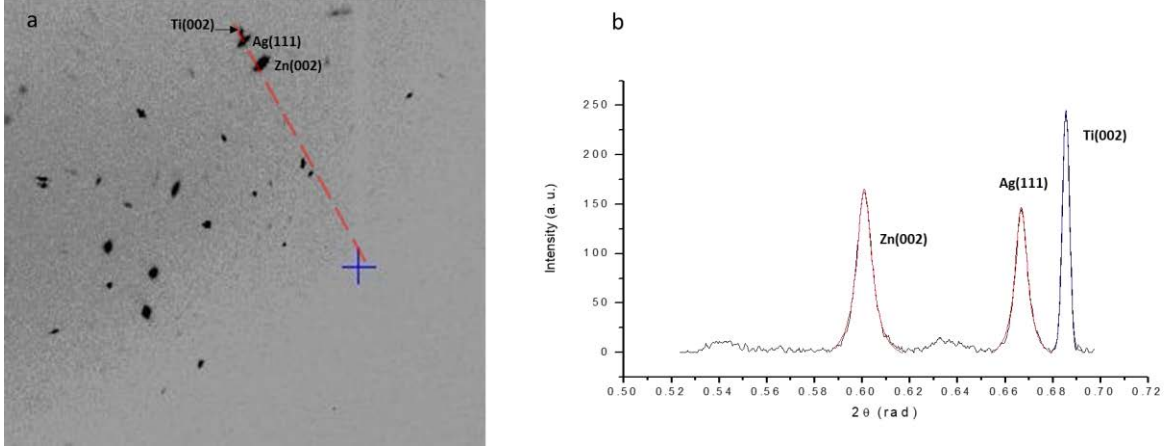


Figure 3.7. a) 2D XRD of prism sample. b) The integrated intensity along the arc *X* corresponding to the radial 2θ spacing (see Section 2.3.3). The aligned narrow spots indicate that the $\text{TiO}_2/\text{dZnO}/\text{ZnO}/\text{Ag}$ films are aligned.

The orientation of the film layers and the size of their crystalline grains were measured from 2D XRD 2θ , $\Delta\chi$ (the angle dependent distribution of XRD signal), and the FWHM of the 2θ peak. Device performance was found also to depend on the degree of crystallinity of the device layers. Because the ultimate performance of a prism device depends on multiple material layers and their crystallinity characteristics, the influence of crystallinity on device performance is depicted below with the help of a composite average of device crystallinity metric, the overall crystallinity score (OCS). The OCS for each device was calculated by first normalizing each variable and then adding them together according to Equation 3.1.

$$OCS = ZnO(002) + ZnO(101) + Ag(111) + Ag(200) + \frac{1}{ZnO(\Delta\chi)} + \frac{1}{Ag(\Delta\chi)} \quad (3.1)$$

According to Equation 3.1, the OCS comprises crystallinity information from the ZnO and Ag layers since the quality and crystallinity of the top-most silver layer is dependent on the quality and crystallinity characteristics of the underlying ZnO/dZnO layers. The maximum value of OCS is thus 6, and the dependence of QE on the OCS is shown graphically for a representative sample set in Figure 3.8.

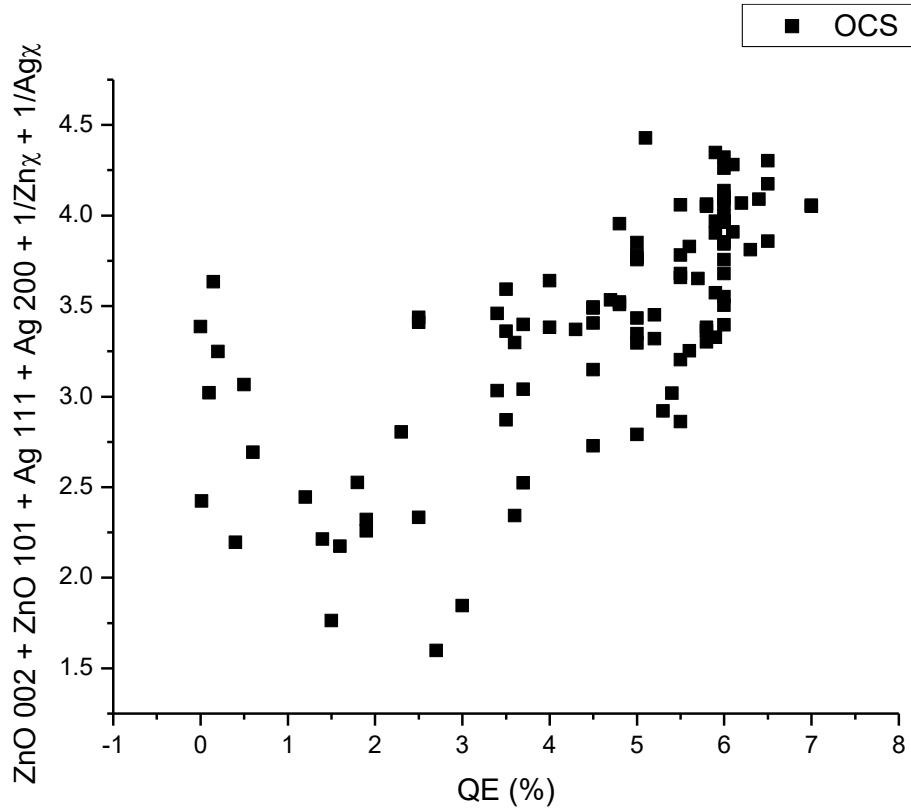


Figure 3.8. The overall crystallinity score vs quantum efficiency for a selection of prism devices measured at 633 nm.

The crystallinity and orientation of the Ag and ZnO layers are highest in samples with good quantum efficiency. The OCS is also found to influence the diode characteristics and coupling efficiency, two device properties that depend on interface smoothness, and surface traps. Large, oriented crystallites are expected to produce a smoother interface surface with fewer grain boundary defects and misaligned domains.

High quality device layers were also found to be an important factor influencing the series resistance of the measured diode curves. Series resistance was found to decrease with increasing dZnO/ZnO layer quality and low series resistance correlated well with quantum efficiency (Figure 3.9)

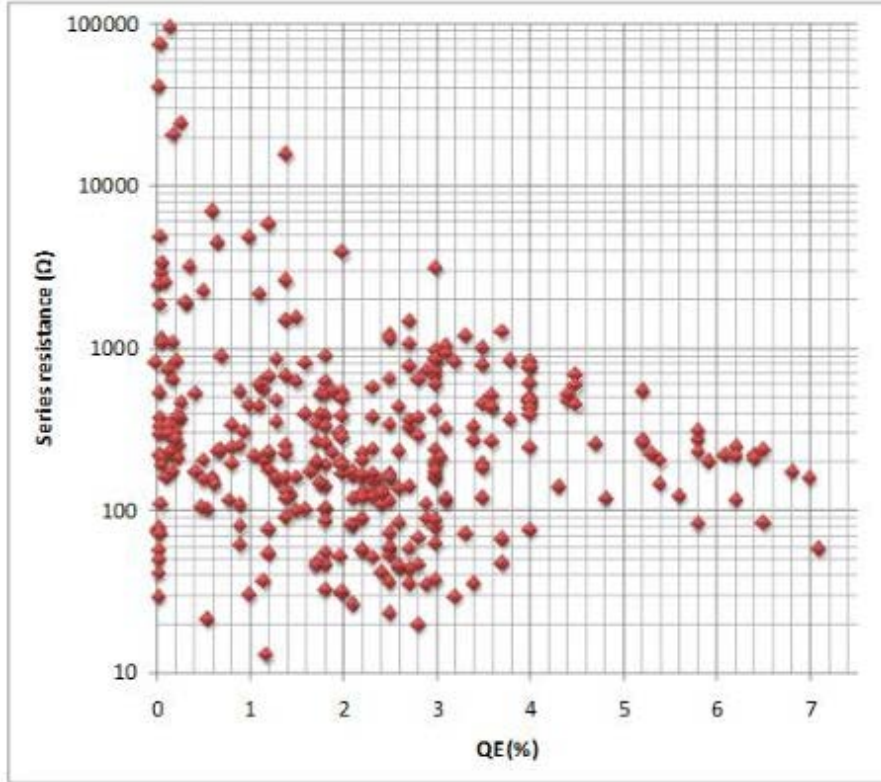


Figure 3.9. Series resistance vs quantum efficiency for a representative sample of prism device measurements.

The Schottky junction barrier height, derived from IV current measurements, was also observed to influence device quantum efficiency. The formation of the Schottky junction at ZnO/Ag contacts is a complex interfacial process that depends strongly on ZnO material quality and surface adsorbates. The Zn polar ZnO surface (determined by HCl etch¹⁵), was pretreated with an oxygen plasma etch to improve junction quality. The average barrier height for all devices tested was 0.59eV - a value at the low end of what has been generally reported for Zn polar silver Schottky junctions¹⁶. This indicates the presence of interface states which lower the barrier through Fermi level pinning¹⁴. Quantum efficiency was highest for devices with barrier heights between 0.5 and 0.6 eV (Figure 3.10), with lower efficiencies observed for devices with both lower and higher barrier height junctions.

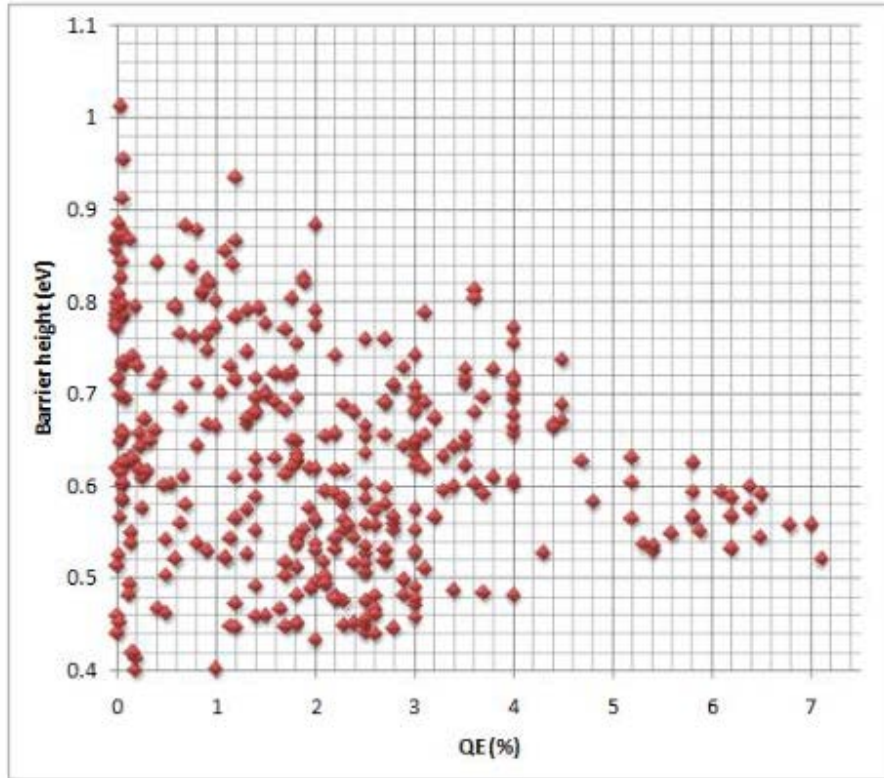


Figure 3.10. Trends in barrier height vs quantum efficiency.

Optical Characterization: Devices were characterized by monochromatic laser illumination focused to a spot size of $\sim 50 \mu\text{m}$ and calibrated to an intensity of $0.1\text{W}/\text{cm}^2$ for all wavelengths tested. The short circuit current (I_{sc}), V_{oc} , and FF were calculated from the shift in the IV curve collected in darkness upon illumination. In order to explore the dependence of the device internal quantum efficiency (IQE) on incident photon energy it was necessary to fabricate multiple samples with different dZnO/ZnO thicknesses for efficient coupling in the Otto configuration (Figure 3c). In addition, because the condition of maximum plasmonic coupling occurs at decreasing angles with incident energy, devices were built on hemispherical TiO_2 prisms to enable normal incidence on the first surface of the prism element.

The photovoltaic properties of devices were first explored through a study of open circuit voltage values. Unsurprisingly, V_{oc} was found to depend linearly on barrier height (Figure 4.11). IV curves under illumination generally exhibited irregular shapes and meaningful analysis of how the diode properties changed under illumination was difficult. Though the V_{oc} was observed to be approximately 0.5eV below the barrier

height and illuminating ZnO Schottky junctions at energies above the bandgap has been shown to result in a lowering of the forward bias barrier¹⁸, the Fowler behaviour of the sample set discussed below suggests that the junction barrier to internal photoemission is not substantially reduced. Electrons injected into the depletion region may recombine with near surface positive holes and tunnel back to the silver through a mechanism analogous to those observed for Schottky junctions with interface contamination due to surface states¹⁴, a process known as junction pinning, resulting in a low open circuit voltage.

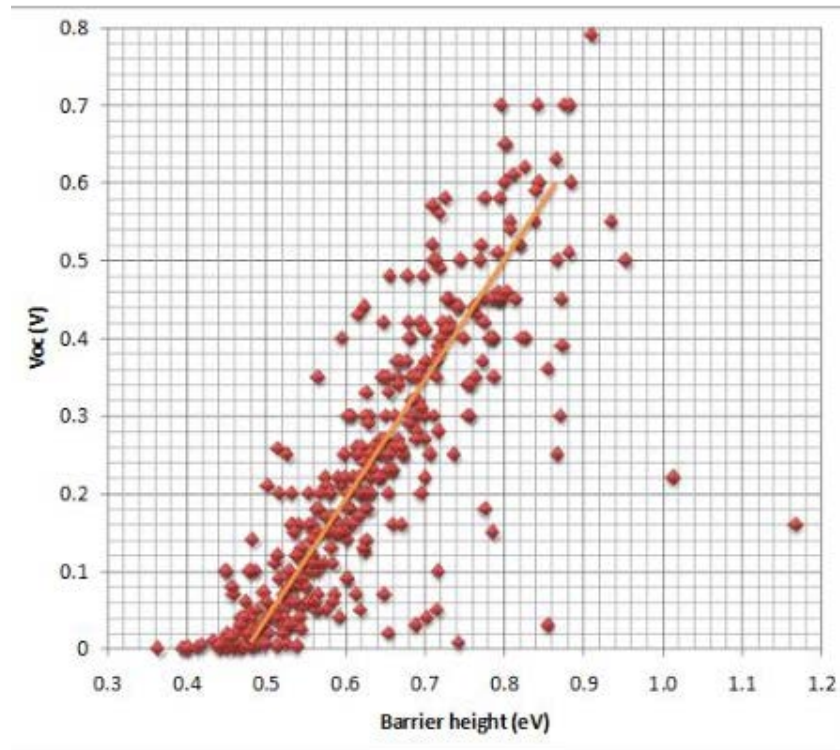


Figure 3.11. V_{oc} dependence on barrier height.

Fill factors (FF) were calculated from 255 prism devices (mean FF 38%), the top quartile of which exhibited fill factors above 44%. The best device had a fill factor of 67%. The observed fill factors are lower than for indirect band gap semiconductor photovoltaics such as silicon, which are well known to be ~80%, but compare well to other reported measurements of plasmonic photovoltaics¹⁷. A weak correlation between V_{oc} and FF can be observed from Figure 3.12, indicating that junction quality as well as

resistive losses and recombination within the bulk of the ZnO/dZnO film are contributors to the observed fill factor values.

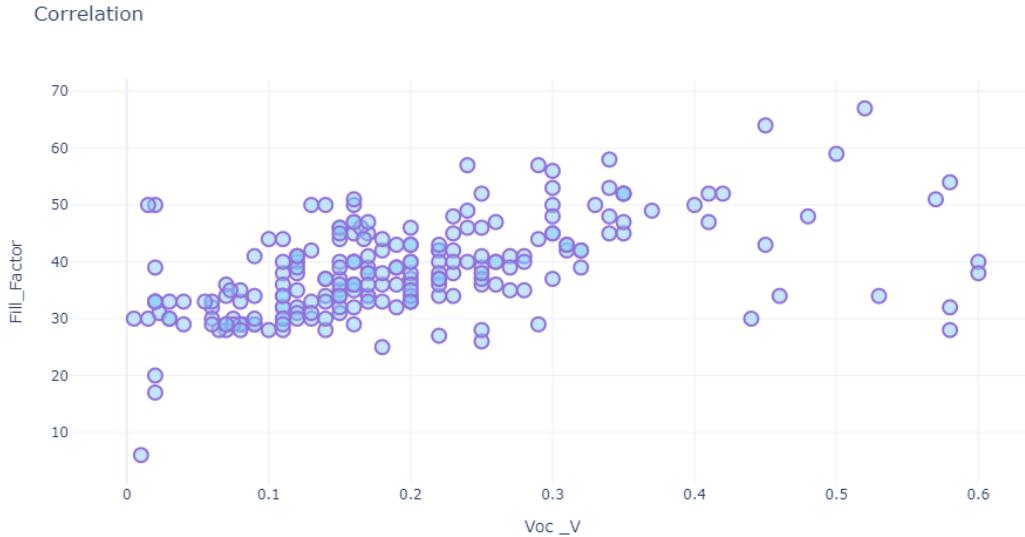


Figure 3.12. Fill factor versus open circuit voltage.

Further analysis of samples designed to couple light to SPPs at different incident energies reveals a wavelength dependent internal quantum efficiency that is consistent with the internal photoemission mechanism and gives rise to an excellent Fowler relation (Figure 3.13). Fowler analysis (see Section 1.4) yields a logarithmic plot with a zero current intercept of 0.5 eV. This value, in reasonable quantitative agreement with the average barrier height of 0.59eV observed during I-V device characterization, is consistent with the proposed mechanism of photovoltaic charge separation, and indicates that, despite low observed V_{oc} values, the Schottky barrier is not lowered greatly upon illumination. This observation is consistent with the conjecture that charges that surmount the barrier can be shunted back across the Schottky interface via tunneling through near surface defects. This is akin to the well-known pinning mechanism observed for Ohmic and low-quality Ag/ZnO junctions, despite the existence of an interface barrier. The highest observed QE was 11.2% at 543 nm incident photon wavelength, the highest photon energy investigated through this study.

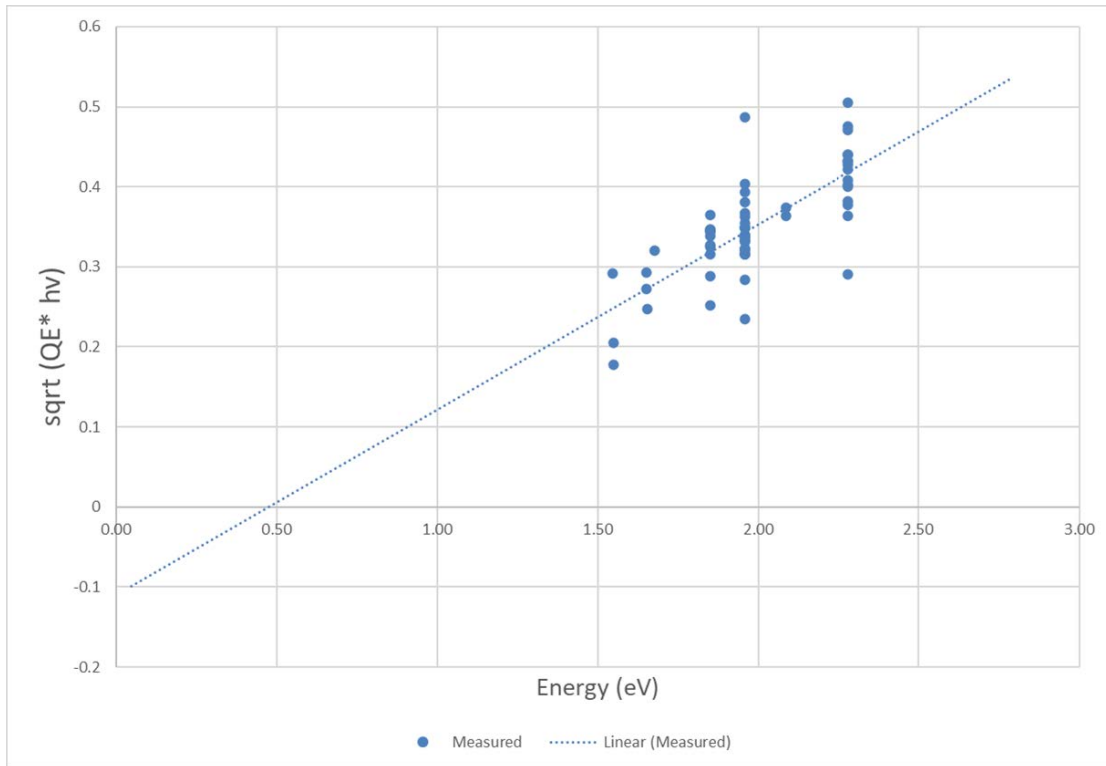


Figure 3.13. Fowler plot of device response vs incident photon energy.

The calculated PCE of the sample set was surveyed. Counterintuitively the highest values were not observed for the highest QE devices as a result of the previously discussed $\sim 0.5V$ offset of V_{oc} to Schottky barrier height (Figure 4.11). The maximum PCE was obtained for a prism device at 633 nm incident wavelength, a barrier height of 0.73eV, a V_{oc} of 0.44V, a FF of 30%, and a coupling efficiency of 90%. The resultant PCE was 2.9%.

3.3. Summary

The systematic study of hundreds of prism-coupled devices that were fabricated and characterized allowed the identification of statistical trends in the collected data. The different electrical and material properties measured were observed to influence QE to varying degrees. This, and the large number of variables governing the ultimate performance of the devices, makes definitive quantification of structure-function relationships difficult. Nevertheless, the wealth of data available from these studies allows the identification of strong qualitative trends that serve as a valuable guide to

inform the design of high efficiency plasmonic hot electron devices. Although the electrical, optical and material properties, such as diode ideality factor (n), series resistance, Schottky barrier height, coupling angle and reflection minima were all found to correlate well with device performance and are inherently all inter-related, perhaps the most critical correlations to device performance can be attributed to the crystalline and oriented nature of the materials that define the interface. A high degree of crystallinity and orientation of the silver, dZnO and ZnO layers were necessary conditions to establish the required electrical and optical characteristics to enable efficient hot electron extraction. Thus, the design of high-quality rectifying plasmonic structures will benefit from oriented, single-crystal materials and strategies that minimize interface traps and defect states that mitigate efficient charge separation in these novel structures.

Though the application of plasmonically mediated hot electron emission to photovoltaic energy generation suffers from fundamental physical constraints that limit its commercial utility, it is anticipated that the data presented here will aid in the design of efficient hot electron devices that enable novel catalytic, sensing, and electrochemical applications.

References

- 1 Clavero, C., 2014. Plasmon-induced hot-electron generation at nanoparticle/metal-oxide interfaces for photovoltaic and photocatalytic devices. *Nature Photonics*, 8(2), pp.95-103.
- 2 Brongersma, M.L., Halas, N.J. and Nordlander, P., 2015. Plasmon-induced hot carrier science and technology. *Nature nanotechnology*, 10(1), pp.25-34.
- 3 Christopher, P. and Moskovits, M., 2017. Hot charge carrier transmission from plasmonic nanostructures. *Annual review of physical chemistry*, 68, pp.379-398.
- 4 Feng, B., Zhu, J., Lu, B., Liu, F., Zhou, L. and Chen, Y., 2019. Achieving Infrared detection by all-Si plasmonic hot-electron detectors with high detectivity. *ACS nano*, 13(7), pp.8433-8441.
- 5 Dahlin, A.B., Dielacher, B., Rajendran, P., Sugihara, K., Sannomiya, T., Zenobi-Wong, M. and Vörös, J., 2012. Electrochemical plasmonic sensors. *Analytical and bioanalytical chemistry*, 402(5), pp.1773-1784.
- 6 Manuel, A.P. and Shankar, K., 2021. Hot Electrons in TiO₂–Noble Metal Nano-Heterojunctions: Fundamental Science and Applications in Photocatalysis. *Nanomaterials*, 11(5), p.1249.
- 7 Scales, C. and Berini, P., 2010. Thin-film Schottky barrier photodetector models. *IEEE Journal of quantum electronics*, 46(5), pp.633-643.
- 8 White, T.P. and Catchpole, K.R., 2012. Plasmon-enhanced internal photoemission for photovoltaics: theoretical efficiency limits. *Applied Physics Letters*, 101(7), p.073905.
- 9 Tagliabue, G., Jermyn, A.S., Sundararaman, R., Welch, A.J., DuChene, J.S., Pala, R., Davoyan, A.R., Narang, P. and Atwater, H.A., 2018. Quantifying the role of surface plasmon excitation and hot carrier transport in plasmonic devices. *Nature communications*, 9(1), pp.1-8.
- 10 Otto, A., 1968. Excitation of nonradiative surface plasma waves in silver by the method of frustrated total reflection. *Zeitschrift für Physik A Hadrons and nuclei*, 216(4), pp.398-410.
- 11 Grajower, M., Levy, U. and Khurgin, J.B., 2018. The role of surface roughness in plasmonic-assisted internal photoemission schottky photodetectors. *Acs Photonics*, 5(10), pp.4030-4036.
- 12 Sundararaman, R., Narang, P., Jermyn, A.S., Goddard III, W.A. and Atwater, H.A., 2014. Theoretical predictions for hot-carrier generation from surface plasmon decay. *Nature communications*, 5(1), pp.1-8.

- 13 Narang, P., Sundararaman, R. and Atwater, H.A., 2016. Plasmonic hot carrier dynamics in solid-state and chemical systems for energy conversion. *Nanophotonics*, 5(1), pp.96-111.
- 14 Brillson, L.J. and Lu, Y., 2011. ZnO Schottky barriers and Ohmic contacts. *Journal of Applied Physics*, 109(12), p.8.
- 15 Özgür, Ü., Alivov, Y.I., Liu, C., Teke, A., Reshchikov, M., Doğan, S., Avrutin, V.C.S.J., Cho, S.J. and Morkoç, A.H., 2005. A comprehensive review of ZnO materials and devices. *Journal of applied physics*, 98(4), p.11.
- 16 Janotti, A. and Van de Walle, C.G., 2009. Fundamentals of zinc oxide as a semiconductor. *Reports on progress in physics*, 72(12), p.126501.
- 17 Mubeen, S., Lee, J., Lee, W.R., Singh, N., Stucky, G.D. and Moskovits, M., 2014. On the plasmonic photovoltaic. *ACS nano*, 8(6), pp.6066-6073.
- 18 Zhu, R., Zhang, X., Zhao, J., Li, R. and Zhang, W., 2015. Influence of illumination intensity on the electrical characteristics and photoresponsivity of the Ag/ZnO Schottky diodes. *Journal of Alloys and Compounds*, 631, pp.125-128.

Chapter 4.

Epitaxial Silver Plasmonic Arrays on Silicon by Nanostencil Lithography*

4.1. Introduction

As presented in Chapters 1 and 3, surface plasmons (SPs) are photon-electron excitations confined to the interfaces of metal and dielectric materials. SPs offer the opportunity to concentrate the extended three-dimensional fields of propagating electromagnetic waves to the nanometer scale of conductive particles, and textured plasmonic interfaces, resulting in field enhancements that scale with the extent of localization. These confined fields have the potential to affect new physical and chemical processes and have been the focus of intensive research efforts.¹⁻⁵ One of the primary challenges in this research is to fabricate well-defined crystalline metal surfaces with controlled nanostructure, and limited material imperfection, designed to tailor these plasmonic fields and maximally enhance their magnitude. Here, a straightforward, low-cost method to pattern large area arrays of monocrystalline, faceted silver nanopillars is presented. In this two-step additive patterning process, Ag is evaporated onto high temperature Si(100) to yield epitaxial crystalline Ag(100) films. Subsequent low temperature Ag nanostencil lithography affords large area nanopillar arrays comprised of faceted, epitaxial, monocrystalline Ag pillars. The utility of this approach is demonstrated by plasmonic field confinement of the Ag nanopillar array and its ability to enhance the nonlinear optical response of ZnO overlayers, as revealed by pillar-resolved second harmonic generation imaging.

Single-crystal materials are used extensively in optics, materials engineering, semiconductor device manufacturing, high performance electrical applications, and scientific research, due to their large area uniformity and superior performance metrics

* The author had a major contribution to the design and fabrication of nanostructured samples (along with Dr. Jayna Chan, Steven Gou, and Greg Wong), TEM characterization (along with Dr. Xin Zhang), and SHG experiments (along with Dr. Saeid Kamal), as well as the design and analysis of experiments (all team members; see acknowledgements). The author had a minor contribution to the SEM imaging and XRD measurements (along with Dr. Xin Zhang and Dr. Enrico Bovero). The majority of the development of the silver deposition process was developed as part of a commercially-funded research project.

associated with the absence of grain boundaries and scattering losses that typify polycrystalline materials. They form ideal substrates for the study of electrical junctions,^[6] electrochemical growth,⁷ and lithographic patterning, as evidenced by the ubiquity of single-crystal silicon substrates in microelectronics and modern fabrication techniques.⁸ Single-crystal and ultrasmooth gold substrates are widely used for the study of electrodeposition^[9] and plasmonics.¹⁰⁻¹² The application of highly regular silver nanostructures and smooth silver films to plasmonics is also of increasing interest.^[13] Silver shows low optical losses at optical frequencies¹⁴ and, unlike gold, is low cost and lacks an absorbing interband transition, making it a preferred plasmonic material for use in the visible spectral region.¹⁵ The deposition of highly oriented, smooth silver films and well-defined nanostructures, without the use of complex techniques and instrumentation, such as molecular beam epitaxy (MBE)¹⁶ and focused ion-beam (FIB) milling^[17] presents an opportunity for wider application of silver in plasmonic device manufacture and research. Single-crystal silver surfaces and nanostructures promise high performance metamaterials¹⁸⁻²⁰ for negative refraction²¹⁻²³ and diffraction-free propagation of surface plasmon polaritons.¹⁴⁻²⁶ Single-crystal metals minimize optical losses and SPP damping originating from grain boundaries and surface roughness^{12,27}, and are expected to demonstrate improved mechanical and thermal stability of nanostructures, provide enhanced localized surface plasmon resonant (LSPR) field intensity of faceted nanostructured elements, and generate enhanced plasmonic coupling between high definition nanoscale features.

Thermal and e-beam evaporation of single-crystal silver films has been studied experimentally on mica and sapphire substrates at elevated temperatures,²⁸⁻²⁹ yielding single-crystal films with the Ag[111] axis oriented normal to the substrate surface. Single-crystal Ag(111) films, deposited by e-beam evaporation onto mica at temperatures above 300°C, are easily patterned by a variety of nanolithographic techniques.³⁰ More recently, e-beam evaporated Ag on Si(100) followed by rapid thermal annealing was shown to yield high quality Ag(100) films³¹, films deposited by this technique have been improved through the pre-deposition of Ag islands at 350°C prior to low temperature continuous film deposition, and 500°C annealing of rough epitaxial films to achieve ultra-smooth surface quality.⁴²⁻⁴³ In addition, sputter-deposited, single-crystal silver films on Si(111) substrates have been patterned by electron beam lithography and plasma etching to yield visible frequency hyperbolic metasurfaces which display the

characteristic properties of metamaterials with device performance greatly exceeding previous demonstrations with polycrystalline silver films.³²

While single-crystal and nanostructured metal films are a powerful tool in surface science, plasmonics, and nanophotonics, their broader utility and application in device architectures is typically limited by expensive and time-consuming fabrication methods. Here, we present a simple method for the deposition of smooth, single-crystal, epitaxial Ag(100) films, 300 nm thick, on hydrogen terminated Si(100), by high temperature thermal evaporation. On the surface of these high quality Ag(100) films, a wide area array of highly regular 100 nm tall Ag nanopillars are fabricated by homoepitaxy-mediated nanostencil lithography. The pillars display faceted sidewalls and flat tops consistent with the deposition of oriented crystalline pillars, demonstrating that the additive manufacture of crystalline Ag nanopillar arrays is a new and powerful approach to the production of high quality plasmonic nanostructured surfaces.

4.2. Results and Discussion

Early studies of silver deposition on silicon substrates conducted under ultrahigh vacuum (UHV) conditions using silicon substrates prepared by high temperature desorption of the substrate native oxide layer,³² or by HF cleaning to generate a hydrogen terminated silicon (H-Si) surface³³ focused on the initial stages of nucleation and film growth. They revealed that silver films on Si(100) and Si(111) at elevated temperatures grow by island formation upon a thin planar layer, by the Stranski-Krastanov (S-K) growth mode and that Ag deposition onto H-terminated Si(111) grows epitaxially. Also of interest, is the early observation by Hanawa *et al.*,³⁴ that the epitaxial growth of silver on silicon is not hindered by an interface silicide. In contrast, the formation of gold silicide at elevated temperatures complicates both epitaxial Au growth, and interface chemistry, for that material combination.

High temperature MBE growth studies revealed that Ag island growth on oxide-free Si(100) is dominated by two distinct temperature dependent morphologies: “small island” and “big island” morphologies.¹⁶ Small islands appear to be disorganised granules, a few tens of nanometers in size, which result from the precipitation of Ag as samples cool. At temperatures above 300°C for films thicker than 0.8 monolayers, the authors observed the formation of a large island morphology, in addition to the small

islands. The large islands were observed to be well faceted and aligned in the Ag[100]//Si[100] direction.

Guided by these insights, we investigated the morphology of silver films grown by thermal evaporation on H-Si(100) and H-Si(111). Based on scanning electron microscopy (SEM), transmission electron microscopy (TEM) and X-ray diffraction (XRD) studies, we report the epitaxial growth of silver films on surface buffered oxide etched (BOE) Si(100) and Si(111) substrates by thermal evaporation at elevated temperatures. Smooth continuous films were obtained at thicknesses of 300 nm and above on Si(100) substrates. Thinner films exhibit characteristic large islands, well oriented with respect to the underlying substrate. We further explored the utility of these smooth continuous films on Si(100) by depositing a nanostructured over-layer of Ag, formed through evaporation at low temperature, through a nanostencil mask. The resultant Ag pillars are well faceted and smooth in comparison with pillars deposited directly on silicon under the same conditions.

Our study shows that the morphology of silver films deposited on silicon depends strongly on the growth temperature, the crystal orientation of the substrate, and the presence or absence of the native surface oxide layer. Other deposition variables, such as the chamber pressure (1×10^{-7} Torr to 3×10^{-6} Torr) and the deposition rate (0.2 \AA s^{-1} to 6 \AA s^{-1}), were found to have relatively little effect on the resultant silver films, within the ranges tested. The results of these experiments are described in Section 4.4 (Figure 4.6). These studies demonstrate that the 350 °C deposition of Ag onto Si:H(100) leads to continuous single-crystal epitaxial Ag(100) films. A series of high temperature Ag deposition experiments on oxide etched Si(100) were conducted to investigate the dependence of film morphology on thickness. Oxide etched Si(111) substrates were also investigated in a similar manner. From the SEM images presented in Figure 4.1, some important features of the film growth mechanism can be inferred. At low thickness (e.g. 20 nm by quartz crystal monitoring (QCM) in Figure 4.1a), films are composed of discontinuous islands. The islands appear to be well faceted and grow with pyramidal morphologies (Figure 4.1b: 30 nm by QCM). Though some small grains are visible in the image, the vast majority of the deposit consists of islands 50-100 nm wide and 50-80 nm tall, dispersed with good uniformity over the surface of the substrate. The sidewalls of the island facets were observed to be inclined between 45° and 58° relative to the Si(100) surface. At film thicknesses of 75 nm (Figure 4.1c) the uniform island

morphology disappears as small islands are observed to coalesce and thicken, forming faceted islands with truncated edges, approximately 200 to 400 nm across. Large islands are either separated by regions containing thinner smaller islands and even smaller silver crystallites (that are less prevalent in lower thickness deposits), or by narrow clear regions where the large island facets are in close proximity. The islands are observed to be distorted truncated octagonal pyramids, influenced by their proximity to neighboring structures. However, the islands clearly display flat tops and well-defined angled sidewalls consistent with (110) (45°) and (111) (54.8°) facets expected for a truncated octagon with a (100) top surface (Figure 4.7 and 4.8). At greater thickness, the island morphology is seen to give way to a continuous surface with small pin-hole defects and surface roughness with a faceted appearance, indicative of large islands of differing height coalescing. Finally, at thickness greater than 300 nm (Figure 4.1d), a smooth continuous silver film can be obtained with no visible grain boundaries.

Thickness-dependent morphology studies of Ag deposited on H-Si(111) substrates reveal a similar growth progression from small to large crystallites, but the transition in growth morphology begins at a lower deposited thickness i.e. 30 nm (Figure 4.1e). Ag films grown on H-Si(111) substrates have truncated hexagonal island morphologies at low thickness, consistent with the symmetry of the underlying surface. At greater thickness, up to 500 nm in the present study (Figure 4.1f), the morphology of the silver films on Si(111) are not observed to coalesce into a smooth, grain boundary-free layer. Instead, pinholes remain and the boundaries between Ag crystallites lose their triangular and hexagonal shapes but remain visible.

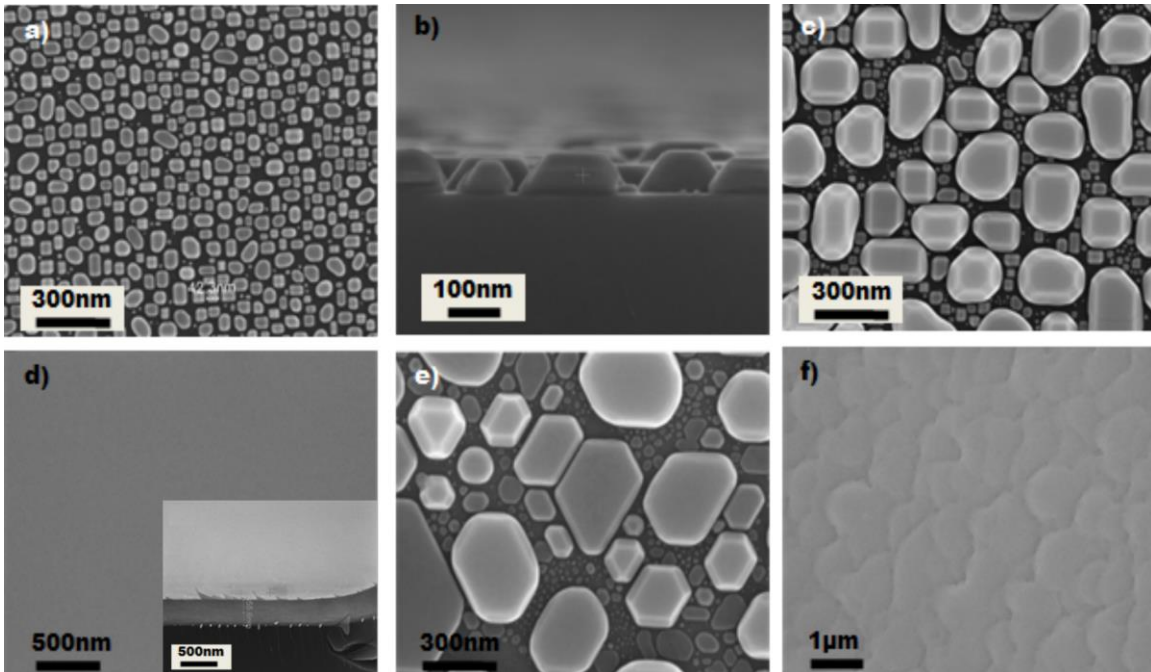


Figure 4.1 SEM investigation of the evolution of silver growth from isolated epitaxial islands to continuous films by high temp. thermal evaporation. a) - d) show H-Si terminated Si(100) surface mediated Ag film growth at thicknesses of a) 20 nm, b) 30 nm (cross section, tilt view), c) 75 nm, and d) 300 nm (inset: cross section, tilt view). Panels e) and f) are images of H-Si terminated Si(111) surface mediated Ag film growth at e) 30 nm and f) 500 nm.

The degree of crystallinity and orientation of high temperature deposited Ag films on H-terminated silicon surfaces was measured by 2D XRD and compared with the XRD patterns of films deposited at 55 °C. The diffraction images are presented in Figure 4.2. The dashed red lines in each panel show the direction of the substrate surface normal with respect to the observed 2D diffraction pattern. The patterns in Figure 4.2a and 4.2b clearly show that low temperature silver films deposited on Si(100) are polycrystalline and poorly oriented with respect to the surface of the substrate. This is to be expected based on the SEM images presented in Figure 4.6 for low temperature silver deposition. The polycrystalline radial diffraction arcs reveal a difference in the morphology of the two films not observed by SEM.

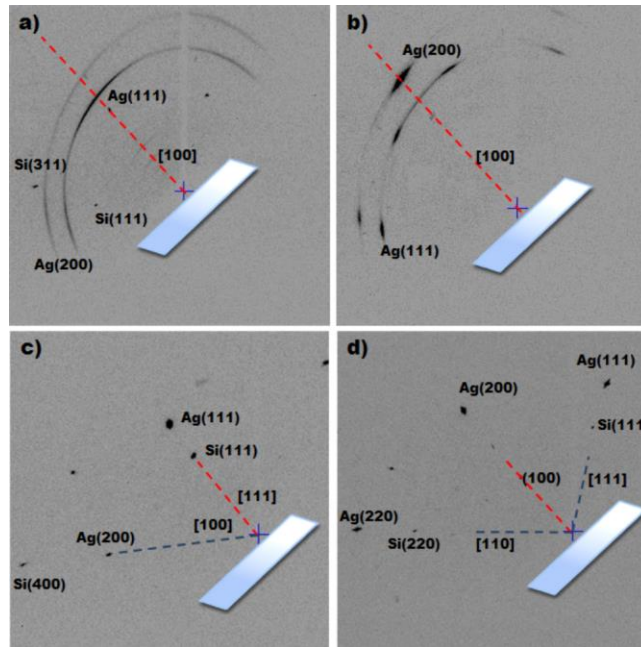


Figure 4.2. 2D XRD patterns of Ag films grown on Si substrates. The dashed red lines show the sample surface normal and the blue lines show directions of constant χ angle corresponding to a given lattice plane orientation (see section 2.4). All films tested were 300 nm thick a) Low temp. Ag (see 2.1.1) on native oxide coated Si (100) b) Low temp. Ag on H-Si terminated Si(100) c) High temp Ag. on a H-Si terminated Si(111) d) High temp Ag. on a H-Si terminated Si(100).

The low temperature silver film deposited on native oxide terminated Si(100) substrate shows a preferential Ag[111] orientation to the substrate surface, as represented by the darker region of the $38^\circ 2\theta$ arc intersected by the dashed red line in Figure 2a. This preference for the Ag[111] orientation is typical for polycrystalline face centred cubic (FCC) films. Figure 4.2b depicts the 2D XRD pattern of a low temperature silver film deposited on H-Si terminated Si(100) substrate. Interestingly, the dark spot, aligned with the substrate surface normal along the $44.5^\circ 2\theta$ arc from the Ag(200) diffraction, reveals that the polycrystalline film is preferentially oriented with the majority of its crystallites having Ag(100) planes oriented near parallel to the Si(100). The XRD patterns of high temperature Ag films grown on H-Si terminated substrates offer stark contrast to the low temperature case, revealing epitaxial alignment of Ag to Si for both the Si(111), Figure 4.2c, and Si(100) substrates, Figure 4.2d. From the dashed blue and red lines superimposed on the XRD images of both samples, it is apparent that the films

demonstrate Ag(111)//Si(111) and Ag(100)//Si(100) epitaxial growth, consistent with domain matching epitaxial models for Ag and Si.^[35-36]

The smooth epitaxial films that result from high temperature deposition of Ag on H-terminated Si(100) substrates were investigated for their utility as a surface template for the over-growth of silver nanostructures. Using a nanostencil shadow mask technique,^[37] silver pillars were deposited on 3 different substrates: a 150 nm thick polycrystalline Ag film (Figure 4.3a), a Si(100) substrate with a native oxide surface (Figure 4.3b), and a 300 nm thick Ag(100) film, deposited at 350 °C on a Si(100) wafer with a H-Si terminated surface (Figure 4.3c and 4.3d). Figure 4.3a and 4.3b show polycrystalline Ag deposits, as would be expected from the preceding discussion. The features are not shadow masked with high fidelity, presumably because non-uniform nucleation of silver crystallites and consequent complex growth kinetics distort the shape of the resultant pillar. Figure 4.3b, nanostenciled Ag on native oxide-coated Si(100), captures two other interesting features. A ring of disconnected irregular islands with sizes on the order of 10 to 20 nm are observed around each silver pillar of irregular shape, possibly related to the shadow mask penumbra.^[37] Silver deposits can also be seen in the form of ~10 nm particles sparsely distributed across the substrate surface in regions that were completely covered by the shadow mask and well outside the penumbra region. The particles are similar in size and distribution to those observed in MBE experiments on Si(100) surfaces,^[16] suggesting precipitation of silver from a thin S-K type planar layer which grows laterally across the covered region. Figure 4.3c and 4.3d depict the results of nanostenciled pillars deposited at low temperature (55 °C) on smooth single-crystal Ag films grown on H-Si(100) substrates. The pillars are without observable grain boundaries, exhibiting a flat top morphology, smooth faceted sidewalls and good uniformity (Figure 4.8 and 4.9). 2D-XRD studies show no change in the diffraction pattern of the epitaxial Ag(100) films following nanopillar deposition. A model of the deposited nanopillars consistent with our observations is presented in Figure 4.3e. The faceted octagonal nanopillars observed in Figure 4.3d can be understood in terms of the epitaxial deposition through the 450 nm diameter circular apertures of the nanostencil. The facets represent the {111} and {110} family of planes of the growing crystalline pillars. The top surface of the nanopillar is the (100) surface, as expected for epitaxial deposition on Ag(100). Note that the appearance of the facets, the observed degree of truncation of the octagonal pillars, and the definition of the pillar top surface

are expected to be determined by the extent of deposition (pillar height) and the relative rates of nucleation and growth on the different Ag facets. The details of the pillar growth and resulting pillar shapes were found to be dependent on the deposition conditions and the cleanliness of the nanostencil mask (Figure 4.9). Well-faceted regular octagonal pillars require use of pristine nanostencils or ones suitably recovered from previous deposition through nitric acid cleaning, however, pillar faceting remains prevalent despite poor mask quality (Figure 4.10), indicating the strong preference for epitaxial deposition on these substrates.

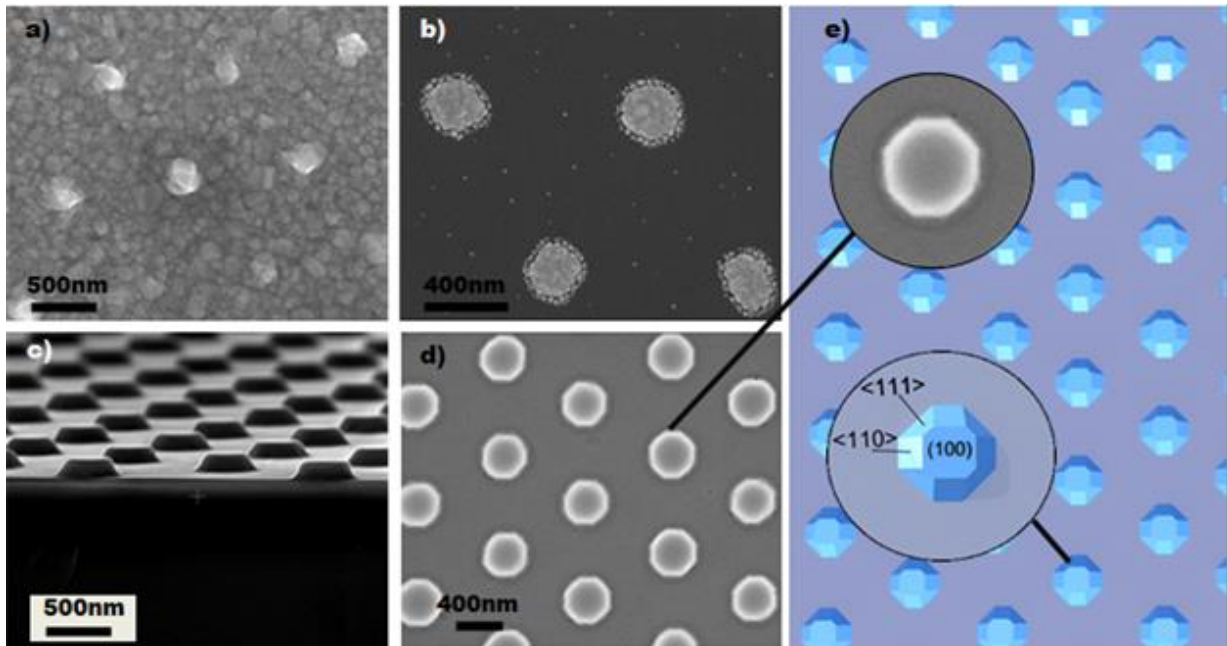


Figure 4.3. Low temperature nanostenciled pillars a) 100 nm on polycrystalline Ag. b) 20 nm of Ag on a native oxide terminated Si(100) c) 100 nm of Ag on a 300 nm high temperature deposited Ag(100)//Si(100) planar film (cross section, tilt view), d) top view image of c) showing faceted nanopillars, e) schematic of epitaxial faceted crystalline silver nanopillar arrays.

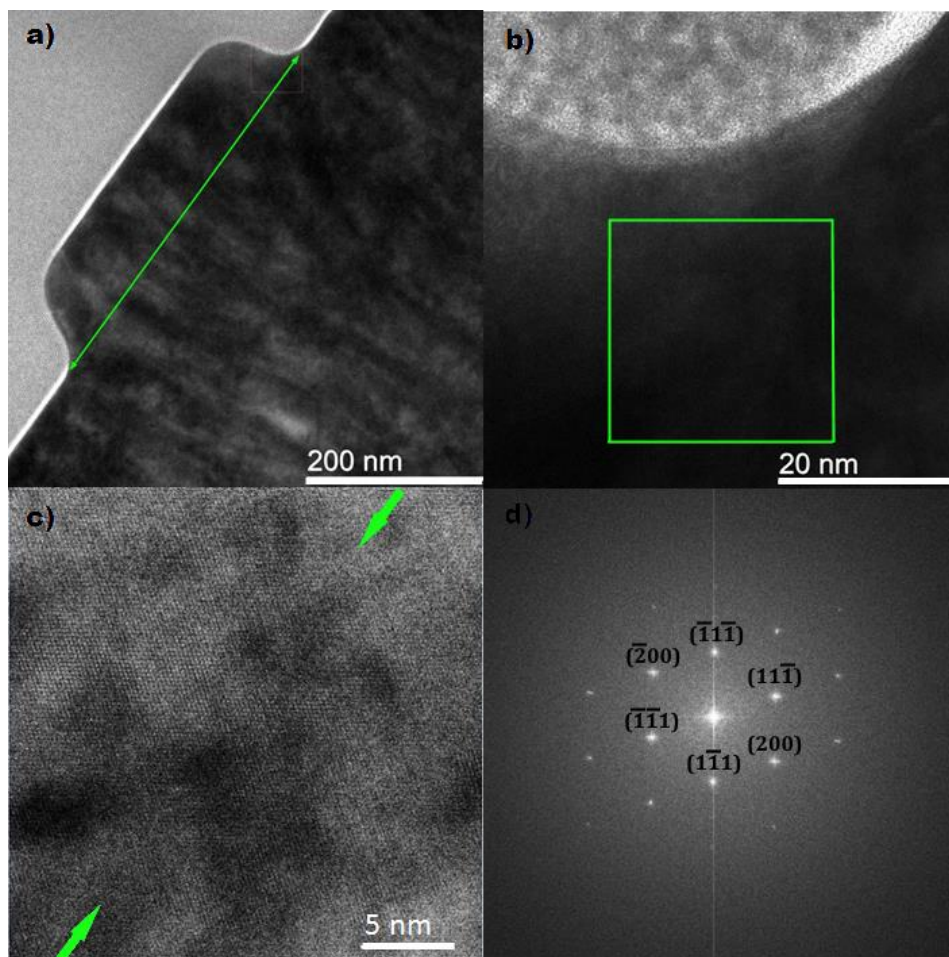


Figure 4.4. High resolution transmission electron microscopy of nanostenciled Ag pillars. a) Cross section of a nanopillar with the Ag(100)/pillar interface indicated by the green double headed arrow. b) Expanded view of the Ag(100)/pillar interface near the nanopillar edge. c) High resolution image of the interface region indicated by the green box in b). The green arrows indicate the location of the interface and demonstrate epitaxial deposition of the Ag nanopillar with a low defect density interface. d) indexed fast Fourier transform of the image in c).

The quality and crystallinity of the nanostencil-deposited Ag pillars was further investigated through high resolution transmission electron microscopy (HR-TEM). Figure 4.4 shows the HR-TEM results from the Ag(100)/Ag nanopillar interface region. Figure 4.4a shows a cross sectional TEM image of an individual nanopillar with the Ag(100)/pillar interface indicated by a green double headed arrow. A high resolution image of the pillar interface region near the nanopillar edge (Figure 4.4b) is presented in Figure 4.4c and illustrates the high quality of the Ag nanostencil deposition. The high resolution image shows a low defect density interface and alignment of the silver atomic planes across the interface, indicating epitaxial pillar deposition. Fast Fourier transform of this interface

region (Figure 4d) confirms contributions characteristic of a single fcc unit cell, consistent with the deposition of epitaxial nanopillars on the Ag(100) substrate.

The plasmonic response of the Ag nanopillar arrays was investigated in order to assess the potential utility of nanostencil-deposited Ag for plasmonic-based sensor, and metasurface applications. For this purpose, ZnO was sputter-deposited onto the patterned substrates covering both the patterned and unpatterned Ag(100) regions uniformly and conformally to a thickness of 140 nm (Figure 4.11). See Section 2.1.2 for details on the ZnO deposition conditions. ZnO is well known to deposit with hexagonal wurtzite structure, which lacks inversion symmetry and demonstrates second order nonlinear optical response. The second harmonic generation (SHG) response of the resulting ZnO-coated silver substrates was investigated using multiphoton confocal microscopy (Figure 4.5). Figure 5a shows the SHG response of the ZnO coated substrate in patterned and unpatterned Ag regions. With an excitation wavelength of 780 nm and detection bandwidth of 20 nm centered at 390 nm, Figure 5a demonstrates strong SHG response from ZnO/Ag(100) in the patterned nanopillared regions (bright) and comparatively little SHG from adjacent unpatterned regions (dark). While both patterned and unpatterned regions show SHG as would be expected from ZnO, we attribute the greatly enhanced SHG response of the ZnO-coated nanopillared Ag to a large increase in the local field strength in the nanopillared region through plasmonic field enhancement.³⁸⁻³⁹ Pillar-resolved SHG from the nanostencil deposited region (Figure 5b) shows nonlinear response consistent with the structure of the underlying hexagonal Ag nanopillar array, supporting this assertion. Analysis of the pillar-resolved SHG intensity from the patterned and unpatterned regions of the Ag(100) substrate indicate approximate 200-fold enhancements in SHG intensity in the nanopatterned regions compared to unpatterned regions. Note that this enhancement factor is volume averaged over the 140 nm thickness of the non-centrosymmetric ZnO overlayer, while the plasmonic field enhancement is expected to be maximum at the Ag(100)/ZnO interface, suggesting a plasmonic field enhancement due to the nanostructured silver pillars that is potentially many times larger.

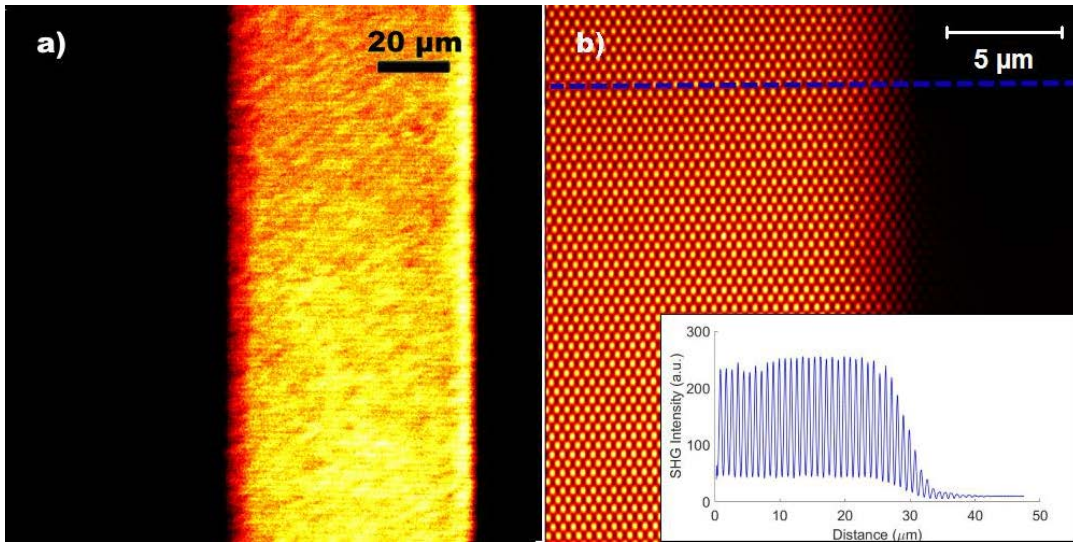


Figure 4.5. Confocal microscope image of plasmonically-enhanced second harmonic generation from ZnO-coated epitaxial silver nanopillar arrays. a) SHG image from ZnO-coated silver in patterned (bright) and unpatterned (dark) silver regions. b) Magnified image highlighting the hexagonal, pillar-resolved SHG response at the edge of the patterned nanopillar array. The inset shows the cross-sectional SHG intensity along a row of pillars indicated by the blue hatched line.

4.3. Summary

In summary, high temperature silver deposition onto H-Si(100) at thicknesses of 300 nm and above affords smooth single-crystal Ag(100) epitaxial films ideal for plasmonic and metasurface applications. These single-crystal surfaces also serve as ideal substrates for the additive manufacture of high-quality silver nanostructures through low temperature homoepitaxy. We have demonstrated the deposition of large area arrays of faceted, single-crystal silver nanopillars by nanostencil lithography and with it, their ability to provide plasmonic enhancement of local nonlinear optical response. The utility of this method can, in principle, also be extended to yield new classes of mixed-metal, crystalline nanostructures via heteroepitaxy, with the promise of new and useful properties and applications. The monocrystalline nature of the surface and nanostructure reduce losses due to material imperfection and mitigate the dissipative dynamics that currently limit quantum plasmonics applications in these materials.^{40,41} This work represents a cost effective and readily accessible approach to

the creation of high quality surface nanostructure suitable for plasmonic device research and application.

4.4. Supplemental Figures

The SEM images presented in **Figure S1** depict silver films grown on the Si(100) substrates with and without native oxide at various temperatures. Ag grown on surface oxide at 55 °C (Figure 1a) is polycrystalline with a disordered grain structure consisting of crystallites ranging in size from 10 to 400 nm separated by distinct grain boundaries at deposited thicknesses of 150 nm. These films appear mirror like to the eye. In contrast, silver films deposited on native oxide at 250°C (Figure 1b) appear cloudy. The SEM image reveals discontinuous silver coverage. Irregular islands of bare substrate, hundreds of nanometers across, are only sparsely covered by tiny, isolated grains of silver, and are surrounded by a thick, networked film of silver crystallites. The silver grains are larger than those in the low temperature deposited film and show less pronounced grain boundaries by SEM. XRD reveals them to be polydisperse in their crystalline orientation. The discontinuous morphology of these high temperature silver films was found to persist beyond deposited thicknesses of 300 nm. Silver deposited on surface oxide etched Si(100) at 55 °C (Figure 1c) exhibits larger grains with fewer pronounced grain boundaries. XRD investigation of these films revealed that the Ag crystallites, though still polydisperse in their orientation, showed a preference for the Ag[100]//Si[100] direction, as discussed. Ag depositions on H-Si terminated Si(100) at 350 °C were observed by SEM to form continuous films without observable grain boundaries or surface features at thicknesses of 300 nm (Figure 4.1d) and above.

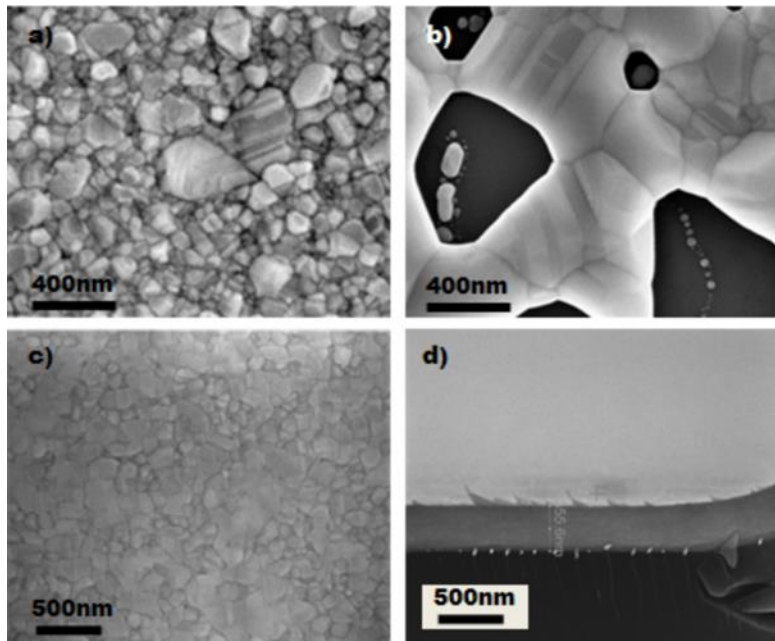


Figure 4.6 SEM images of thermally evaporated Ag film morphologies. All films were deposited at a rate of 3 \AA s^{-1} on Si(100) substrates: a) 150 nm Ag film deposited at $55 \text{ }^\circ\text{C}$ on the native oxide surface, b) 150 nm Ag film deposited at $250 \text{ }^\circ\text{C}$ on the native oxide surface, c) 300 nm Ag film deposited at $55 \text{ }^\circ\text{C}$ on a BOE etched surface, and d) tilt view of 300 nm Ag film deposited at $350 \text{ }^\circ\text{C}$ on a BOE etched surface.

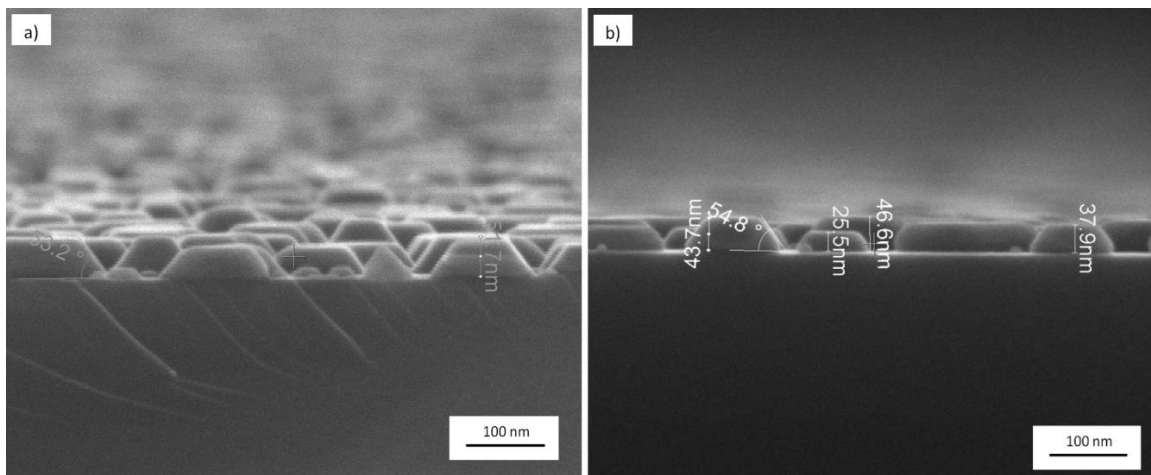


Figure 4.7 SEM cross section images of thermally evaporated Ag film morphologies on H-Si(100) deposited at $350 \text{ }^\circ\text{C}$ and a rate of 3 \AA s^{-1} . a) 50 nm Ag islands illustrating that the Ag island crystallite facets are aligned along the crystal planes of the underlying silicon. b) 50 nm Ag islands showing Ag island facet angle of 54.8° , consistent with the expected angle between (100) and (111) planes of the Ag fcc lattice.

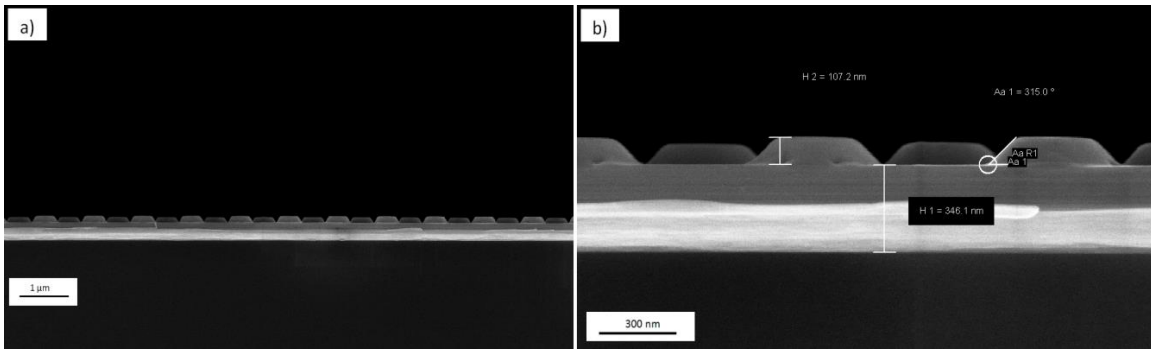


Figure 4.8. SEM cross section images of thermally evaporated Ag film morphologies on Ag(100)//H-Si(100) deposited at 55 °C and a rate of 3 Å s⁻¹ through a nanostencil mask. a) Large scale image illustrating the uniformity of the crystal nanopillar features and b) Ag island facet angle of 45°, consistent with the expected angle between (100) and (110) planes of the Ag fcc lattice.

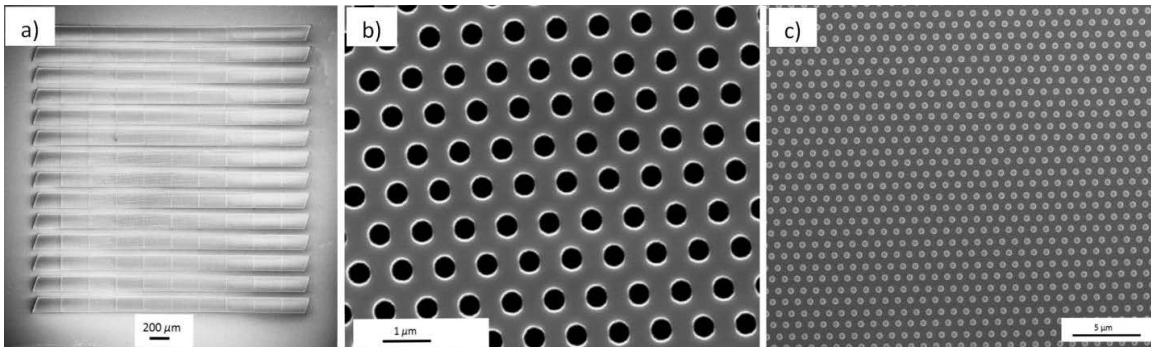


Figure 4.9. SEM top view images of a nanostencil mask illustrating a) the 3 mm × 3 mm patterned area consisting of a nanopatterned Si₃N₄ membrane supported by a silicon scaffold fabricated on a 0.6 mm thick silicon chip. The patterned region consists of 150 μm × 3000 μm windows containing b) hexagonal arrays of 450 nm diameter pores with 900 nm periodicity. c) A typical Ag nanopillar array fabricated by nanostencil lithography of Ag deposited at 55°C on Ag(100)//H-Si(100).

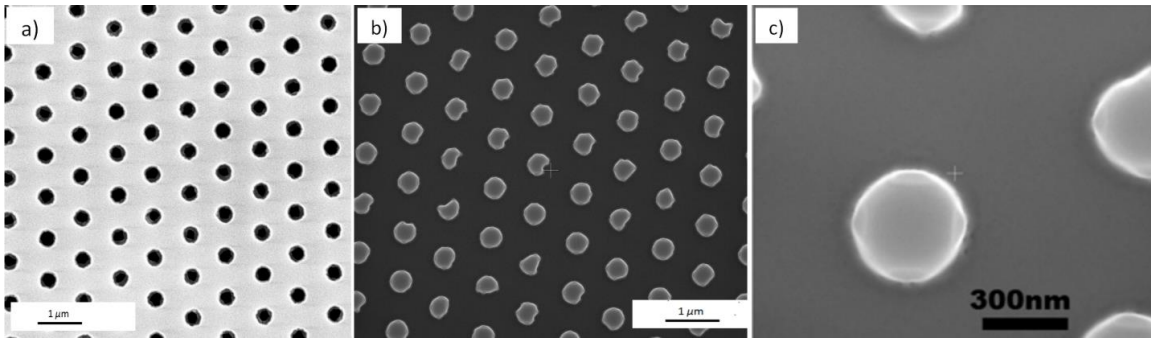


Figure 4.10. SEM top view images of a) a contaminated nanostencil mask, b) the misshapen nanopillars resulting from deposition through the contaminated mask, and c) an expanded view of pillars deposited through the contaminated mask illustrating that pillar faceting remains prevalent even under these deposition conditions.

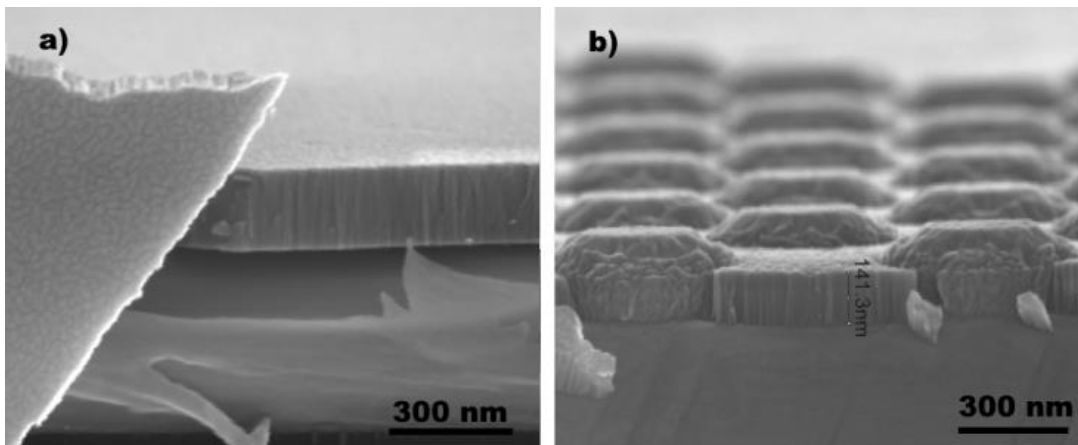


Figure 4.11. SEM images of a ZnO coated Ag(100) substrate. a) SEM image (cross section, tilt view) of 140 nm thick sputter-deposited ZnO layer atop a planar Ag(100) region of the substrate. The SEM image shows a fragmented piece of the ZnO layer in the left foreground resulting from fracture of the substrate. b) SEM image (cross section, tilt view) of 140 nm thick sputter-deposited ZnO layer atop the epitaxial silver patterned nanopillar region, illustrating the conformal coating of the Ag nanopillars. The region labeled by 141.3 nm thickness lies between Ag nanopillars and corresponds to the ZnO overlayer thickness.

References

- 1 W. L. Barnes, A. Dereux, T. W. Ebbesen, Surface plasmon subwavelength optics, *Nature*, **2003**, 424, 824.
- 2 S. A. Maier, H. A. Atwater, Plasmonics: Localization and guiding of electromagnetic energy in metal/dielectric structures, *J. Appl. Phys.*, **2005**, 98, 011101.
- 3 S. Mubeen, J. Lee, N. Singh, S. Krämer, G. D. Stucky, M. Moskovits, An autonomous photosynthetic device in which all charge carriers derive from surface plasmons, *Nat. Nanotech.*, **2013**, 8, 247.
- 4 Z. Fang, X. Zhu, Plasmonics in Nanostructures, *Adv. Mat.*, **2013**, 25, 3840.
- 5 M. L. Brongersma, N. J. Halas, P. Nordlander, Plasmon-induced hot carrier science and technology, *Nat. Nanotech.*, **2015**, 10, 25.
- 6 L. J. Brillson, Y. Lu, ZnO Schottky barriers and Ohmic contacts. *J. Appl. Phys.* **2011**, 109, 121301.
- 7 D. J. Trevor, C. E. D. Chidsey, D. N. Loiacono, In situ scanning-tunneling-microscope observation of roughening, annealing, and dissolution of gold (111) in an electrochemical cell. *Phys. Rev. Lett.*, **1989**, 62, 929-932
- 8 W. Zhang and M. K. Kannan, Epitaxial patterning of thin-films: conventional lithographies and beyond. *J. Micromech. Microeng.* **2014**, 24, 093001.
- 9 R. Liu, A. A. Vertegel, E. W. Bohannon, T. A. Sorenson, J. A. Switzer, Epitaxial electrodeposition of zinc oxide nanopillars on single-crystal gold. *Chem. Mater.*, **2001**, 13, 508.
- 10 P. Nagpal, N. C. Lindquist, S.-H. Oh, D. J. Norris, Ultrasmooth patterned metals for plasmonics and metamaterials, *Science*, **2009**, 325, 594.
- 11 E. J. R. Vesseur, R. de Waele, H. J. Lezec, H. A. Atwater, F. J. García de Abajo, A. Polman, Surface plasmon polariton modes in a single-crystal Au nanoresonator fabricated using focused-ion-beam milling, *Appl. Phys. Lett.*, **2008**, 92, 083110.
- 12 J.-S. Huang, V. Callegari, P. Geisler, C. Brüning, J. Kern, J. C. Prangma, X. Wu, T. Feichtner, J. Ziegler, P. Weinmann, M. Kamp, A. Forchel, P. Biagioni, U. Sennhauser, B. Hecht, Atomically flat single-crystalline gold nanostructures for plasmonic nanocircuitry, *Nature Comm.* **2010**, 1, 150.
- 13 H.A. Atwater, A. Polman, Plasmonics for improved photovoltaic devices. *Nature Mater.* **2010**, 9, 205.

- 14 P. Tassin, T. Koschny, M. Kafesaki, C. M. Soukoulis, A comparison of graphene, superconductors and metals as conductors for metamaterials and plasmonics, *Nat. Photonics*, **2012**, 6, 259.
- 15 Y. Wu, C. Zhang, Y. Zhao, J. Kim, M. Zhang, N. M. Estakhri, X.-X. Liu, G. K. Pribil, A. Alù, C-K. Shih, X. Li, Intrinsic Optical Properties and Enhanced Plasmonic Response of Epitaxial Silver, *Adv. Mat.*, **2014**, 26, 6106.
- 16 D. Kong, J. Drucker, Tuning Ag/Si(100) island size, shape, and density. *J. Appl. Phys.* **2013**, 114, 144310.
- 17 A.G. Brolo, R. Gordon, B. Leathem, K. L.Kavanagh, Surface plasmon sensor based on the enhanced light transmission through arrays of nanoholes in gold films. *Langmuir*, **2004**, 20, 4813.
- 18 A.V. Kildishev, A. Boltasseva, V. M. Shalaev, Planar photonics with metasurfaces. *Science*, **2013** 339, 1232009.
- 19 Y.M. Liu, X. Zhang, Metasurfaces for manipulating surface plasmons. *Appl. Phys.Lett.* **2013**, 103, 141101.
- 20 A. A. High, R. C. Devlin, A. Dibos, M. Polking, D. S. Wild, J. Perczel, N. P. de Leon, M. D. Lukin, H. Park, Visible-frequency hyperbolic metasurface, *Nature*, **2015**, 522, 192.
- 21 J.B. Pendry, Negative refraction makes a perfect lens. *Phys. Rev. Lett.* **2000**, 85, 3966.
- 22 R. A.Shelby, D. R. Smith, S. Schultz, Experimental verification of a negative index of refraction. *Science*, **2001**, 292, 77.
- 23 J. Yao, Z. Liu, Y. Liu, Y. Wang, C. Sun, G. Bartal, A. M. Stacy, X. Zhang, Optical negative refraction in bulk metamaterials of nanowires. *Science*, **2008**, 321, 930.
- 24 A. Salandrino, N. Engheta, Far-field subdiffraction optical microscopy using metamaterial crystals: theory and simulations. *Phys. Rev. B*, **2006** 74, 075103.
- 25 Z. Jacob, L. V. Alekseyev, E. Narimanov, Optical hyperlens: far-field imaging beyond the diffraction limit, *Opt. Express*, **2006**, 14, 8247.
- 26 Z. W. Liu, H. Lee, Y. Xiong, C. Sun, X. Zhang, Far-field optical hyperlens magnifying sub-diffraction-limited objects. *Science*, **2007**, 315, 1686.
- 27 M. Kuttge, E. J. R. Vesseur, J. Verhoeven, H. J. Lezec, H. A. Atwater, A. Polman, Loss mechanisms of surface plasmon polaritons on gold probed by cathodoluminescence imaging spectroscopy, *J. App. Phys.*, **2008**, 93, 113110.

- 28 H. Bialas, K. Heneka, Epitaxy of fcc metals on dielectric substrates. *Vacuum*, **1994**, 45, 79.
- 29 A. Baski, H. Fuchs, Epitaxial growth of silver on mica as studied by AFM and STM. *Surf. Sci.* **1994**, 313, 275.
- 30 J.H. Park, P. Ambwani, M. Manno, N.C. Lindquist, P. Nagpal, S.-H. Oh, C. Leighton, D.J. Norris, Single-crystalline silver films for plasmonics. *Adv. Mat.* **2012**, 24, 3988.
- 31 B.-T. Chou, S.-D. L.-H. Huang, T.-C. Lu, Single-crystalline silver film grown on Si (100) substrate by using electron-gun evaporation and thermal treatment, *J. Vac. Sci. Technol. B* **2014**, 32, 031209.
- 32 M. Hanbücken, M. Futamoto, J. Venables, Nucleation, growth and the intermediate layer in Ag/Si (100) and Ag/Si (111). *Surf. Sci.* **1984**, 147, 433-450.
- 33 K. Sumitomo, T. Kobayashi, F. Shoji, K. Oura, I. Katayama, Hydrogen-mediated epitaxy of Ag on Si (111) as studied by low-energy ion scattering. *Phys. Rev. Lett.* **1991**, 66, 1193.
- 34 T. Hanawa, K. Oura, Deposition of Ag on Si(100) surfaces as studied by LEED-AES. *Jpn. J. Appl. Phys.* **1977**, 16, 519.
- 35 C. Wang, D. E. Laughlin, M. H. Kryder, Epitaxial growth of lead zirconium titanate thin films on Ag buffered Si substrates using rf sputtering, *Appl. Phys. Lett.*, **2007**, 90, 172903.
- 36 S. R. Singamaneni, J. T. Prater, J. Narayan, Multifunctional epitaxial systems on silicon substrates, *Appl. Phys. Rev.*, **2016**, 3, 031301.
- 37 A. Linklater, J. Nogami, Defining nanoscale metal features on an atomically clean silicon surface with a stencil. *Nanotechnology*, **2008**, 19, 285302.
- 38 J. A. Schuller, E. S. Barnard, W. Cai, Y.C. Jun, J. S. White, M. L. Brongersma, Plasmonics for extreme light concentration and manipulation, *Nat. Mat.*, **2010**, 9, 193.
- 39 M. Kauranen, A. V. Zayats, Nonlinear plasmonics, *Nat. Photon.*, **2012**, 6, 737.
- 40 M. S. Tame1, K. R. McEnery, S. K. Özdemir, J. Lee, S. A. Maier, M. S. Kim, Quantum Plasmonics, *Nat. Phys.*, **2013**, 9, 329.
- 41 S. J. P. Kress, F. V. Antolinez, P. Richner, S. V. Jayanti, D. K. Kim, F. Prins, A. Riedinger, M. P. C. Fischer, S. Meyer, K. M. McPeak, D. Poulidakos, D. J. Norris, Wedge Waveguides and Resonators for Quantum Plasmonics, *NanoLett.*, **2015**, 15, 6267.

- 42 Rodionov, I. A.; Baburin, A. S.; Gabidullin, A. R.; Maklakov, S. S.; Peters, S.; Ryzhikov, I. A.; Andriyash, A. V. Quantum Engineering of Atomically Smooth Single-Crystalline Silver Films. *Sci. Rep.* **2019**, *9* (1), 12232.
- 43 Cheng, F.; Lee, C.-J.; Choi, J.; Wang, C.-Y.; Zhang, Q.; Zhang, H.; Gwo, S.; Chang, W.-H.; Li, X.; Shih, C.-K. Epitaxial Growth of Optically Thick, Single Crystalline Silver Films for Plasmonics. *ACS Appl. Mater. Interfaces* **2019**, *11* (3), 3189–3195

Chapter 5.

Nanostructured Silver/Zinc Oxide Schottky Junctions for Plasmonic Photovoltaics*

5.1. Introduction

Plasmonic hot carrier generation at nanostructured interfaces has been the focus of intense study towards practical applications in optoelectronic sensing¹, catalysis², and electrochemistry³. Though the physical mechanism of hot carrier generation in these systems has been widely explored⁴, there has been less of a focus on optimizing the material and electrical properties of such devices in order to gain deeper insights into efficient hot carrier mediated phenomena. Here we report the results of such an undertaking, enabled by an iterative design and fabrication strategy that utilizes a high throughput, low-cost metal nanopatterning technique and bottom-up materials chemistry-focused device design. This approach, which was previously applied successfully to planar surface plasmon polariton (SPP)-mediated devices (see Chapter 3), resulted in the rapid fabrication and test of over 300 test chips. These efforts, described here, gave insights into structure-function design considerations for efficient plasmonic photovoltaics and yielded high quality nanostructured surfaces that couple light to lattice resonant surface plasmons (LRSP) in good agreement with FDTD modeled absorption. Good agreement between simulated and experimental device absorption allowed meaningful analysis of how the distribution of plasmonic field intensity influences hot carrier internal photoemission probability.

Plasmonically enhanced internal photoemission of hot electrons has been an exciting area of study for over a decade⁵. Initially, excitement around the phenomena was focused on the commercial application of the technology to photovoltaics⁶, but

* The author had a major contribution to device design and fabrication, electrical characterization (along with Dr. Kourosh Khosraviani, Dr. Jayna Chan, Steven Gou, and Greg Wong), TEM (along with Dr. Xin Zhang), SHG, and FLIM imaging (with Dr. Saeid Kamal), as well as analysis of data (with all team members; see acknowledgments). The author had a minor contribution to the SEM imaging and XRD measurements (with Dr. Xin Zhang and Dr. Enrico Bovero), and minimal contribution to optical characterization and simulation (along with Dr. Tom Johansson, Dr. Haijun Qiao and Dr. Murat Cetinbas). The majority of the device data presented in Chapter 5 was gathered as part of a commercially-funded research project.

subsequent study revealed that the ultimate efficiency of this class of device is limited by fundamental physical constraints that govern the efficiency of charge separation⁷. The inelastic nature of internal photoemission⁸ and the momentum distribution of hot electrons that result from plasmon decay⁹ allow the calculation of an upper bound on device performance. Device electrical and material properties degrade performance from this theoretical maximum¹⁰. Nevertheless, optimizing the influence of these variables on photovoltaic quantum efficiency can be a guide to more efficient hot carrier mediated device design for other applications.

5.2. Results and Discussion

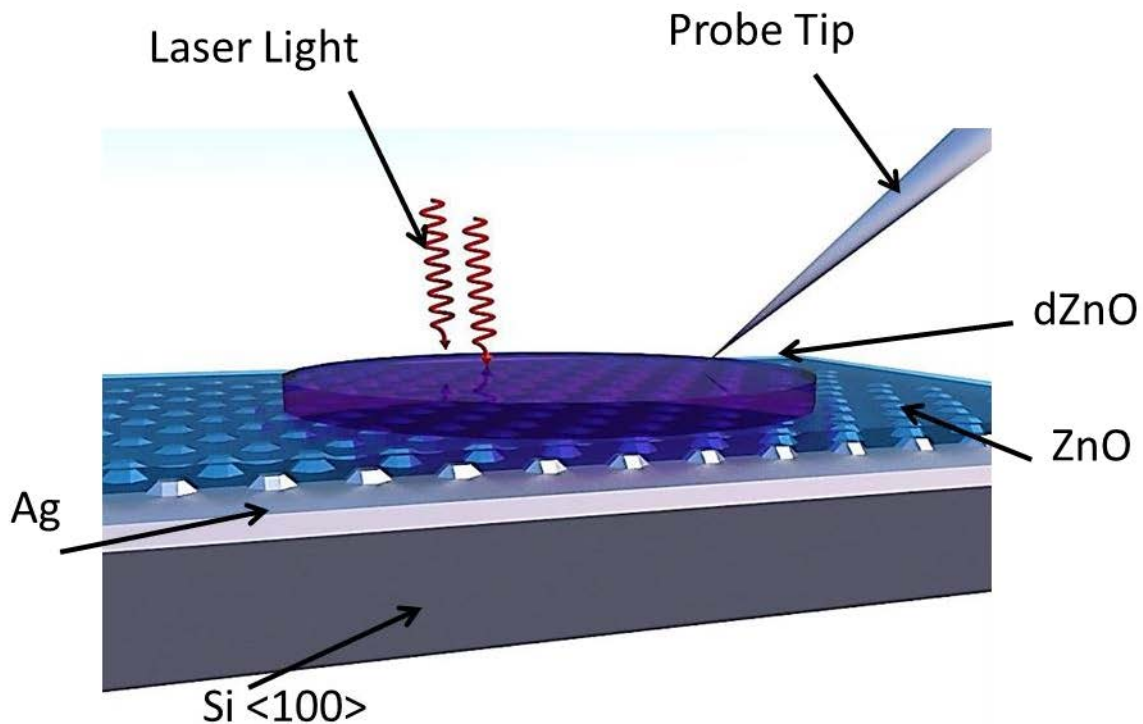


Figure 5.1. Figure 5.2. Device cartoon. The device comprises: a single-crystal Si<100> substrate coated with single-crystal Ag<100> nanostructured plasmonic coupling layer, a ZnO semiconducting layer forms a rectifying junction at the Ag interface, and a highly doped Al:ZnO transparent 250 μm circular top contact is probed with a tungsten needle. (see Chapter 2)

The choice of a “design for high throughput” experiment informed the material selection and nanostructured geometry of the devices (Figure 5.1). The design was constrained by the need for: 1) a low-cost device, 2) a device that could be fabricated without expensive and slow lithography tools, and 3) a rapid test methodology. Criterion 1 led to the design of a simple three-layer device consisting of a nanopatterned silver bottom contact, a zinc oxide semiconducting layer, and a transparent conducting Al-doped zinc oxide top contact. Silicon(100) wafers were chosen as a low-cost single-crystal substrate. Criterion 2 led to the selection of a little-known nanopatterning technique, nanostenciling²⁶ (described in detail in Chapter 4). Criterion 3 led to the choice of photovoltaic response as a measure of hot electron generation and internal photoemission probability, allowing the testing of more than 5 test chips per day.

Two major fabrication challenges were overcome during the development of the test chip architecture. The difficulty of nanopatterning ZnO by low-cost techniques necessitated the selection of silver as the bottom contact of the device. Initially, silver was PVD deposited by thermal evaporation onto silicon at ambient temperature and without HF etching the surface oxide from the Si(100). The films that resulted were of a polycrystalline morphology and yielded irregular nanostructures of poor quality upon the further evaporation of silver pillars through a nanostencil mask. The challenge was overcome through systemic study of silver layer material quality with deposition temperature on surface oxide-etched Si(100) substrate, as described in detail in Chapter 4 of this thesis. Briefly, at 350°C Ag deposits epitaxially and forms an ultra smooth and flat film with no discernable grain boundaries (see Chapter 4). Films deposited by this technique are excellent substrates for a multitude of applications¹¹. The ultra smooth silver films were then additively patterned by a second evaporation step masked by a nanostencil. The details of this procedure are discussed in Section 2.2. The resultant surfaces are patterned with a regular array of nanopillars 50-100 nm high and 450 nm in diameter. The bottom-up templating of the pillar growth on the well-oriented underlying silver led to pillars with characteristic (100) single-crystal surface features (Figure 5.3).

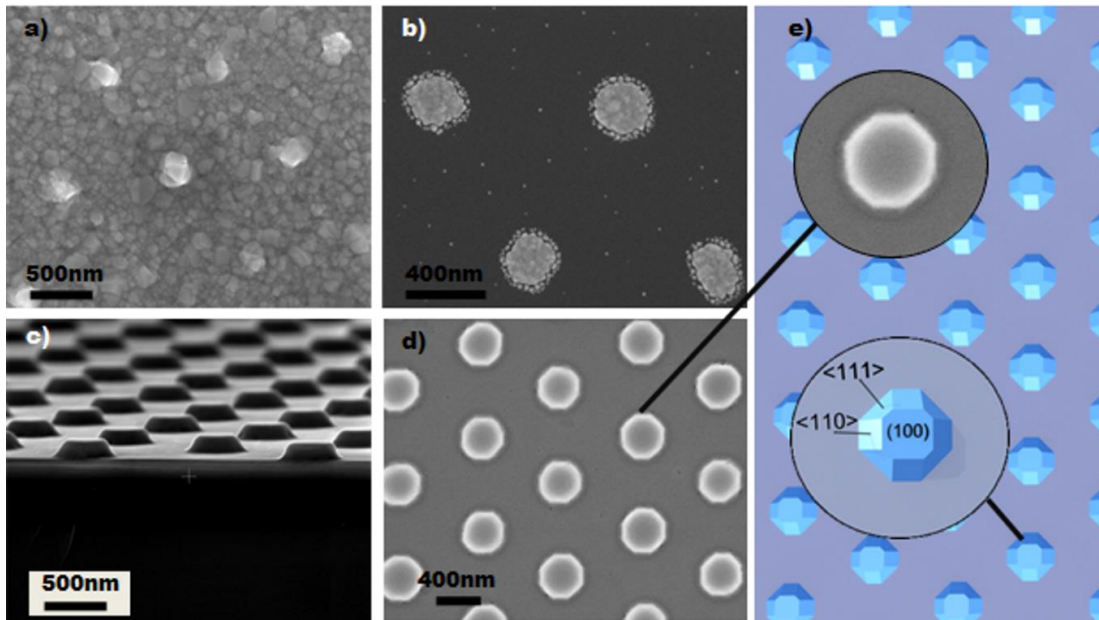


Figure 5.3. Reprinted Figure 4.3 for clarity. Low temperature nanostenciled pillars a) 100 nm on polycrystalline Ag. b) 20 nm of Ag on a native oxide terminated Si(100) c) 100 nm of Ag on a 300 nm high temperature-deposited Ag(100)//Si(100) planar film (cross section, tilt view), d) top view image of c) showing faceted nanopillars, e) schematic of epitaxial faceted crystalline silver nanopillar arrays.

A second major challenge in device development was the fabrication of a high quality Schottky junction with a silver bottom contact. A literature survey revealed that only attempts using atomic layer deposition (ALD)¹², and electrodeposition (ED)¹³ had previously yielded successful bottom metal contact ZnO Schottky diode devices. According to that extensive search, this is the first report of PVD sputter-deposited ZnO Schottky junctions with metal bottom contacts. In order to achieve good junctions in the metal bottom contact geometry using PVD sputtering, two challenges were overcome. The first was the generation of a smooth junction interface with low surface trap density and the second was the development of a high quality, low temperature sputtered ZnO deposition process. ZnO deposited with good quality electrical and material properties was previously reported to be limited to high temperature ($> \sim 400^{\circ}\text{C}$) sputter deposition²⁷. Initial experiments with polycrystalline silver films were unsuccessful, as the bottom contact was degraded during high temperature sputtering and lower temperature sputter conditions gave rise to Ohmic junctions, likely due to Fermi energy pinning resulting from large numbers of surface trap states¹⁴. Good quality junctions were achieved after many iterative experiments. Ultra smooth silver films reduced the number of surface traps and grain boundary-related defects. Successful low temperature ZnO

deposition required careful conditioning of the PVD vacuum system to eliminate all sources of water within the chamber and highly precise control over the sputter gas oxygen:argon ratio. Under these optimized conditions(see Section 2.1.2), high-asymmetry (10^5), Ag bottom contact ZnO diodes in planar geometries were fabricated with excellent properties: low ideality factors (n), low series resistance, high shunt resistance, when diode properties were fitted using the diode-resistor circuit equation (see Section 2.4.1) (Figure 5.4). Further details on the characteristics of the diodes presented in this chapter can be found in Appendix B.

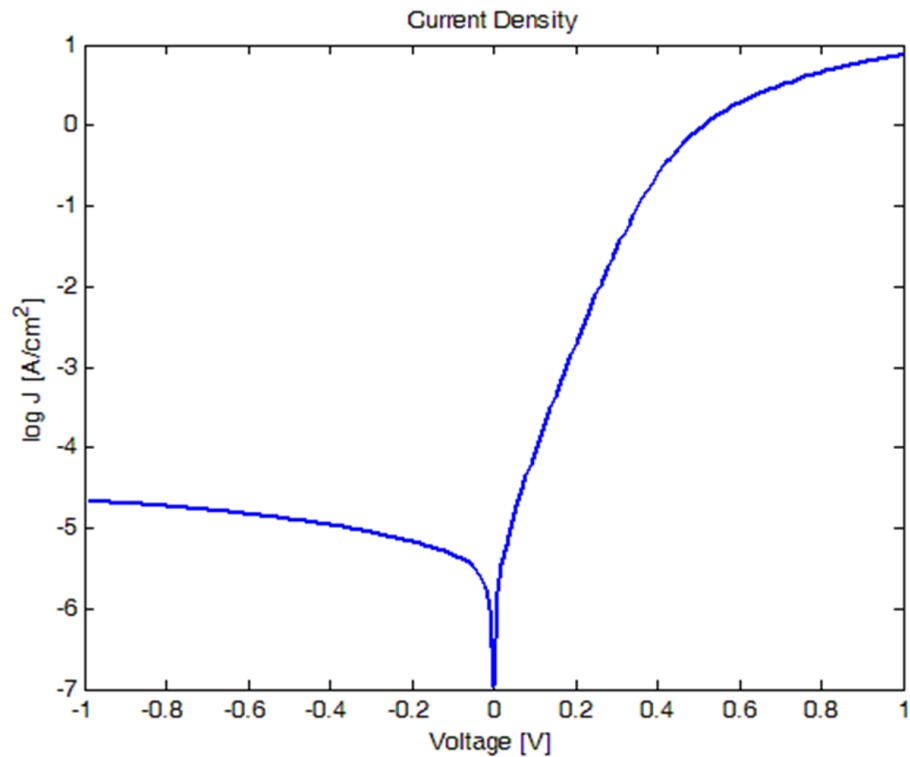


Figure 5.4. High-asymmetry planar Ag bottom contact PVD-sputtered ZnO diode curve (see Section 2.4.1).

The quality of the Schottky diodes formed on nanostructured silver surfaces was degraded from the planar case. Asymmetry values declined from 10^5 to 10^2 . The highest forward to reverse current asymmetry measured was 243 and barrier heights were typically in the range of 0.56eV. This value is lower than what is typically observed¹⁴ and indicates the presence of significant numbers of interface states and junction defects.

Despite the faceted and smooth nature of the Ag nanostructures, and two dimensional x-ray diffraction (2D XRD) spectra indicating excellent crystallinity and orientation of the Si(100)/Ag/ZnO/dZnO material stack (Figure 5.5b), a high resolution scanning electron microscope study of device cross sections reveals a possible explanation for the degraded diode performance (Figure 5.5a). Cross section images show a characteristic regular array of highly uniform pillar structures. The planar regions of the nanostructured devices exhibit ZnO films with characteristic pillar structure that extends from the top surface all the way to the silver interface. The uniformity of the ZnO through its thickness is unusual. ZnO is commonly reported to grow, by sputtering, in a cone like morphology, where the film nucleates at the interface with the substrate in very small grains that grow from a disordered interface into pillars as the film thickens¹⁴. An examination of Figure 5.5a reveals that the ZnO film exhibits a columnar morphology through the entire thickness of the film. It is thought that the templating of the ZnO crystal structure by the high-quality substrate layer gives rise to the highly ordered film quality and is the mechanistic origin of the observed Schottky junction electrical properties on planar test diodes. The morphology in the ZnO on the pillar sidewalls, however, exhibits much less ordered morphology than the planar regions. The growth orientation of the ZnO appears to tilt and disrupt the film's uniformity. The Schottky junction quality in these disordered side-wall regions of the nanostructure surface is likely the origin of the degraded diode electrical properties measured relative to the planar junctions, where disordered ZnO is not observed. A more systematic examination of the structure of the deposited ZnO close to the sidewalls of the Ag nanopillars is required to elucidate the drastic drop in rectification ratio. It is possible that points of stress concentration near the edges of the nanopillars produce dislocations in the ZnO that reduce the device performance. Techniques such as TEM, and Raman microscopy may provide more direct insight into the mechanism responsible for the observed reduction in junction quality.

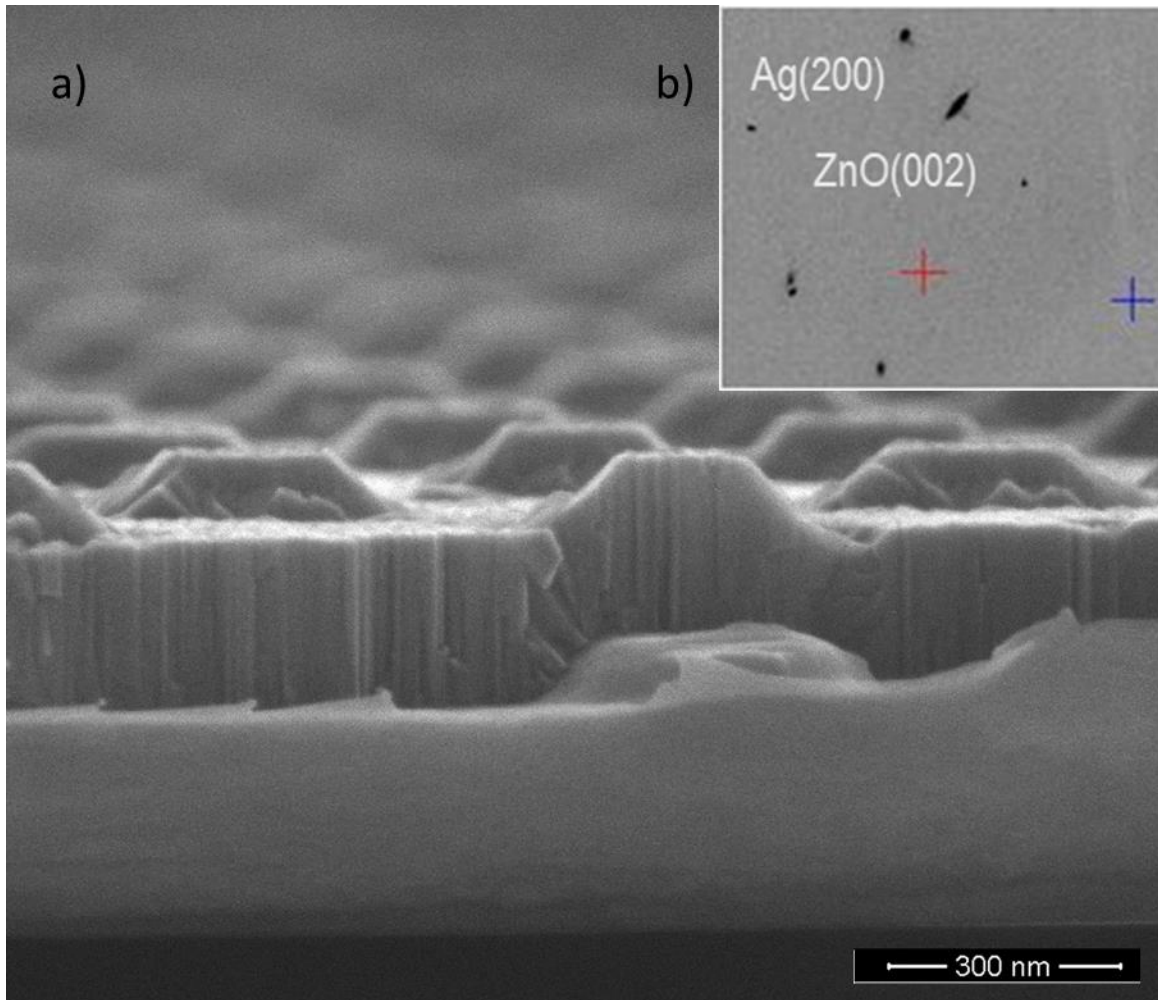


Figure 5.5. a) Cross section SEM images of the nanostructured Ag/ZnO interface. b) 2D XRD of the highly crystalline and oriented Ag and ZnO films (see section 2.3.3).

After refining the high throughput design of our test chips, the plasmonic absorption properties of the devices were first simulated using finite difference time domain (FDTD) techniques resulting in the simulated spectrum below (Figure 5.6). The constraints of the low-cost test chip design required that optical characterization and photovoltaic response be measured according to the requirements of the plasmonic response of the locally resonant surface plasmon mode structure. This mode profile, governed by the easily achievable 450 nm pillar/ 900 nm hexagonal pitch surface structure was a consequence of commercial nanostencil availability, rather than plasmon

excitation energies chosen through designed nanostructure array geometries that would require expensive and slow lithographic fabrication steps.

Figure 5.6 displays both the simulated and experimentally measured absorption spectrum of the Ag/ZnO/dZnO nanostructured devices. Simulation details are presented in Appendix B. The experimental absorption spectrum was acquired using a broadband tungsten halogen lamp fiber-coupled to an integrating sphere. The broadband light was focused onto the nanopillared regions of the device at an 8 degree angle of incidence. The detected light from the integrating sphere was outcoupled from the sphere through a fibre optic and measured using a MS260i spectrograph equipped with an electron multiplying CCD (EMCCD) (Andor, Newton) detector, thermoelectrically cooled to -60°C . Comparison of the simulated and experimentally determined spectra show good qualitative agreement. The spectra are characterized by intense long wavelength (900 – 1000 nm) resonances, the origins of which are described below.

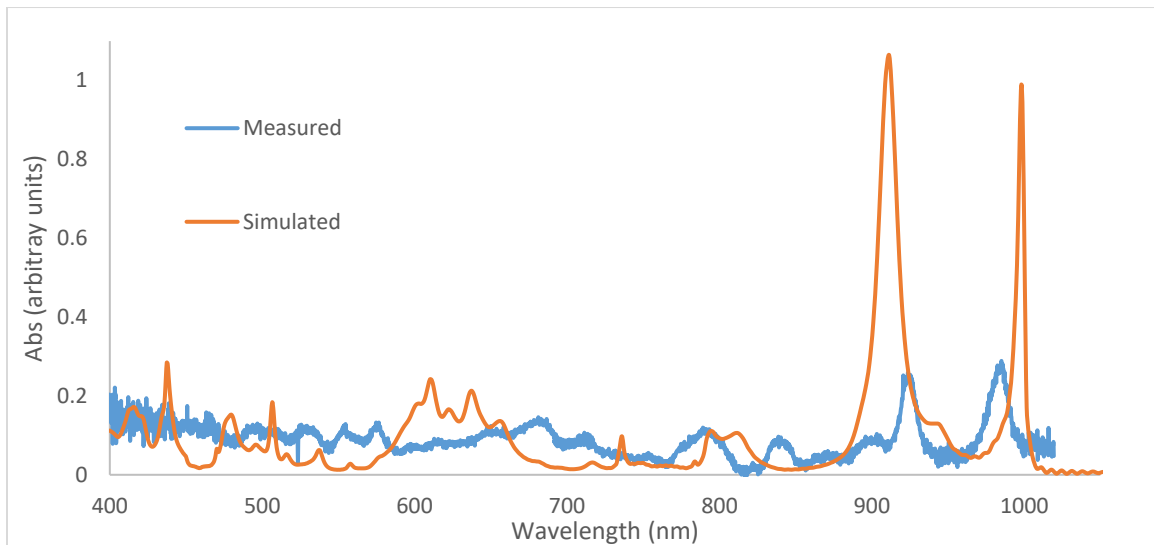


Figure 5.6. FDTD Simulated absorption vs broadband experimentally measured spectrum of the test chip design

The experimental absorption profiles of test devices were developed through measurements at discrete wavelengths utilizing a frequency tunable laser setup (see Section 2.5.2) Absorption measurements at discrete wavelengths were undertaken using the integrating sphere to quantify the absorption of the devices at a range of wavelengths (680 nm, 700 nm, 720 nm, 750 nm, 780 nm, 800 nm, 850 nm, 880 nm, 900

nm, 910 nm, 920 nm, 930 nm, 940 nm, 950 nm, and 960 nm) (Figure 5.7), coinciding with wavelengths at which device quantum efficiency was measured (see below). Initially agreement with simulation was poor until materials models were updated with optical data derived from direct ellipsometric measurements. The index of refraction (n) of the sputtered doped ZnO layer was found to be 1.8, lower than the reported literature value of $n=2.0$ ²². After adjusting the ZnO model's optical properties, reasonable agreement between simulated and experimental absorption was observed. Though the magnitude of the measured absorption peaks is lower for the test devices, the large peak appearing at approximately 908 nm in the FDTD simulated spectrum and 930 nm in the integrating sphere-based absorption spectrum is easily observed. Initially, it was thought that this plasmonic mode would give rise to the largest photovoltaic signal. The reason that this is not the case is discussed later in this Chapter.

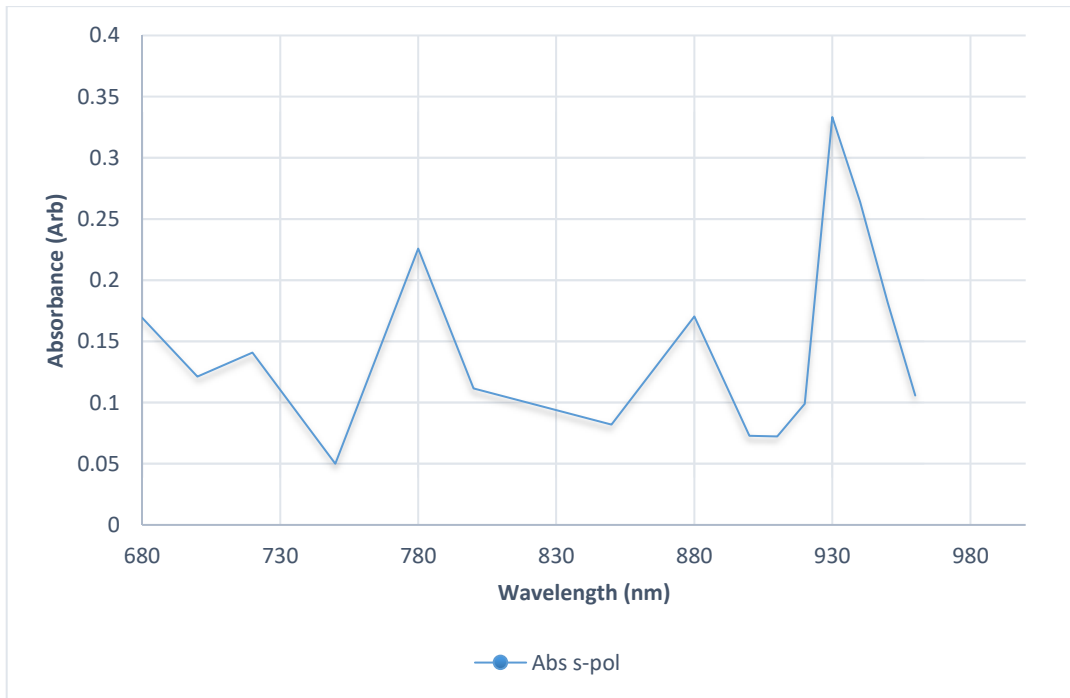


Figure 5.7. Measured absorption of a plasmonic photovoltaic test chip under s-polarized illumination. (see Section 2.5.2)

The plasmonic response of the nanostructured test chips was further explored through the use of non-linear confocal microscopy and second harmonic generation (SHG) imaging. Owing to wurtzite zinc oxide's non-centrosymmetric lattice geometry, it exhibits a well-known second harmonic response¹⁵. Plasmonically enhanced nonlinear

optical phenomena are a focus of great interest because, the intense electric fields generated at plasmonically active interfaces and their applicability to the rational design of nonlinear active metamaterials¹⁶, suggest a promising avenue for the development of novel photonic devices¹⁷. In the present case, LRSPs excited at the Ag/ZnO interface greatly enhance the electric field intensity within the ZnO semiconducting overlayer. Since second order processes are dependent on the nonlinear susceptibility ($\chi^{(2)}$) of the ZnO and on the square of the electric field intensity, the plasmonic enhancement of the signal is strong. Under the confocal microscope, SHG from the pillar regions of the nanostructures can be resolved with submicron resolution with a z-height focus at the surface of the test chip (Figure 5.8). A ~200-fold enhancement of the SHG signal over the adjacent planar region is evident. The complexity of plasmonic SHG phenomena make it difficult to determine an accurate measure of the interface plasmonic field intensity enhancement. The calculation is complicated by the difficulty in determining the volumetric distribution of the plasmonically enhanced electric field, and the complex surface geometry considerations that govern efficient SHG processes (see Section 2.6). There are many examples of plasmonically enhanced non-linear phenomena^{18,19} that demonstrate much higher second order process enhancement than presented here, though preliminary far field studies of SHG intensities from test chips indicate a greater enhancement than inferred from the confocal microscopy measurements reported here. The 200-fold SHG enhancement observed in Figure 5.8 appears to be anomalously low in comparison to the 10^4 - 10^5 enhancement factors reported in other systems.^{18,19} This modest response is attributed to the fact that the ZnO films are oriented with their <0001> axis normal to the surface. This is the polar, noncentrosymmetric optical c-axis of the ZnO and for microscopy performed at normal incidence, with the electric field vector of the incident light oriented parallel to the surface and orthogonal to the c-axis, efficient SHG response is not expected to occur¹⁹. The response is thought to come from the volume fraction of the film on the pillar edges that was observed to have a tilted crystal orientation with respect to the substrate. Excited plasmonic modes with field directions that are not perpendicular to the c-axis may also generate SHG in the normal incidence orientation.

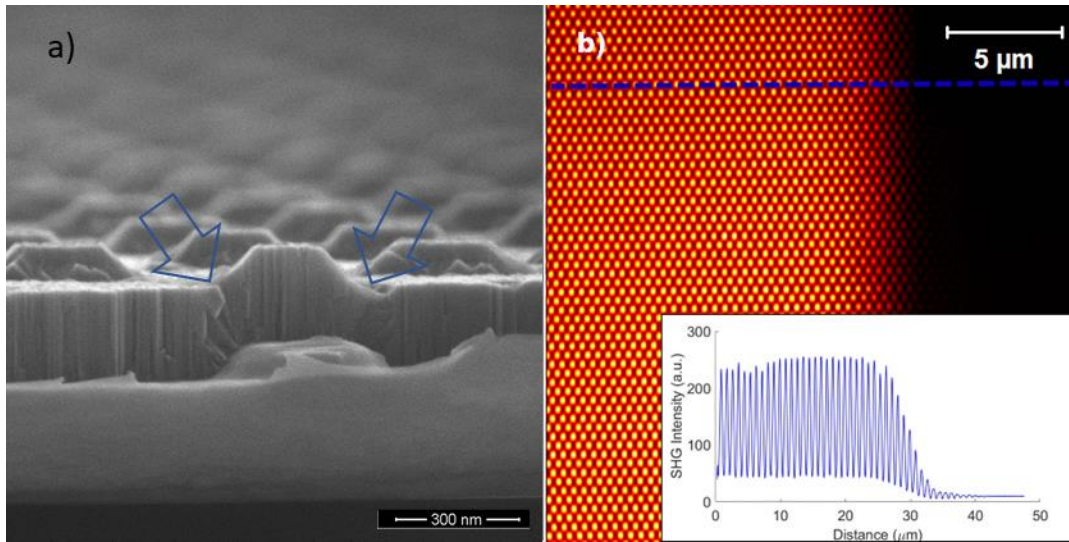


Figure 5.8. a) SEM image of a nanostructured device showing the zinc oxide with tilted c-axis orientation (arrows). Confocal microscope image of plasmonically-enhanced second harmonic generation from ZnO-coated epitaxial silver nanopillar arrays shown in a). The image highlights the hexagonal, pillar-resolved SHG response at the edge of the patterned nanopillar array. The inset shows the cross-sectional SHG intensity along a row of pillars indicated by the blue hatched line.

To examine the dependence of the plasmonically enhanced SHG on the orientation of the c-axis of the ZnO film, the nanostructured sample was removed from the microscope to the optical bench, mounted onto a rotation stage, and illuminated with light at variable angle of incidence. When oriented at an incident angle of ~ 42 degrees, the sample was found to produce an intense 2D SHG diffraction pattern (Figure 5.9) with 800 nm incident light from the Chameleon fs pulsed laser. In contrast, no observable SHG diffraction pattern was visible at normal incidence. This observation provides a rational explanation for the modest SHG enhancement observed through confocal SHG microscopy, in that under normal incidence, the geometry of the nanostructured hexagonal array does not efficiently scatter second harmonic generated light at angles readily captured by the microscope objective. Efficient SHG is instead generated under conditions in which the driving field induces an array of SHG-emitting nanopillars at 400 nm that can diffract to yield the constructive interference of the second harmonic response in the far field. A thorough investigation of the NLO behaviour of these nanostructured devices is the subject of ongoing investigation in our research laboratory.

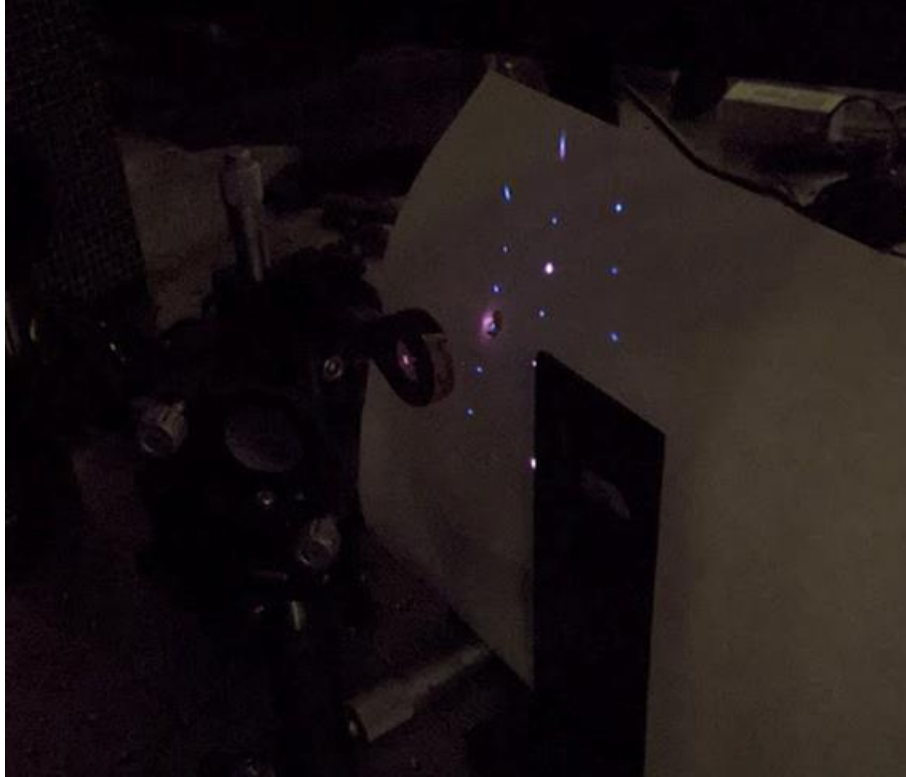


Figure 5.9. Intense 2D-SHG diffraction from a nanostructured sample under illumination with 800 nm light at 42° angle of incidence (viewed through a paper screen).

Further exploration of nonlinear device properties was undertaken to measure the time-resolved, plasmonically enhanced, two photon photoluminescence (2PPL), from the samples by confocal fluorescence lifetime imaging microscopy (FLIM) (see Section 2.6). Confocal microscopy was utilized to observe signals from samples illuminated with short-pulse 815 nm wavelength light. The signal was binned to gather the 2PPL emission from a spectral range of 500 – 650 nm and was well-fitted to luminescence decay curves with two characteristic lifetime components (Figure 5.10). 97% of the signal fit to an emission with an instrument-limited (~ 100 ps) short lifetime and 3% of the measured light decayed with a 2.1 ns average lifetime. The nanosecond component of the fluorescence lifetime image depicted in Figure 5.8b displays a characteristic herringbone structure resulting from the hexagonally-pillared surface. Qualitatively, the bi-exponential decay characteristics of the device photoluminescence can be attributed as a combination of 2PPL from the nanostructured silver layer and long-lived fluorescence from zinc oxide excited by internal photoemission. The instrument-limited short lifetime luminescence is attributed to 2PPL from doubly excited hot electrons, consistent with the ultrafast relaxation expected from plasmonically excited noble metal

nanostructures. The longer-lived fluorescence is thought to result from electrons that have undergone internal photoemission across the Ag/ZnO interface recombining with bulk defects within the zinc oxide film. The histogram inset of measured lifetimes is the result of multiple defect-mediated luminescent transitions with lifetimes characteristic of excited state ZnO²². The results of these time-resolved 2PPL studies provide supporting evidence for two characteristic and disparate timescales that result from the excitation and relaxation of SPs in the nanostructured Ag/ZnO-based devices, consistent with the internal photoemission mechanism expected to prevail following plasmonic excitation in these structures. Other nonlinear optical-based observations of plasmonically enhanced internal photoemission²³ suggest that optical characterization of charge injection plasmonic Schottky junction devices is a viable technique, useful for guiding photocatalytic device design where direct photovoltaic current measurement is non-trivial. The long-lived fluorescent signal, though consistent with an internal photoemission mediated process, cannot be unambiguously assigned as such, due to the possibility of competing luminescent processes. Fluorescence due to plasmonic resonant energy transfer from the silver to defect levels within the zinc oxide could also give rise to the observed signal. 2PPL excitation spectra show negligible fluorescence upon excitation at energies corresponding to less than half the band edge energy outside the plasmonically active pillared region. Further studies of this phenomenon would disambiguate the observed time resolved luminescence results.

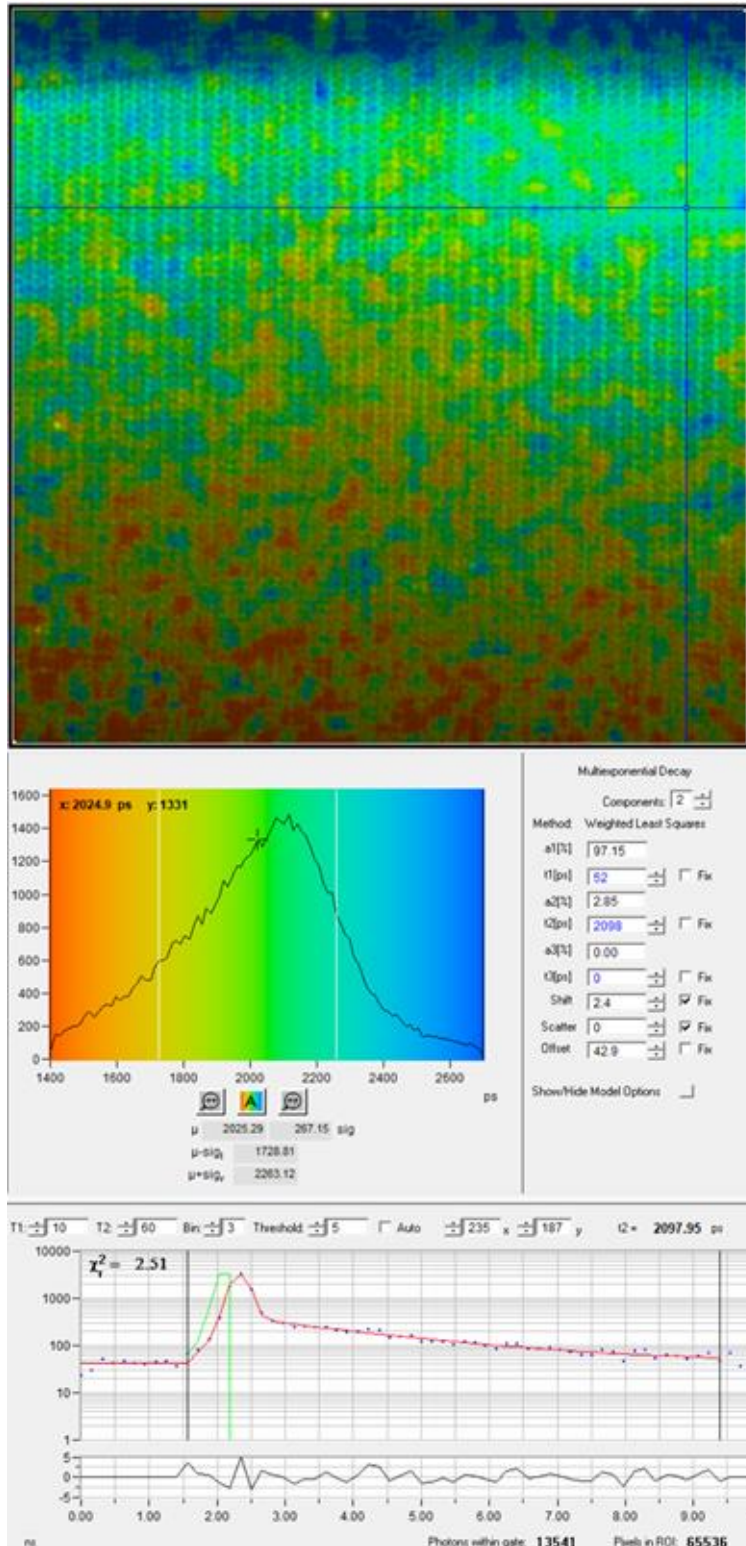


Figure 5.10. Time-resolved microscopy of 2PPL from Ag/ZnO nanostructured devices. left) Long-lived fluorescence from a nanostructured Si/Ag/ZnO/dZnO device (see section 2.5.3). right) A histogram of the measured lifetimes and lifetime fit parameters.

Many nanostructured performant devices are built from single-crystal silicon and operate in the infrared regime²⁰, in part because of the outstanding processability of single-crystal silicon substrates and the wealth of available equipment and experience that has been developed through research and development of microchips. The nanostructured films presented here provide a path toward developing highly efficient non-linear plasmonic optical elements that operate at visible wavelengths. Their smooth and faceted surfaces can not only be patterned subtractively with high fidelity²¹, but unlike silicon, can be additively patterned easily with excellent quality¹¹. Iterative design and test cycles culminated in test chips comprised of a 300 nm Ag planar film, nanostructured with 450 nm diameter pillars 100 nm tall, overcoated with a 150 nm semiconducting ZnO film. Test chip top contacts of doped ZnO were then sputtered through a nickel shadow mask to a thickness of ~100 nm to deposit an array of 250 micron circular transparent and conductive dZnO contacts. Devices were optically tested if they exhibited acceptable junction properties. Typical devices had ideality factors between 1.3 and 2.5, and current asymmetries at +/-1V of between 20 and 200 and calculated barrier heights above 0.5eV. Typical forward currents at 1V were on the order of 1 mA. Initially, device optical response was measured using a HeNe laser source calibrated to one sun intensity. At 633 nm the best devices exhibited internal quantum efficiencies of 6.5%. The maximum fill factor (FF) observed was 50%, but most test chips exhibited fill factors of between 30 and 40%. Open circuit voltage (V_{oc}) was universally low in comparison to barrier height. The dependence of V_{oc} on Schottky junction barrier height has been explored in Chapter 3 for planar, prism-coupled devices where V_{oc} was found to be linearly correlated with barrier height but offset by approximately 0.50eV. The maximum V_{oc} for nanostructured devices was 0.12V, while the average of all devices tested was 0.042V. Photoresponse and absorbance characteristics of the devices were found to depend strongly on angle of incidence and measurements were complicated initially by the difficulty in measuring device absorption accurately due to light scattering. In order to measure the photovoltaic efficiency and to investigate the wavelength dependence of the response, an integrating sphere was used to measure device absorption at a fixed 10-degree angle of incidence, and a 680-1080 nm tunable ultrafast pulsed laser with 75 MHz repetition rate was incorporated into the setup. The samples were studied across the tunable bandwidth of the laser source and photovoltaic response was measured at incident energies around the observed absorbance peaks (Figure 5.6). As expected, photovoltaic characterization of internal

and external QE from test chips did not exhibit the Fowler dependence observed for planar samples in Chapter 3 (Figure 5.11). Rather, the wavelength-dependent quantum efficiency showed resonant behavior in agreement with the FDTD simulated spectrum (Figure 5.5) and characteristic of the LRSP-based excitation mechanism.

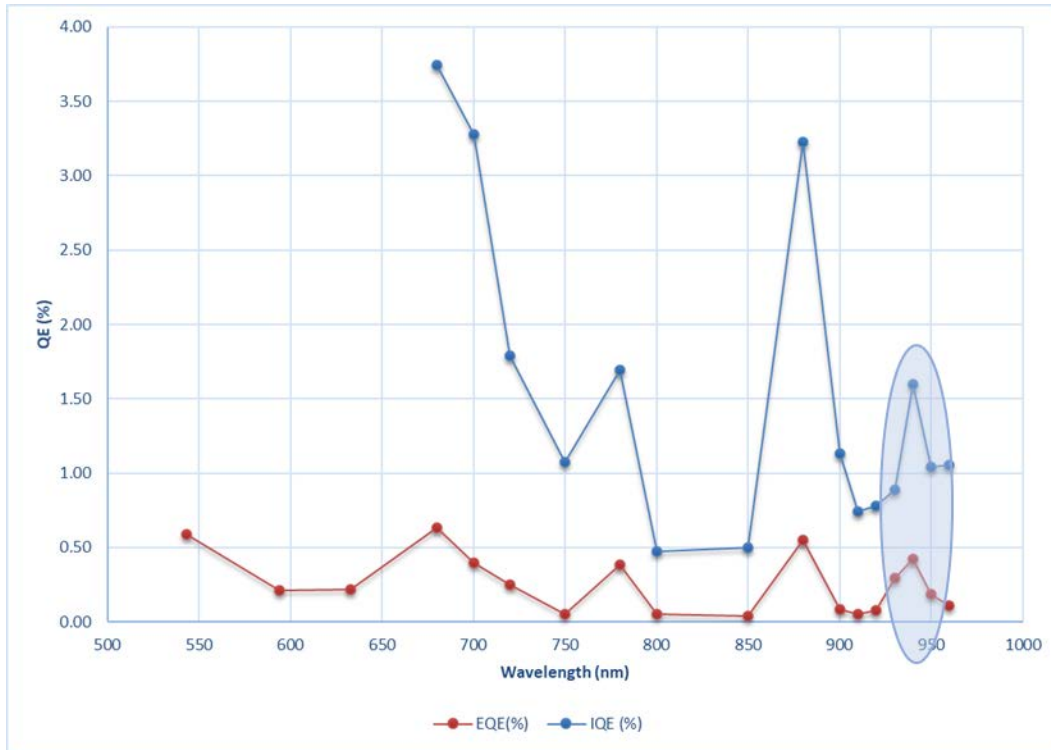


Figure 5.11. Wavelength dependent photovoltaic response. (circular callout: IQE at 930 nm is unexpectedly low in a region of high absorption)

An examination of Figure 5.11 reveals peaks in the QE of the photoresponse that correspond to the absorbance peaks at 680 nm, 770 nm, 880 nm, and 930 nm. IQE measurements were plotted according to the Fowler relation characteristic of internal photoemission discussed in Chapter 3. Hot electrons emitted during plasmon decay are predicted to surmount the junction barrier if their momentum and energy fall within a conic “escape cap” (see Section 1.4). The change in emission probability with incident photon energy should then be governed by the change in the area of the escape cap with hot electron energy. This description is complicated in the case of nanostructured devices that harvest hot electrons from LRSPs, because different resonant absorption modes can have different field distributions and can excite different regions of the

plasmonically active interface. Very tightly confined plasmonic modes, with fields confined to the corners of device pillars, may lead to the emission of hot electrons with higher probability of internal photoemission because the metal semiconductor junction is not planar. Geometries that support LRSP modes with an extended escape cap surface allow electrons emitted in many directions to surmount the barrier⁸ and may further enhance the probability of emission by reducing hot electron reflections from the interface²⁴. High interface fields confined to non-planar regions also afford the chance of multiple interface interactions within the mean free path of ballistically propagating charge, typically 40-50 nm in the case of silver⁴.

Other surface excitation modes may lower the probability of internal photoemission. LRSP modes that confine high field intensities to regions of the Schottky junction interface where films grow with a more disordered character, as observed in Figure 5.5, emit hot electrons that may undergo recombination more easily or scatter their energy in collisions at grain boundaries and defects, lowering the observed QE. Other LRSP modes excite the surface at the base of surface pillars. For these modes, the hot electrons may see a reduced escape cap since the junction surface is reduced in those regions of the nanostructures. In addition, some absorbance peaks may give rise to electric field distributions where the intensity resides away from the Ag/ZnO surface. One common example of this type of surface mode results from the coupling of LRSP excitation to non-plasmonic (photonic) grating modes, resulting in surface lattice resonances (SLR)²⁵. Plasmonic SLR have been studied as a method for enhancing the quality factor of plasmonic resonances and typically result in intense, long wavelength, narrow absorbance peaks with mixed photonic and plasmonic contributions. Figure 5.6 displays a series of narrow resonances between 980 nm and 770 nm. Their narrow FWHMs are consistent with the excitation of lattice modes with significant photonic character (see Appendix B, Figure B.8). While these features display large absorption intensities and high Q factors, SLR excitation does not necessarily lead to efficient IPE., The field intensities of the coupled excitations reside above the metal and between the metal nanostructures (Figure 5.12), as opposed to driving a large plasmonic field within the metal²⁸ in the Ag/ZnO interface region, suppressing hot electron excitation and therefore emission. Surface lattice resonance at 930 nm is thought to degrade the QE of the devices tested here. The SLR absorption feature at 980 nm in the FDTD simulated spectrum appears as the maximum intensity absorption feature in the spectrum.

Similarly, the largest resonance observed in the experimental, line-tuned absorption spectrum (Figure 5.7) appears as the longest wavelength resonance at 930 nm. Based on the magnitude of the absorption, one may have expected to observe a larger hot electron yield and photovoltaic efficiency at this resonant wavelength. However, the IQE and EQE wavelength-dependent results of Figure 5.11 illustrate a lower-than-expected photovoltaic efficiency based on resonant absorption arguments. This observation highlights the complexities and challenges of the nanostructured device design. The conditions for efficient internal photoemission require not only optical coupling that drives a large plasmonic field distribution localized in the metal to yield a large hot electron population, but in addition, also requires excellent junction quality in this region where the plasmonic field is high to drive these excited carriers through internal photoemission into the conduction band of the adjacent dielectric. This represents perhaps the greatest technical challenge, as plasmonic field maxima tend to appear at discontinuities in the metal nanostructure (at the corners and edges of faceted nanopillars, for example) where the deposition of subsequent overlayers is more likely to lead to material defects and poorer junction quality

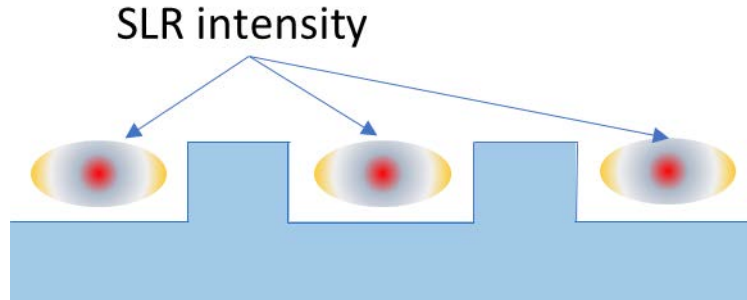


Figure 5.12. Surface lattice resonance with electric field intensity distribution between the pillars rather than near the ZnO-Ag Schottky interface can lower expected IQE.

It proves instructive to compare the performance of the nanostructured LRSP-based devices to the planar SPP-based devices described in Chapter 3. The operating wavelengths of the nanostructured devices, dictated by the periodicity of the commercially available nanostencils, appear in the near infrared spectral region. While this renders a direct comparison impossible, one can extrapolate the wavelength dependent quantum efficiency of the SPP devices to the near infrared spectral region. Based on the Fowler dependence of the planar SPP-based devices, one would expect near infrared (880 nm or 1.40 eV) quantum efficiencies in the range of 3%, consistent

with the measurements of Figure 5.10 on the LRSP-based nanostructured devices. This agreement illustrates that some of the anticipated benefits and enhancements expected from nanostructured devices have not been realized in the current nanostructures. As described, the material deposition challenges required to achieve excellent junction characteristics in the locations of high plasmonic field enhancement likely mitigate the greater degree of localization of the plasmonic field distribution for LRSP excitation compared to SPP excitation. Further, while one may anticipate based on geometric arguments, a larger potential escape cone for the nanostructured interface compared to the planar interface, the size scale of the nanopillar features in the present case (~450 nm) does not compare favorably with the ~50 nm mean free path length of electrons in silver, limiting any anticipated potential LRSP-based benefits on these grounds. These limitations highlight current bottlenecks in fabrication capability and emphasize the need for new approaches to scalable single-crystal materials deposition.

5.3. Summary

The extraction of plasmonic hot carriers at nanostructured interfaces has been investigated through the study of the photovoltaic response of nanopillared Ag/ZnO structures. Informed by the requirements established for high efficiency performance of planar SPP-based photovoltaic response of this material pair, the design for high throughput approach to LRSP-based nanostructured test chip fabrication enabled rapid iterative improvements of the material and electrical properties of device layers. The resulting structures display large and uniform nanopillar-based plasmonic field enhancement that leads to efficient nonlinear optical response in the form of second harmonic generation from the pillars. These plasmonic fields also give rise to hot electron distributions that culminate in nanostructured plasmonic photovoltaic response and devices with good performance relative to previously reported solid state designs^{10,6,26} – a mechanism supported by time-resolved 2PPL measurements. Comparison of nanostructured device efficiency with the efficiencies of planar SPP-based devices described in detail in Chapter 3 provide guidance for how these devices could be further improved.

High-quality nanostructured interfaces with absorption properties that agree with simulation have previously been primarily limited to infrared wavelengths compatible with highly processable silicon substrates²⁷. The work presented here demonstrates that

continued studies grounded in high quality material combinations such as those presented here, present an excellent avenue for simulation-informed plasmonically enhanced, hot carrier-based devices with response in the optical regime. This work helps to guide further development of devices that employ plasmonic field enhancement for linear and nonlinear optical response as well as hot carrier-based devices for application in energy harvesting, sensing, and photocatalysis.

References

- 1 Mirzaee, S.M., Lebel, O. and Nunzi, J.M., 2018. Simple unbiased hot-electron polarization-sensitive near-infrared photodetector. *ACS applied materials & interfaces*, 10(14), pp.11862-11871.
- 2 Hartland, G.V., Besteiro, L.V., Johns, P. and Govorov, A.O., 2017. What's so hot about electrons in metal nanoparticles?. *ACS Energy Letters*, 2(7), pp.1641-1653.
- 3 Yu, Y., Wijesekara, K.D., Xi, X. and Willets, K.A., 2019. Quantifying wavelength-dependent plasmonic hot carrier energy distributions at metal/semiconductor interfaces. *ACS nano*, 13(3), pp.3629-3637.
- 4 Christopher, P. and Moskovits, M., 2017. Hot charge carrier transmission from plasmonic nanostructures. *Annual review of physical chemistry*, 68, pp.379-398.
- 5 Hobbs, P.C., Laibowitz, R.B., Libsch, F.R., LaBianca, N.C. and Chiniwalla, P.P., 2007. Efficient waveguide-integrated tunnel junction detectors at 1.6 μm . *Optics express*, 15(25), pp.16376-16389.
- 6 Knight, M.W., Sobhani, H., Nordlander, P. and Halas, N.J., 2011. Photodetection with active optical antennas. *Science*, 332(6030), pp.702-704.
- 7 White, T.P. and Catchpole, K.R., 2012. Plasmon-enhanced internal photoemission for photovoltaics: theoretical efficiency limits. *Applied Physics Letters*, 101(7), p.073905.
- 8 Sundararaman, R., Narang, P., Jermyn, A.S., Goddard III, W.A. and Atwater, H.A., 2014. Theoretical predictions for hot-carrier generation from surface plasmon decay. *Nature communications*, 5(1), pp.1-8.
- 9 Scales, C. and Berini, P., 2010. Thin-film Schottky barrier photodetector models. *IEEE Journal of quantum electronics*, 46(5), pp.633-643.
- 10 Mubeen, S., Lee, J., Lee, W.R., Singh, N., Stucky, G.D. and Moskovits, M., 2014. On the plasmonic photovoltaic. *ACS nano*, 8(6), pp.6066-6073.
- 11 V. Grayli, S., Zhang, X., MacNab, F.C., Kamal, S., Star, D. and Leach, G.W., 2020. Scalable, green fabrication of single-crystal noble metal films and nanostructures for low-loss nanotechnology applications. *ACS nano*, 14(6), pp.7581-7592.
- 12 Krajewski, T.A., Luka, G., Gieraltowska, S., Zakrzewski, A.J., Smertenko, P.S., Kruszewski, P., Wachnicki, L., Witkowski, B.S., Lusakowska, E., Jakiela, R. and Godlewski, M., 2011. Hafnium dioxide as a passivating layer and diffusive barrier in ZnO/Ag Schottky junctions obtained by atomic layer deposition. *Applied Physics Letters*, 98(26), p.263502.

- 13 Benlamri, M., Wiltshire, B.D., Zhang, Y., Mahdi, N., Shankar, K. and Barlage, D.W., 2019. High breakdown strength schottky diodes made from electrodeposited ZnO for power electronics applications. *ACS Applied Electronic Materials*, 1(1), pp.13-17.
- 14 Brillson, L.J. and Lu, Y., 2011. ZnO Schottky barriers and Ohmic contacts. *Journal of Applied Physics*, 109(12), p.8.
- 15 Janotti, A. and Van de Walle, C.G., 2009. Fundamentals of zinc oxide as a semiconductor. *Reports on progress in physics*, 72(12), p.126501.
- 16 Kauranen, M. and Zayats, A.V., 2012. Nonlinear plasmonics. *Nature photonics*, 6(11), pp.737-748.
- 17 Panoiu, N.C., Sha, W.E., Lei, D.Y. and Li, G.C., 2018. Nonlinear optics in plasmonic nanostructures. *Journal of Optics*, 20(8), p.083001.
- 18 Novotny, L. and Van Hulst, N., 2011. Antennas for light. *Nature photonics*, 5(2), pp.83-90.
- 19 Weber, N., Protte, M., Walter, F., Georgi, P., Zentgraf, T. and Meier, C., 2017. Double resonant plasmonic nanoantennas for efficient second harmonic generation in zinc oxide. *Physical Review B*, 95(20), p.205307.
- 20 Li, G., Zhang, S. and Zentgraf, T., 2017. Nonlinear photonic metasurfaces. *Nature Reviews Materials*, 2(5), pp.1-14.
- 21 High, A.A., Devlin, R.C., Dibos, A., Polking, M., Wild, D.S., Perczel, J., De Leon, N.P., Lukin, M.D. and Park, H., 2015. Visible-frequency hyperbolic metasurface. *Nature*, 522(7555), pp.192-196.
- 22 Rodnyi, P.A. and Khodyuk, I.V., 2011. Optical and luminescence properties of zinc oxide. *Optics and Spectroscopy*, 111(5), pp.776-785.
- 23 Manuel, A.P. and Shankar, K., 2021. Hot Electrons in TiO₂-Noble Metal Nano-Heterojunctions: Fundamental Science and Applications in Photocatalysis. *Nanomaterials*, 11(5), p.1249.
- 24 Grajower, M., Levy, U. and Khurgin, J.B., 2018. The role of surface roughness in plasmonic-assisted internal photoemission schottky photodetectors. *Acs Photonics*, 5(10), pp.4030-4036.
- 25 Kravets, V.G., Kabashin, A.V., Barnes, W.L. and Grigorenko, A.N., 2018. Plasmonic surface lattice resonances: a review of properties and applications. *Chemical reviews*, 118(12), pp.5912-5951.
- 26 K., Ding, J., Liu, Y., Wathuthanthri, I. and Choi, C.H., 2017. Stencil lithography for scalable micro-and nanomanufacturing. *Micromachines*, 8(4), p.131.

- 27 Kluth, O., Schöpe, G., Hüpkes, J., Agashe, C., Müller, J. and Rech, B., 2003. Modified Thornton model for magnetron sputtered zinc oxide: film structure and etching behaviour. *Thin solid films*, 442(1-2), pp.80-85.
- 28 Khlopin, D., Laux, F., Wardley, W.P., Martin, J., Wurtz, G.A., Plain, J., Bonod, N., Zayats, A.V., Dickson, W. and Gérard, D., 2017. Lattice modes and plasmonic linewidth engineering in gold and aluminum nanoparticle arrays. *JOSA B*, 34(3), pp.691-700.

Chapter 6. Conclusions and Future Work

The comprehensive characterization of the silver-zinc oxide Schottky junction material pair's plasmonic photovoltaic response grew from a ~3.5-year commercialization effort. The data that supports this work was collected by more than a dozen researchers at a significant cost. Thousands of iterative optimizations and intuitive leaps, which coalesced into several successful device geometries, were performed. A slice of this body of work -the two most usefully characterized device designs- comprise the basis for the analysis in the preceding pages.

The challenge of plasmonic hot electron science is in understanding and integrating the three pillars of device efficiency: (i) plasmonic excitation, (ii) plasmon decay and hot carrier transport, and (iii) rectification of the carrier's energy across an interface. One of the primary goals of this thesis has been to introduce these processes and to explain how they depend on material and junction quality, providing perspective on the challenges in efficient device design. The work describes a systematic approach to the design, testing and characterization of devices to establish structure-function relationships, highlighting the materials science focus that underpinned the high-throughput device optimization strategies employed.

The systematic study of hundreds of prism-coupled devices, presented in Chapter 3, allowed the identification of statistical trends in the collected data. The different electrical and material properties measured were observed to influence QE to varying degrees. The structure-function approach to maximizing device efficiency, and resultant devices of unparalleled material quality, allowed meaningful comparisons between theory and experiment. The close agreement between the Scales theoretical efficiency model (Section 1.4) and the highest observed quantum efficiency from the samples, suggest that the practical limits of plasmonic photovoltaic efficiency were approached (11.2% IQE @ 543 nm).

Chapter 4 described the first steps in applying the high throughput structure-function approach to the problem of free space-coupled plasmonic nanostructured hot carrier devices. Iterative experiment led to the development of a novel technique for depositing single-crystal, ultrasmooth, epitaxial silver films, on silicon substrates. The smooth oriented silver was shown to be an excellent substrate for the further deposition

of nanostencilled silver pillars to form a hexagonal array of crystalline lattice-resonant plasmonic nanostructures. The plasmonic response of the surface was highlighted through the observation of intense SHG emission enhancement.

In Chapter 5, a metal bottom contact silver-zinc oxide Schottky junction with ZnO deposited by magnetron sputtering was demonstrated. This novel result was examined for planar substrates and was found to have excellent material quality and form a robust diode. The result could only be partially extended to nanostructured substrates, due to a reduced templating effect on the morphology of the sputtered ZnO film. Nonetheless, the refined material properties of the test devices showed good agreement between simulated and experimental absorbance spectra, allowing the identification of strongly absorbing surface lattice resonant modes.

The structure-function design approach has proven to be a successful strategy for developing devices with high enough quality to generate good theoretical-experimental agreement. This research holds promise as a platform of material fabrication and design strategies that can be leveraged to extend our understanding of plasmons and hot carrier dynamics across a broad range of applications, including plasmonic photocatalysis, plasmonic electrochemistry, optics, and sensors.

Several possible paths to higher efficiency plasmonic photovoltaics can be imagined, but the challenges highlighted by the structure-function relationships explored here, make their practical realization a challenge. The primary path to higher efficiencies is reducing the size scale and increasing the surface area of nanostructured PV devices. This would have the effect of increasing the probability of photoemitted hot electrons reaching the interface with sufficient energy to undergo internal photoemission. The challenge of this approach (see Chapter 5) is that poor Schottky junction quality at irregular interfaces degrades device performance, and the lattice resonant response of the plasmonic device suffers from angle and wavelength dependent absorption limitations. Maximizing the absorption and electron transport properties of a plasmonic PV nanostructure compromises the rectifying Schottky junction's quality, leading to a combined efficiency limit that has not yet been found. Future success may come from the utilization of a surface geometry insensitive semiconductor deposition technique such as electrodeposition (See Chapter 4).

It is unlikely that plasmonic internal photoemission will ever be adapted for commercial solar energy conversion in competition with existing, silicon-based, solutions with higher power conversion efficiency and lower cost, but the structure-function design considerations explored in these chapters are a useful guide towards plasmonic IPE device applications in the areas of photosensing, photocatalysis, and electrochemistry. Plasmonic IPE is particularly suited to sensing and electrochemical applications, where the strengths of the unique mechanism can be leveraged to build devices with unique properties.

Because Schottky junction barrier height is tunable through material selection and interface engineering, electrons with energies below the silicon bandgap (1.1eV) can be charge-separated across the junction (see Chapter 1). This range of energies is not accessible to commodity silicon-based sensors and existing solutions, such as InGaAs based sensors, are expensive and difficult to fabricate. The applications of photosensors that operate in the short-wave infrared (SWIR) window (0.4eV to 1.2 eV) are broad. The short-wave regime is very weakly absorbed by the atmosphere over much its bandwidth because it resides between the shoulder regions of energies associated with electronic transitions and those of vibrational excitations. As a result, short wave imaging penetrates fog and cloud readily at some wavelengths and is absorbed at others in material dependent ways with characteristic fingerprints. These intriguing light matter interactions make SWIR camera detectors a focus of intense interest for their potential application to autonomous driving, satellite-based crop monitoring, SWIR monitoring of produce quality, and defense related activities.

Adapting the research presented here to the design and fabrication of SWIR sensors is a project underway within our research group, with initial funding from the Canadian Department of National Defense.

A second avenue of research with less immediate commercial value, but that holds promise in the pursuit of advanced interface studies and nanostructuring using maskless, “bottom-up” approaches, is plasmonic IPE driven electrochemistry. Traditional electrochemistry applies macroscopic potentials to electrodes in order to control microscopic processes, such as metal deposition. Hot electrons emitted from an interface with a well designed plasmonic response, can engender designed microscopic fields and electron fluxes that open new possibilities for the growth of films using light.

Initial experiments using polycrystalline gold films immersed in acidic gold salt solution resulted in plasmonically-mediated electrodeposition when SPPs were excited at the gold electrolyte interface (Figure 6.1).

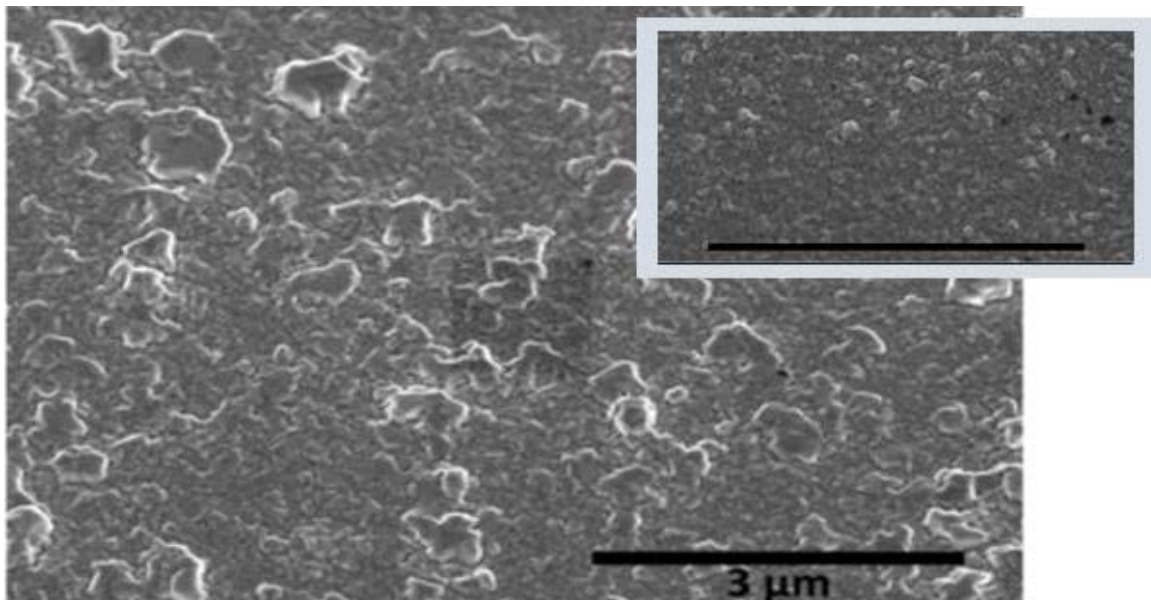


Figure 6.1. Gold plasmonically electrodeposited from a gold chloride solution on a polycrystalline gold film excited with 650 nm incident light in a Kretschmann coupled geometry. Inset) A region of the same film that was not illuminated, at identical magnification.

Extending these preliminary results with experiments on highly oriented smooth and nanostructured films, such as those described in Chapter 4 is one obvious approach that inform these studies. A smooth controlled geometry, with known plasmonic field intensity distribution at the interface, could mediate electrodeposition and other redox processes, yielding microscopic control of the reactions. This would enable new 3D nanostructures, with novel optical properties, and give insights into hot electron emission dynamics, through exploring the spatial relationship between electrodeposited surface features and the plasmonic fields driving the hot carrier generation.

It is hoped that the passion and dedication of the researchers that contributed to the material presented here inspires others to consider the importance of structure-function design considerations to the study of plasmon hot carrier generation and plasmonics generally.

Appendix A.

Supplementary Data File

Description:

Appendix A is available as a supplemental file through the SFU library. It describes a novel patented lithography process developed over the course of this work. The process termed rapid electron area masking (REAM lithography) enables high throughput, low cost patterning of nanostructures by exposing e-beam resist through a multilayer, low-stress, patterned membrane that, when positioned above a substrate, can mask the intensity of an electron beam, enabling nanopatterning without the requirement of focusing and guiding an electron beam with nanometer precision.

Filename:

etd21768-finlay-macnab-Finlay MacNab Thesis Appendix A.pdf

Appendix B.

Supplementary Data File

Description:

This appendix contains the accompanying executable file, and the details of diode curve fitting procedures and examples of diode IV curves from devices described in Chapter 3 (prism coupled devices) and Chapter 5 (nanostructured devices).

Filename:

etd21768-finlay-macnab-fitIV2_win64_with output.exe

Diode Parameter Fitting

Diodes were fit to equation 2.3 using a numerical solver program written in MATLAB scripting code. The standalone application is available as a supplemental file through the SFU library. A screenshot of the application is shown in Figure B.1.

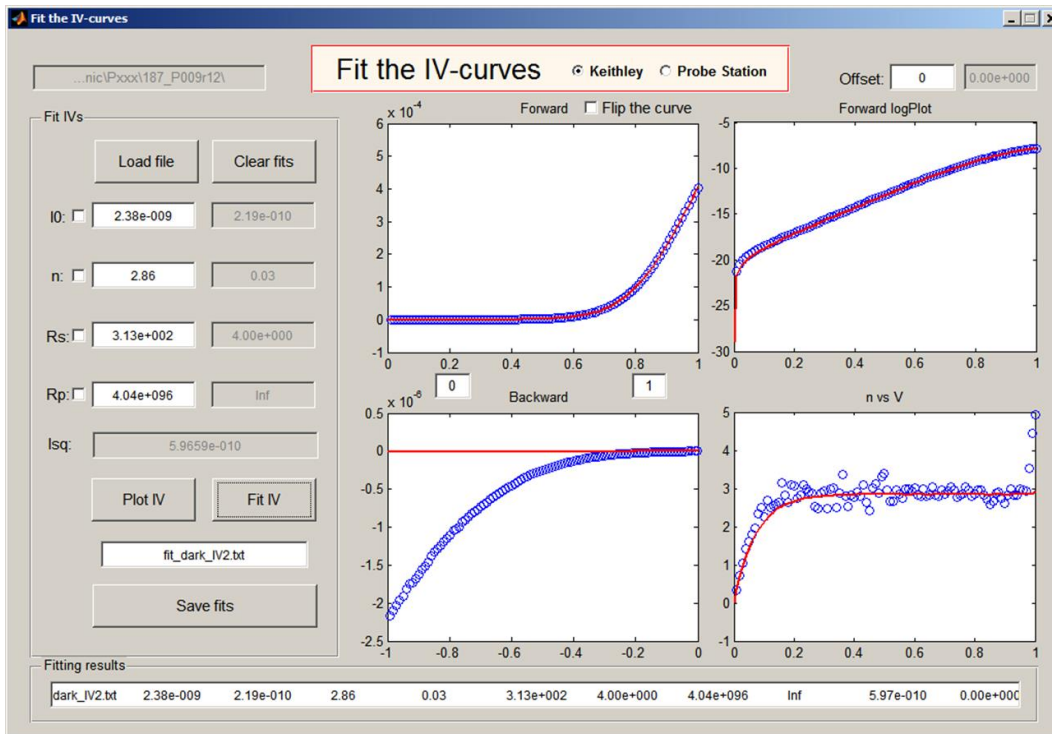


Figure B.1. The diode fitting application GUI

The application is designed to accept data as .csv files or from an Agilent Technologies B1500A semiconductor device analyzer. The numerical methods are based on the assumption that $V + R_s I \gg kT$.

Details of Prism Device Diode Testing

Each prism sample was shadow-masked with an array of 150 nm thick silver top contact pads with a diameter of 250 μm . The samples were mounted in the optical test station and the contact pads were imaged with magnifying optics through a digital imaging camera. A sample image of one device, sample P11r35 is shown in Figure B.2. The contacts are numbered to indicate the pad testing order and position.

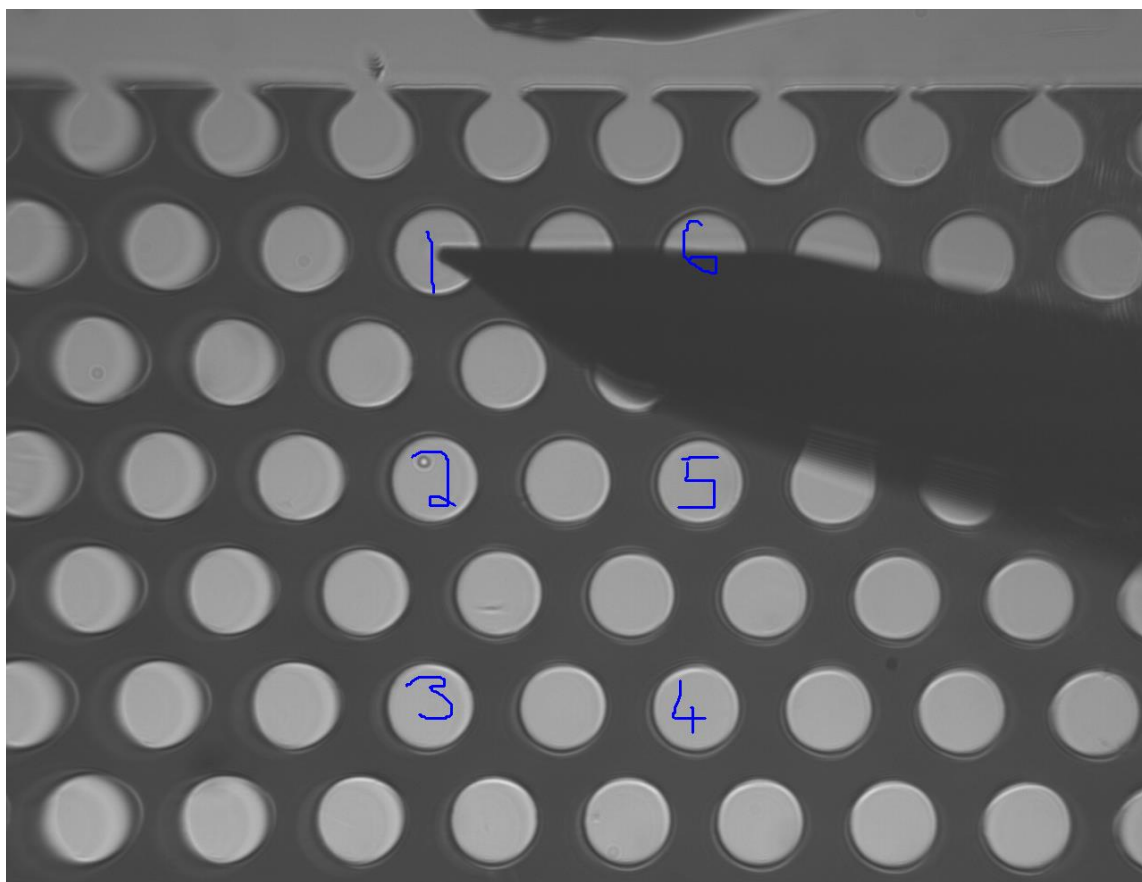


Figure B.2 Magnified image of 250 μm contact probes under test. Sample numbers indicate the order of testing. The probe tip and its shadow are visible.

Current-Voltage response was measured for each device in the dark and under 633nm illumination as described in Section 2.5.1. Figure B.3 depicts IV plots from the first 3 tested top contacts from the sample. The reported value used for further analysis was always based on a single measurement that was representative of the surveyed contacts.

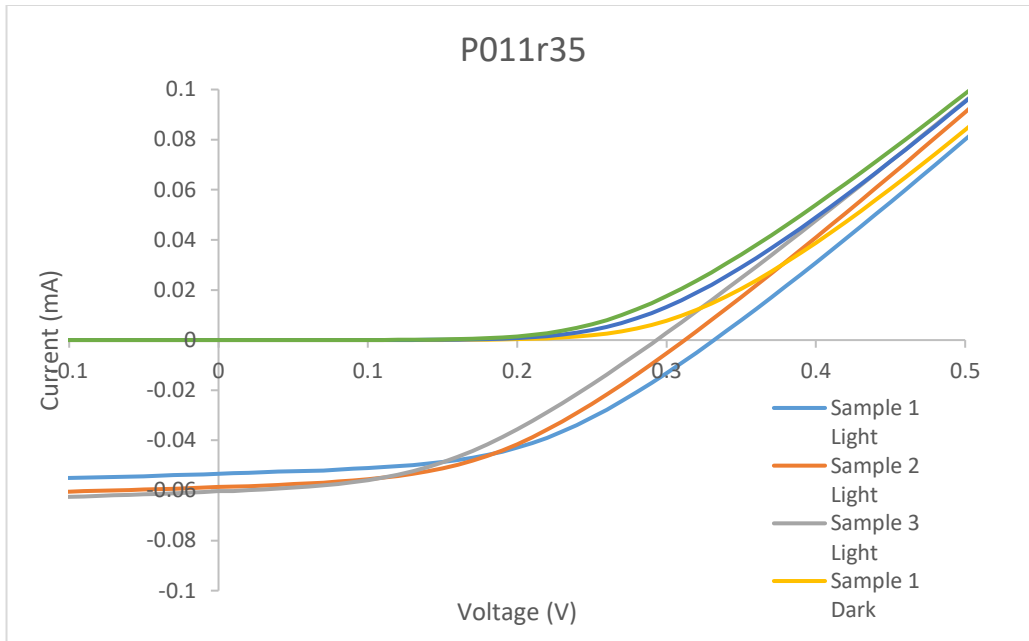


Figure B.3 Examples of light and dark curves for sample P011r35. Samples were illuminated as described in Section 2.5.1 at 633nm.

Figure B.4 depicts the same measurements plotted on a log scale with a larger voltage range.

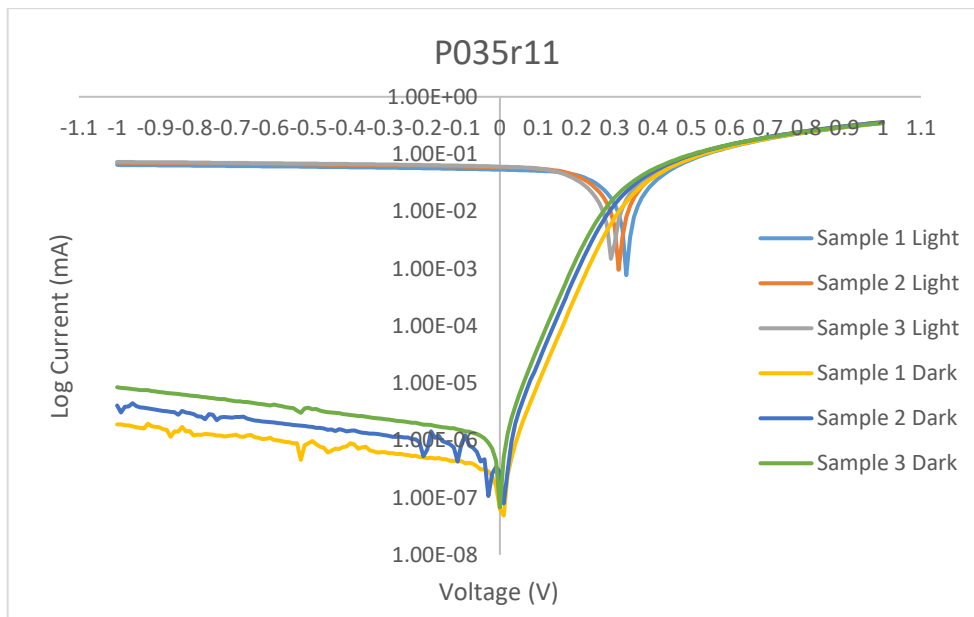


Figure B.4 Logarithmic plot the data in B.3 showing the good asymmetry of the devices in the dark and the change in asymmetry under illumination.

Details of Nanostructured Device Diode Testing

Each nanostructured device was patterned with dZnO top contacts by sputtering through a nickel shadow mask as described in Section 2.1.3. Figure B.5 depicts a magnified image of sample U01-100. The contacts are numbered to indicate testing order and position on the sample surface.

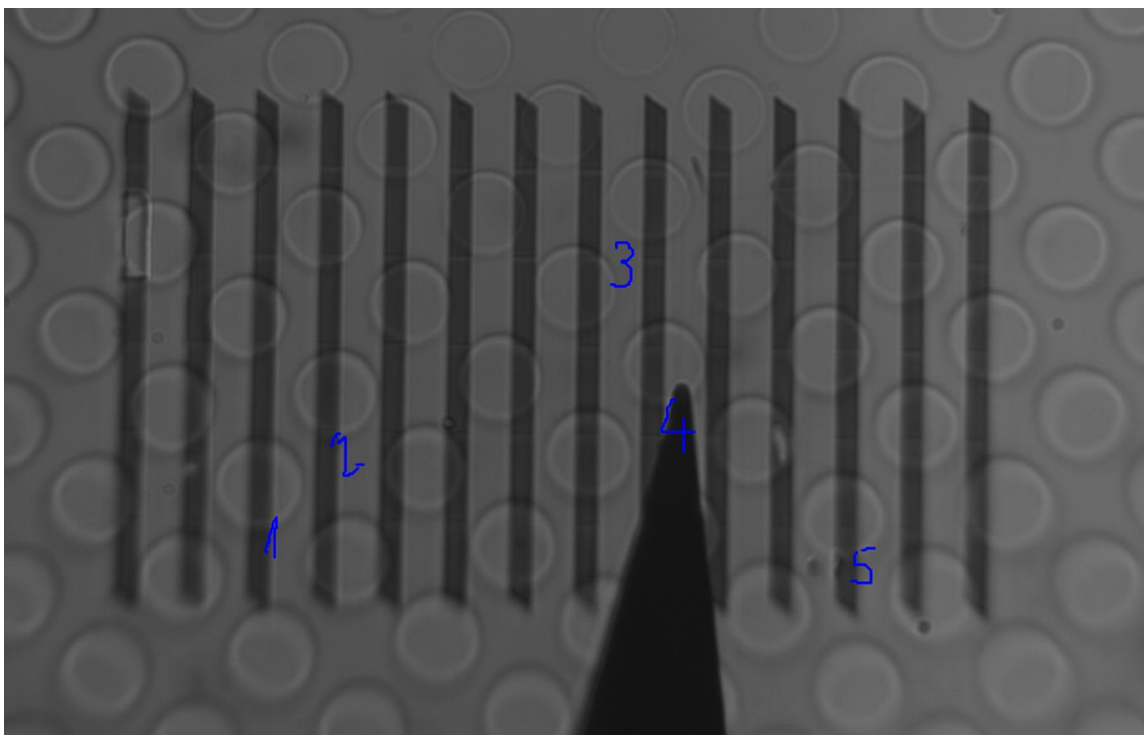


Figure B.5 Magnified image of nanostructured device surface. The transparent conductive dZnO contacts are hexagonally spaced across the nanostenciled stipes. The samples were tested according to the description in Section 2.5.2.

Current-Voltage response was measured for each device in the dark and under illumination as described in Section 2.5.2 and in Chapter 5. Figures B.6 and B.7 depict IV plots of the first 3 tested top contacts from the sample. U01-100 was characterized at 633 nm. The reported value used for further analysis was always based on a single measurement that was representative of the surveyed contacts.

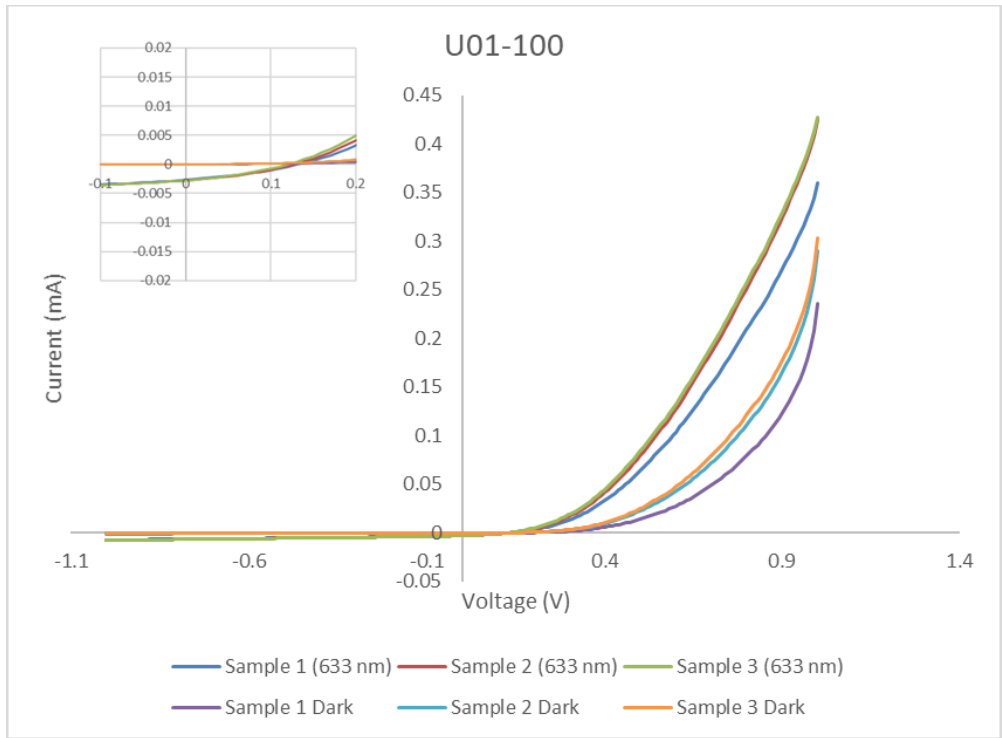


Figure B.6 Examples of light and dark curves for sample U01-100. Samples were illuminated as described in Section 2.5.1 at 633nm. (Inset) The curves in the low voltage region of the plot showing the PV response.

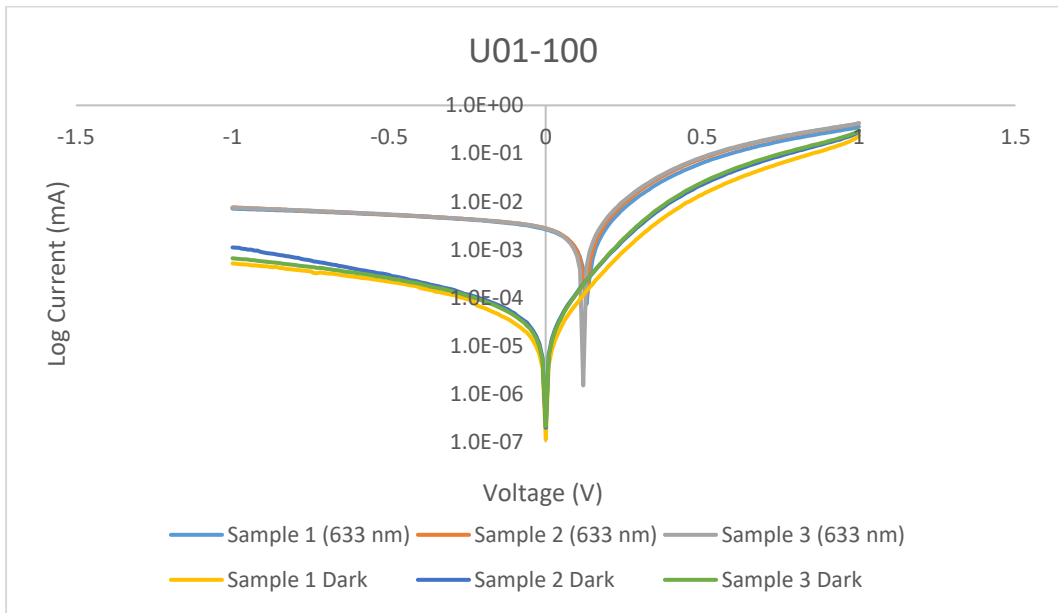


Figure B.7 Logarithmic plot of the data in Fig. B.6 showing the asymmetry of the devices in the dark and the change in asymmetry under illumination.

FDTD Simulation Details

The simulated FDTD spectrum in Figure 5.6 was constructed using Lumerical software (ANSYS Inc.). The Structures were defined using computer aided design (CAD) models of the device layers imported into the Lumerical GUI. The nanostructures were modeled as cylindrical pillars 450nm in diameter, overcoated with 250nm of ZnO. The conformal coating in ZnO above the Ag, was modeled by expanding the diameter of the pillar in the layer to 600nm as observed in the fabricated samples (Figure 2.8a). The modeled source was a Bloch/periodic plane wave with a frequency range of 400-1100 nm and 1000 frequency points. The source was configured at normal incidence polarized along the x direction. The boundary conditions were symmetric in the y direction, anti-symmetric along the x-axis and used a perfectly matched layer (PML) in the z direction. An absorbance monitor was selected to obtain the wavelength-dependent absorbance cross-section. The electric field intensity at the nanostructures was also measured using frequency domain field profile monitors positioned at the silver substrate surface, 50 nm above the surface at the midpoint of the nanostructures, and 100 nm above the surface at the top of the silver nanostructures. Simulations were observed to converge on the result depicted in Figure 5.6 using adaptive grid scaling level 3 or above in the FDTD parameter menu.

The FDTD spectrum displayed Figure 5.6 shows intense absorption resonances at 998 nm and 908nm that we have attributed to surface lattice resonance response of the periodic nanopillared arrays. These excitations generally have mixed photonic and plasmonic character, with the longest wavelength SLR mode being primarily diffractive (i.e. photonic) in nature, with a corresponding high Q and narrow linewidth. The degree of photonic character of the intense absorption peaks at 998 nm and 908nm were confirmed by examining the field magnitudes at these wavelengths using the field profile monitors described above. Figure B.8 depicts the field magnitudes measured at these two wavelengths by the field monitor placed 50nm above the silver substrate. The field distribution shows significant magnitude in the inter-pillar region within the ZnO which would not contribute to IPE and supports the discussion in Chapter 5 of the lower than expected QE measurements (based on absorption intensity) at the line tuned frequencies around 930 nm in Figure 5.11.

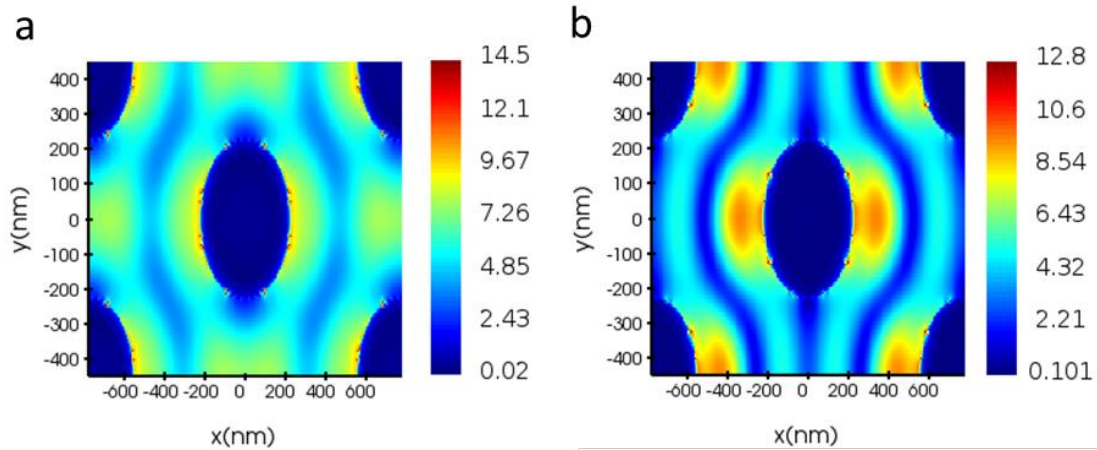


Figure B.8 Electric field magnitudes in the x-y plane half way up the silver nanostructured pillars. The fields confined between the silver pillars (which appear oval due to the simulation unit cell dimensions), and above the metal substrate, demonstrate the photonic character of the a) 998 nm resonance and b) 908 nm resonance shown in Figure 5.6.